Russian Original Vol. 34, No. 6, June, 1973

December, 1973

SATEAZ 34(6) 531-612 (1973)

SOVIET ATOMIC ENERGY

АТОМНАЯ ЭНЕРГИЯ
(ATOMNAYA ÉNERGIYA)

TRANSLATED FROM RUSSIAN

CONSULTANTS BUREAU, NEW YORK

SOVIET ATOMIC ENERGY

Soviet Atomic Energy is a cover-to-cover translation of *Atomnaya Énergiya*, a publication of the Academy of Sciences of the USSR.

An arrangement with Mezhdunarodnaya Kniga, the Soviet book export agency, makes available both advance copies of the Russian journal and original glossy photographs and artwork. This serves to decrease the necessary time lag between publication of the original and publication of the translation and helps to improve the quality of the latter. The translation began with the first issue of the Russian journal.

Consultants Bureau journals appear about six months after the publication of the original Russian issue. For bibliographic accuracy, the English issue published by Consultants Bureau carries the same number and date as the original Russian from which it was translated. For example, a Russian issue published in December will appear in a Consultants Bureau English translation about the following June, but the translation issue will carry the December date. When ordering any volume or particular issue of a Consultants Bureau journal, please specify the date and, where applicable, the volume and issue numbers of the original Russian. The material you will receive will be a translation of that Russian volume or issue.

Subscription
$80 per volume (6 Issues)
2 volumes per year
(Add $5 for orders outside the United States and Canada.)

Single Issue: $30
Single Article: $15.

CONSULTANTS BUREAU, NEW YORK AND LONDON

c/b
227 West 17th Street
New York, New York 10011

Davis House
8 Scrubs Lane
Harlesden, NW10 6SE
England

Published monthly. Second-class postage paid at Jamaica, New York 11431.

SOVIET ATOMIC ENERGY

A translation of *Atomnaya Énergiya*
December, 1973

Volume 34, Number 6 June, 1973

CONTENTS

CONTENTS

(continued)

The Russian press date (podpisano k pechati) of this issue was 5/28/1973. Publication therefore did not occur prior to this date, but must be assumed to have taken place reasonably soon thereafter.

ACADEMICIAN MIKHAIL DMITRIEVICH MILLIONSCHIKOV

The editorial board and staff of "Atomnaya Énergiya" express our deep sorrow on the occasion of the death of this journal's Editor-in-Chief, Academician Mikhail Dmitrievich Millionschikov, an outstanding Soviet scientist, the Chairman of the Supreme Soviet of the Russian Soviet Federated Socialist Republic, the Vice-President of the Academy of Sciences of the USSR, Deputy Director of the I. V. Kurchatov Institute of Atomic Energy, Hero of Socialist Labor, and laureate of the Lenin and State prizes of the USSR, who died on the 27th of May, 1973, at the age of 61. We share the bitter loss of the relatives, friends, and colleagues of the deceased.

Translated from Atomnaya Energiya, Vol. 34, No. 6, p. 426, June, 1973.

ARTICLES

ON CHOOSING METHODS OF CUTTING METALS IN THE REPAIR OF REACTORS

Yu. F. Yurchenko, V. F. Murav'ev, B. A. Pyatunin, and B. G. Malyavin

UDC 621.039.5/68:004.6

All conceivable reactor repair situations have not as yet been studied in sufficient detail; however, it is reasonable to assume that the experience which has been gained all over the world in the use of nuclear power stations will shortly enable mechanisms for the execution of preventive maintenance and emergency repairs to be incorporated in standard reactor repair equipment. Problems of this kind are even now facing the designer.

The majority of repair works involve cutting operations and the removal of the reactor construction elements which are to be replaced. This requires special mechanisms developed for particular repair conditions. The levels of radiation in the repair zones are usually so high that no repair crews can work there. Sometimes special measures may be taken to reduce the level of radiation in the repair zones. For example, filling the vessel of a discharged water-cooled, water-moderated reactor with water after several years use enables repair work to be carried our fairly safely using special remote-control mechanisms inside the vessel. It is therefore of particular interest to discover and develop such effective methods of cutting metals as will enable reliable remote-control mechanisms to be created, capable of working both in air and under a layer of water.

For separative cutting in the dismantling of reactor construction elements requiring replacement, mechanical and gas–electric (plasma) methods of cutting are usually employed. The mechanical cutting of construction materials is executed with special remote-controlled machinery. The machines are most frequently designed for one particular operation and are very complicated in design and manufacture. Mechanical cutting involves a great deal of mechanical pressure between the tool and the part being cut. This means that the framework of the mechanism has to be rigid, and the whole thus becomes much heavier. The tool in such mechanisms also has to have at least two motions (to and fro), complicating the kinematics of the machine.

The use of gas–electric cutting is limited by the thickness of the metal being cut, the dimensional circumstances in the repair zone, and also the complexity of the technology of repair work under water. Existing equipment allows steel up to 60 mm thick to be cut under water. Thicker metal can only be cut if there is space for the plasma jet to pass right through.

As the result of a continuing search for other methods of cutting metals, free from the disadvantages associated with those just indicated, it was found that the electrical-contact method of cutting was the one most suitable under the specific conditions of reactor repair. This method involves very little pressure between the tool and the part being cut, it enables various cutting operations to be carried out with the tool simply moving forward in the feed direction, the cutting process is stable in both air and water, simple and inexpensive equipment may be used, and there is a low specific consumption of electrical power (1-4 kW · h/kg).

In order to compare mechanical drilling with the plasma and electrical-contact cutting of metals, Table 1 presents some characteristics of the corresponding equipment for driving holes 120 mm in diameter in stainless steel plates 130 mm thick under a layer of water. The thickness of the plate was chosen from a consideration of the maximum resistance of a circular drill under optimum boring conditions.

Translated from Atomnaya Énergiya, Vol. 34, No. 6, pp. 427-434, June, 1973. Original article submitted February 1, 1972.

TABLE 1. Some Characteristics of Equipment for Driving Holes in a Steel Plate by Various Methods

Form of cutting	Thickness of plate, mm	Form of tool	Cost of tool, roubles	Cutting time, min	Cutting force, kg	Weight of equipment (without supply source), kg	Cost of equipment, roubles
Drilling	130	Circular drill (ϕ130 mm, length of working part 200 mm)	416	55	Axial 1500, circumferential 350	3100	3800
Plasma cutting	55	Plasma burner	50	2,5	–	45	6800
Electrical-contact cutting	130	Circular electrode	2,5	16	Up to 5	20	1200

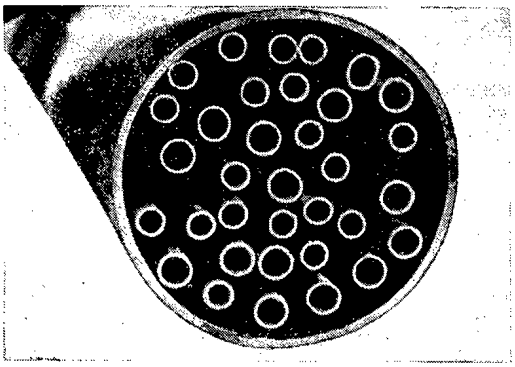

Fig. 1. Section of an object with a complex cross section after cutting with a disc electrode, the cutting zone being intensively water-cooled.

Arrangements for the Electrical-Contact Cutting of Metals

This method involves the removal of metal from the part being cut by virtue of the thermal action of powerful transient arc discharges on its constituent material, these discharges being excited between electrodes (usually in mutual contact) attached to ac or dc sources.

Electrical-contact cutting may be executed with either rotating or nonrotating electrodes. In the first case cutting may be effected over wide ranges of the electrode voltages and the specific powers evolved at the electrodes. When these parameters vary, so do the cutting efficiency and the quality of the surface cut. For example, cutting by electrical fusion at a voltage of 36 V or over is characterized by a high value of the specific power evolved at the electrodes and a high cutting efficiency, but a low quality of the cut surface and a fairly deep zone of thermal influence. This somewhat restricts the use of electrical-contact cutting in the electrical-fusion mode.

Figure 1 shows a cut through a part of complicated cross section obtained in water by means of a rotating tool electrode (disc) with 24 V on the electrodes. The quality of the surface of the cut is $\nabla 3$.

By using special discs with abrasive electrical-insulating coatings of their lateral surfaces (for example, a coating made from aluminum oxide powder) we may improve the quality of the cut surface to $\nabla 6$-$\nabla 7$. On using such electrode tools for the electrical-contact cutting of hollow parts and tubes under a layer of water or with intensive water cooling of the cutting zone, we may obtain a high-quality cut surface over the whole cross section of the part. The cutting efficiency increases by about a factor of ten over that of conventional mechanical methods.

The foregoing advantages of electrical-contact cutting with a rotating electrode offer excellent prospects for its use in industry [1-3]. However, the use of this type of cutting for the repair of nuclear reactors involves serious difficulties. This is due to the following circumstances. The weight of the machines used for electrical-contact cutting with a rotating electrode is as great as that of those used for mechanical cutting [3]. In the first case the machines have comparatively complex kinematics, which makes remote control more difficult. Furthermore, the presence of water (as a coolant) greatly increases the power of the drive motors required for electrode discs rotating at more than 20 m/sec, and requires the installation of complicated sealing systems to prevent water from passing into the current-taking devices and thus to ensure their efficient operation.

Hence under the specific conditions of nuclear reactor repair special interest is evoked in electrical-contact cutting with nonrotating electrodes, which, depending on the shape of the working part of the electrodes, facilitates separative cutting, the cutting of apertures in metal plates and the sides of the vessels, the removal of broken pins from these, and other operations. The simplicity with which such operations may be executed enables us to create light, reliable, and inexpensive equipment.

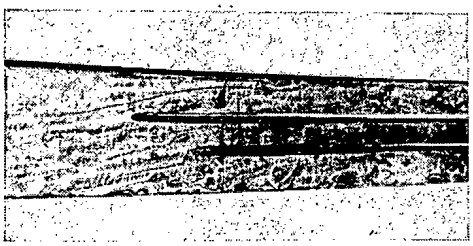

Fig. 2. Cut through a stainless steel plate made with a laminar graphite electrode under a layer of water.

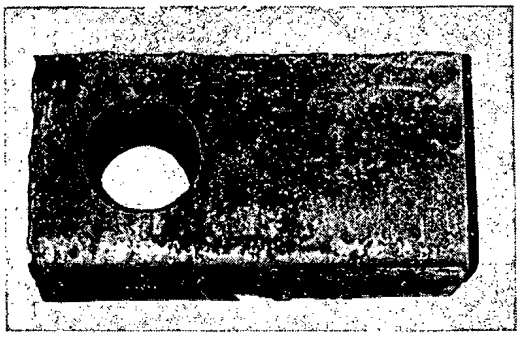

Fig. 3. St. 3 sample with a hole 80 mm in diameter drilled through it.

Cutting with a nonrotating electrode may only be effected in the mode of electrical fusion.

Figure 2 shows a cut through a stainless steel plate 30 mm thick made with a nonrotating electrode under a layer of water. The cutting speed was 150-200 mm/min.

Figure 3 shows a St. 3 plate 180 mm thick with a hole bored through it, 80 mm in diameter. The operation was effected with a tubular graphite electrode under a layer of water.

Materials for Tool Electrodes and Their Wear in Electrical-Contact Cutting

The intensive action of the powerful arc discharges causes wear of the tool electrode materials, appearing in the form of electrical erosion. Furthermore, tool electrodes working without intensive cooling by an external medium experience severe thermal loading. This influences the mechanical strength of nonrotating electrodes, and reduces the dynamic stability during the operation of rotating electrodes, owing to thermoplastic deformations. The use of liquid media possessing a fairly high specific heat and thermal conductivity (for example, water and aqueous solutions of chemical compounds) greatly reduces the thermal stress on the tool electrodes and improves their working conditions.

Apart from electrical erosion, wear on certain electrode materials may also arise from the formation of volatile oxides and other chemical compounds in gas media. Such materials include molybdenum and tungsten, which, despite their high thermophysical properties, undergo serious wear when used as electrode material for electrical-contact cutting in air. The oxides of these metals, formed at 750-800°C, sublime very considerably at the same temperatures. The wear on graphite electrodes increases with increasing rate of pumping air through the cutting zone because of the oxidation of the carbon.

The external medium has hardly any effect on the amount of electrical erosion of the electrode materials at those currents characterizing electrical-contact cutting with a nonrotating electrode. Tests showed that the degree of electrical erosion of nonrotating graphite electrodes during electrical-contact cutting in water, electrolyte solutions, oils, and air (without pumping the latter through the cutting zone) remained constant. The same effect was noted in [4], in which it was indicated that for high currents in arc discharges the external medium was displaced from the electrodes by the vapor of the electrode materials.

The wear of the rotating electrodes also includes a component due to processes taking place as a result of friction between the tool electrodes and the part being machined in those cases in which cutting is effected with a low voltage on the electrodes, i.e., in which the contact mechanism of arc-discharge excitation predominates.

Water-cooled rotating electrodes are usually made from low-carbon steels, brass, copper, or special cast iron. The use of refractory metals or metalloceramic composites is economically undesirable owing to the complexity involved in the manufacture of such tools and their high net cost.

Investigations showed that, under optimum cutting conditions, the wear resistance of tools using metalloceramic of the VM-70 type (tungsten–copper–nickel) was only 1.3-1.6 times higher than that of cast iron tools.

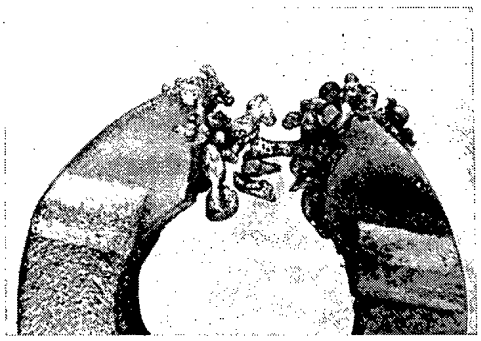

Fig. 4

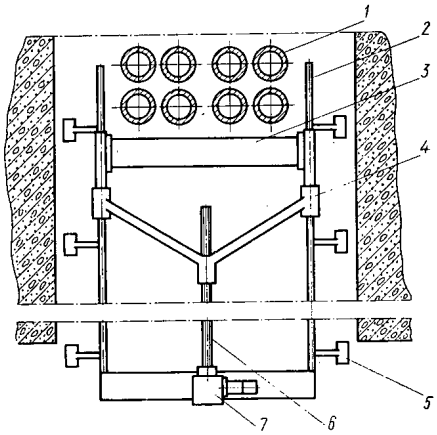

Fig. 5

Fig. 4. Granules formed after the electrical-contact cutting of 18-8 steel under a layer of water; the granules are collected with a magnet.

Fig. 5. Arrangement of the apparatus for remote-control electrical-contact cutting of an array of tubes: 1) tube being cut; 2) guides; 3) electrode plate; 4) master nut; 5) carriage; 6) lead screw; 7) electromechanical drive.

For the reasons just outlined, chief interest lies in nonrotating tool electrodes. These are made of graphites, which have the great advantage that under the thermal action of arc discharges they suffer no fusion but rather sublime, dissipating far more thermal energy than would occur on melting, and a higher wear resistance is thus achieved in electrical-contact cutting.

As regards erosion resistance and mechanical strength, pyrolytic graphites are the best; these have a highly oriented structure and high specific gravity [5]. Pyrolytic graphites may also be used as coatings for ordinary graphites, increasing the strength of tool electrodes made from such materials and increasing their cutting efficiency.

Of all the pyrolytical graphites, we may specially mention that of the PGV type, which has advanced thermophysical and mechanical properties: 1) thermal conductivity – along the *a* axis 150-300, along the c axis 2.5-4.0 m·W/deg; 2) compressive strength – along the *a* axis 5-7, along the c axis 25-30 kg/mm^2; 3) bending strength – along the *a* axis 1-2, along the c axis 25-30 kg/mm^2; 4) resistivity – along the *a* axis $(1.63\text{-}2.0)\cdot 10^{-4}$, along the c axis 0.2-0.3 Ω·cm.

Phenomena Accompanying Electrical-Contact Cutting

In developing a technology for repair which involves electrical-contact cutting, allowance should always be made for phenomena accompanying the cutting process.

As a result of the thermal action of the arc discharges on the electrode material the latter evolve their own vapors, which emerge from the cutting zone at a high velocity. The intensity of vaporization depends on the power of the arc discharges, their repetition frequency, and the thermophysical properties of the electrode materials and the medium.

When the vapors of the electrode materials condense in the gas medium, highly dispersed solid particles 0.1-20 μ in size are created. The particles formed as a result of the cutting of construction materials having induced radioactivity are propagated into the free gas space in the form of an aerosol cloud. The particles settling on the wall surfaces of the room and on the equipment constitute radioactive contamination. These particles adhere firmly to metal, particularly to polished stainless steel, and remain attached to them [6]. Hence when conducting electrical-contact cutting in air it is essential to provide special suction systems and corresponding systems of gas purification. Methods of deactivating the equipment must also be selected.

In order to remove the contaminants formed during electrical-contact cutting, ordinary redox deactivation methods may be used. The volumes of the desorption solutions and the number of deactivation cycles may be reduced if easily-removable coatings are first applied to the surface of the equipment.

TABLE 2. Examples of Metal-Cutting Operations in Reactor Repair

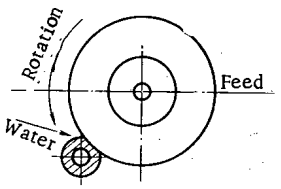	Disc cutting of construction units. Executed with a rotating electrode and water cooling in the cutting zone. Surface quality ∇_3. Electrode voltage 18-32 V.
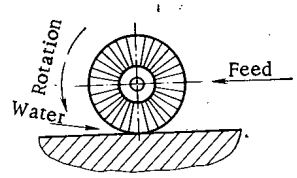	Finishing of metal surfaces. Executed with a rotating brush electrode and water cooling in the cutting zone. Surface quality $\nabla 3$-$\nabla 5$. Electrode voltage 10-18 V.
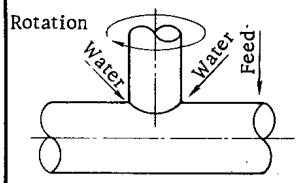	Cutting into tubes, cutting apertures in tubes and sheets. Executed with a rotating tube electrode and water cooling in the cutting zone. Electrode voltage 18-32 V.
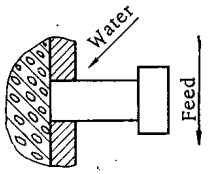	Cutting of construction units, face plates, etc. Executed with a graphite electrode (no rotation) and water cooling of the cutting zone, or under a layer of water. Surface quality – unclassified. Electrode voltage 36-50 V.
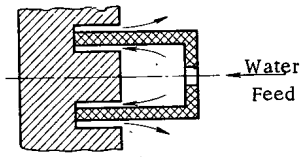	Broaching of apertures, removal of broken pins. Executed with a circular graphite electrode (no rotation), water being fed into the inside of the electrode. Quality of machined surface – unclassified. Electrode voltage 36-50 V.
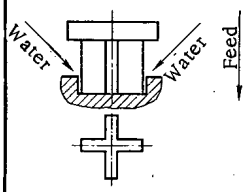	Hollowing of grooves in parts Executed with a graphite electrode having a profiled working part, the working zone being water cooled, or executed under a layer of water. Surface quality after machining – unclassified. Voltage 36-50 V.

In under-water cutting, the electrode vapors condense in the water. In this case colloidal solutions are formed. Coarse colloidal solutions rapidly coagulate (in 25-30 min). Fine solutions break up more slowly. Thus, for example, after leaving the water used for cutting stainless steel to settle for two days it still contains up to 4 mg/liter of iron oxides and 0.5-0.7 mg/liter of chromium and titanium oxides. The formation of colloidal solutions turbidizes the water, and this impedes the use of optical observation systems.

Under-water electrical-contact cutting is accompanied by the evolution of oxygen and hydrogen, formed by the decomposition of the water. For a thin layer of water above the cutting zone, these gases are intensively evolved and suffer combustion. The possibility of hydrogen accumulating in a certain closed volume cannot however be ruled out. On immersing the cutting equipment to a depth of 5-6 m these gases fail to reach the surface of the water. Evacuation of the cutting products from the repair zones is one of the essential measures required to ensure successful execution of subsequent operations.

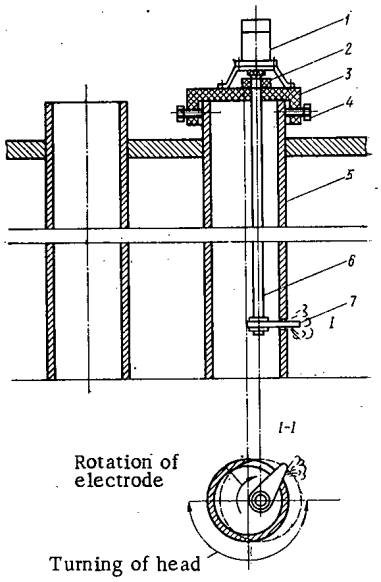

Fig. 6

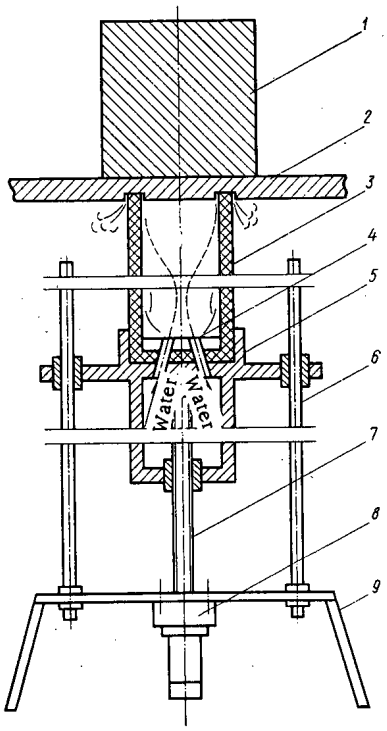

Fig. 7

Fig. 6. Mechanism for the electrical-contact cutting of tubes from within: 1) shaft-rotating motor; 2) current-taking device; 3) housing of cutting head; 4) screw supports; 5) tube being cut; 6) shaft; 7) electrode.

Fig. 7. Arrangement of apparatus for the electrical-contact broaching of holes in freely-mounted parts: 1) cast iron cube (part to be broached); 2) plate on which the part is freely mounted; 3) tool electrode; 4) electrically-insulating plate; 5) carriage; 6) guides; 7) lead screw; 8) electromechanical drive feeding the electrode; 9) stand.

In electrical-contact cutting in air, it is essential to provide surface protection for equipment situated around the current zone so as to prevent the adhesion of molten metal, and also to provide for the subsequent removal of any which does adhere. Demountable screens are used to this end.

The thermophysical properties of the metal being cut and the rate of cooling the molten metal affect the size and shape of the solidified drops. On cutting in air, the drops of melt merge into a shapeless mass. On cutting under water the molten metal becomes granular. During the cutting of stainless steel under water, hollow granules 0.01-12 mm in size are created. Of these 10-12% are spherical and the rest are drawn out and geometrically irregular. Up to 60% of the granules acquire magnetic properties arising as a result of the formation of delta ferrite by the high rate of cooling of the melt in water; magnets may thus be used to remove them (Fig. 4).

The shape and size of the granules formed in the under-water cutting of aluminum and its alloys differ considerably from steel. In this case long, drop-like granules with acicular tips are usually formed. Some granules extend to 15 mm.

Supply Sources

In electrical-contact cutting, supply sources with strict volt–ampere characteristics and fairly high powers (100 kVA and over) are used; their voltage is regulated within the range 18-50 V.

No special dc or ac sources are produced by industry for electrical-contact machining. Standard-production armored transformers are therefore employed. These include, for example, dry transformers

of the OSU-100 type, which may be used in twos or more by parallel connection in the supply source. The same transformers, furnished with rectifier systems, may be used as dc supply sources; these have some advantages over ac sources in respect of a reduction of the reactive components of the circuit impedance and the wear on the tool.

The choice of supply sources with due allowance for the required cutting efficiency is considered in [7]. The same paper indicates a method of calculating the circuit elements of the supply source for the electrical-contact cutter.

Use of Electrical-Contact Cutting in the Repair of Reactors

Examples of some technological operations encountered in reactor repairs for which electrical-contact cutting is suitable are presented in Table 2.

In the repair of reactors, cutting operations often have to be executed under cramped conditions so that traditional cutting methods are difficult or impossible. In such cases electrical-contact cutting with nonrotating electrodes is particularly effective.

We shall now give a brief description of some mechanisms for electrical-contact cutting in similar operations.

Cutting of an Array of Tubes. The most typical repair operation is the cutting of an array of tubes. If the array of tubes is situated in the housing in such a way that the distance between individual tubes and the walls is insufficient for the operation of ordinary cutting tools, the device illustrated in Fig. 5 is employed.

A laminar graphite electrode with a length greater than the width of the array of tubes is moved along guides on a carriage by means of a lead screw, driven by an electromechanical system. The cutting process is stabilized and the normal thermal conditions of the cutting electrode kept constant by virtue of feedback (introduced into the electrical drive circuit) between the rate of rotation of the dc electric drive motor and the cutting current. In order to avoid rupture of the electrode, a current-limiting relay is also provided for the current in the core winding of the electric motor driving the electrode; this disconnects the motor if the current rises too high.

The supply source includes two parallel transformers of the OSU-100/0.5 type each with a power of 100 kVA. The power of the supply source is sufficient for the series or parallel cutting of any tubes made from the construction materials generally employed in reactor building.

Cutting of Tubes from Inside. In repair work it is often required to cut tubes from inside with the cutting instrument situated at a considerable distance from its drive point. For cutting tubes with an internal diameter of 30 mm or over in this way in straight vertical sections an electrical-constant cutting head may be used (Fig. 6).

The cutting head is furnished with a lamellar electrode made of pyrolytic graphite fixed to a shaft with a current-collecting device. To the framework of the mechanism an electrical motor for driving the rotating shaft is attached. The mechanism is placed at the top of the tube and fixed with a screw support. The shaft carrying the tool electrode is placed eccentrically with respect to the axis of the tube being cut. When the supply source and the shaft-rotating motor are connected, the working edge of the electrode touches the wall of the tube, as a result of which electrical fusion occurs.

After the graphite electrode has rotated through 360° the tube is not completely severed. This is achieved after rotating the framework of the cutting head through 180°. The cutting may be effected in either air or water. The fact that there is no pressure between the tool electrode and the part, together with the fact that the electrode is very light, enables tubes to be cut at a depth of 10-15 m from the site of the mechanism.

Broaching Holes in Freely-Mounted Parts

Using the mechanism illustrated schematically in Fig. 7, open apertures may be broached in freely-mounted parts. The mechanism has been used to broach holes 130 mm in diameter in cast iron cubes freely installed on a steel floor. The depth of the apertures is 280 mm.

Broaching is effected with a tubular electrode having a diameter 4-5 mm smaller than the diameter of the opening to be broached, while the length exceeds the thickness of the broached metal by 60 mm. The electrode is fixed in a movable carriage set in motion by a lead screw. The screw is rotated by an electromechanical drive, the electrical circuit of which incorporates feedback between the current in the core winding of the dc drive motor feeding the electrode and the current effecting the broaching. All the mechanisms are placed on a firm base. Inside the electrode is a plate of electrically-insulating material preventing it from coming into contact with the core being cut out.

The tool is made of GMZ graphite, the surface of the electrode being coated with pyrographite. As supply source there is a pair of parallel-connected transformers of the OSU-100/0.5 type with an electrode voltage of 40-50 V. As the broaching depth increases, the rate of feed of the tool falls from 40 to 5 mm /min. This is because the conditions for removing the erosion products worsen as the depth of incision increases, despite the fact that water is forced through the inside of the electrode. Using an analogous device, apertures may be made in the walls of reactor vessels.

CONCLUSIONS

Practice has shown the efficiency and economic viability of the electrical-contact cutting of metals in the repair of nuclear reactors, particularly cutting with nonrotating electrodes.

The advantages of the electrical-contact method of cutting metals are as follows: simplicity of execution, low cost of the equipment, and possible application to all metals used in reactor building, whether the cutting is effected in air or in water.

LITERATURE CITED

1. In Nonstandardized Technological Equipment and Fittings, Catalog No. 2 [in Russian], TsINTINeftekhimash, Moscow (1971), p. 36.
2. N. S. Kabanov and A. V. Piskunov, Avtomaticheskaya Svarka, No. 4, 11 (1967).
3. D. M. Zmiev and B. V. Kuznetsov, Anodic Mechanical Cutting of Metals in Disc Machines [in Russian], ENIMS, Moscow (1970).
4. V. I. Rakhovskii, G. V. Levchenko, and O. K. Teodorovich, Break Contacts of Electrical Apparatus [in Russian], Energiya, Moscow (1966).
5. A. S. Fialkov et al., Uspekhi Khimii, 34, No. 1 (1965).
6. A. D. Zimon, Adhesion of Dust and Powders [in Russian], Khimiya, Moscow (1967).
7. A. S. Davydov, in: New Methods of Machining Metals [in Russian], GOSINTI, Moscow (1964).

SOME PROBLEMS IN THE OPERATIONAL SAFETY OF ATOMIC POWER STATIONS USING GAS-COOLED FAST REACTORS WITH A DISSOCIATING COOLANT

G. A. Sharovarov

UDC 621.039.58

One of the most important problems in nuclear power generation is the operational safety of atomic power stations using gas-cooled fast reactors, which are characterized by high thermal stress, low accumulating capacity in the coolant, and correspondingly short periods of operation before breakdown processes develop. Breakdown processes may be divided into two main stages: first, a rise in the temperature of the fuel and the jacket of the fuel element until the melting point is reached and, second, melting of the active zone, with displacement of the fuel and the possible formation of a secondary critical mass, leading to an explosion.

The requirements for absolute safety have been discussed in many recent works on breakdown processes in various types of fast-reactor power stations [1-5]. Unfortunately, the general requirements and the corresponding standards for the investigation of nonstationary breakdown processes in the design of atomic power stations have not yet been clearly formulated. This is attributable to the fact that the various atomic power stations investigated differ considerably in their thermodynamic cycles, their flow circuits, the coolants they use, and other features.

The most important problem in operational safety is to prevent the melting of the active zone, with possible displacement of the fuel, formation of secondary critical mass, and explosion. As is generally known, this is defined as ultimate failure.

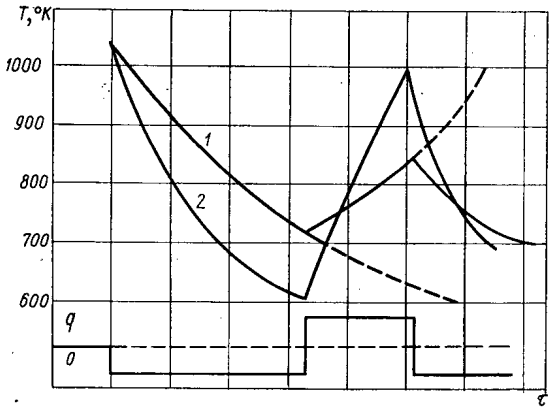

Fig. 1

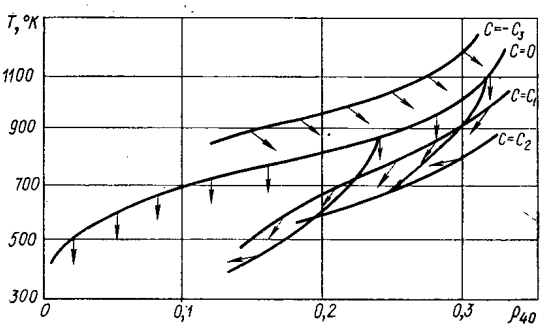

Fig. 2

Fig. 1. Coolant temperature as a function of time when the heat flow q varies as a step function: 1) process for equilibrium properties; 2) process for nonequilibrium properties.

Fig. 2. Coolant phase diagram for oxygen (P = const, $q_V = -23{,}000$ kcal/m$^3 \cdot$ sec). The curves are drawn for a constant value of $C = d\rho_{40}/dT$, with $C_2 > C_1 > 0 > -C_3$.

Translated from Atomnaya Énergiya, Vol. 34, No. 6, pp. 435-439, June, 1973. Original article submitted November 9, 1972.

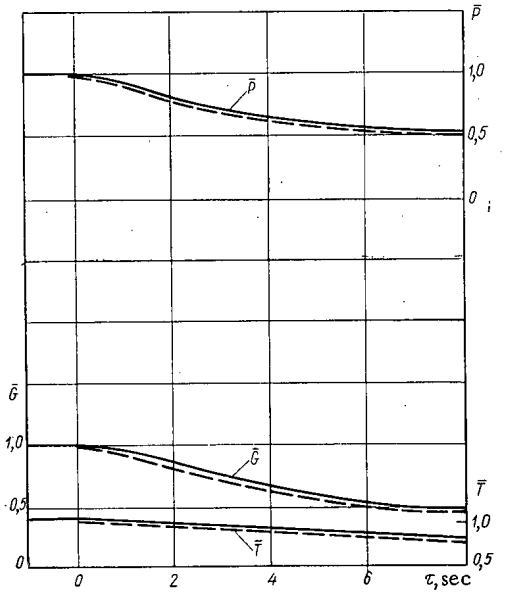

Fig. 3. Curves showing flow rate, pressure, and temperature of the coolant at the reactor inlet when the pumps fail: ——) main circulating pumps; ---) power station.

In order to solve the problem it is essential, above all, to ensure reliable coolant circulation during a power-station breakdown and shutdown cooling of the reactor. In addition, the reactor design must ensure the necessary temperature effects and include a highly reliable breakdown-protection system.

The most dangerous breakdown situations are those involving a failure of the seal in the primary loop at various points of the flow circuit, cutting off the flow of the main circulating pumps, the compressors, or the entire power station, and also those involving an accidental change in reactivity. In all breakdown situations, it is essential to maintain continuous circulation of the coolant through the reactor. The length of time that continuous circulation is maintained and the nature of the change in coolant flow for different types of breakdown are determined primarily by the flow circuits, the thermodynamic cycle, the design of the reactor, and the properties of the coolant.

In the present study we shall discuss possible solutions of these problems for atomic power stations using the dissociating coolant N_2O_4. We shall investigate the characteristic factors which are specific to dissociating coolants alone, since the other difficulties involved in maintaining safe operation remain the same for all gas-coolant reactors. The most important feature of atomic power stations using a dissociating coolant is that they use a single-loop conversion system and use a gas–liquid thermodynamic cycle in a gas-cooled reactor [5-10].

The main characteristics of nonstationary processes in nuclear power installations using a dissociating coolant are determined by nonstationary processes in the coolant, which differs in principle from ordinary gaseous coolants. Because the thermophysical properties of a dissociating coolant are variable, the processes in it cannot be regarded as inertialess. For a given pressure and temperature and comparable periods of time for the chemical reactions and technological processes, the properties will also depend on the characteristics of the nonstationary process taking place in the coolant.

For example, Fig. 1 shows that the temperature of a gas in a real nonstationary process varies more sharply for a change in heat flow than for inertialess chemical reactions.

In Fig. 2 we show the phase diagram for the relative density of oxygen in the dissociating mixture. The curve C = 0 corresponds to the process with inertialess chemical reactions. The arrows indicate the direction of the possible process when cooling takes place as a function of the initial state. The amount of oxygen depends not only on the temperature and pressure but also on the initial conditions and the nature of the nonstationary process. Thus, the dissociating coolant is a dynamic system characterized by the kinetics of the chemical reactions.

One of the most dangerous breakdowns in multi-loop atomic power stations using a gaseous or liquid–metal coolant is loss of power in the main circulating pumps or compressors, since in this case it is extremely difficult to maintain continuous circulation. Continuity of circulation can be maintained for some time, at diminishing pressure difference, for a specific quantity of coolant on the high-pressure side. The use of a gas–liquid thermodynamic cycle with a dissociating coolant is characterized by the large amount of coolant in the loop in comparison with the flow rate and the considerable drop from maximum to minimum pressure in the loop [10].

The ratio of the amount of coolant to the flow rate in the corresponding segment of the loop is determined by the coefficient

$$\frac{\text{amount of coolant}}{\text{flow rate}} = K_m = \frac{M}{G}\int_0^l \frac{dl}{w},$$

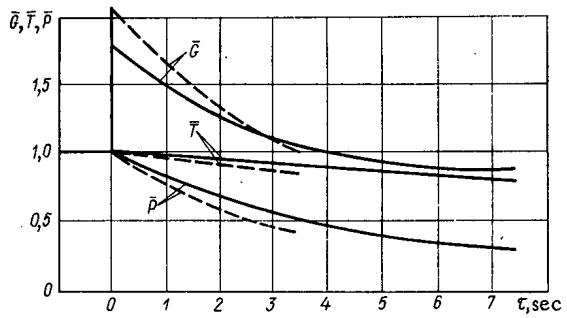

Fig. 4. Curves showing the flow rate, pressure, and temperature of the coolant at the reactor inlet for a burst duct at the reactor outlet; ——) break in main vapor duct, with $F_{eff} = (1/6)F_0$; ---) break in one branch of a six-branch vapor duct.

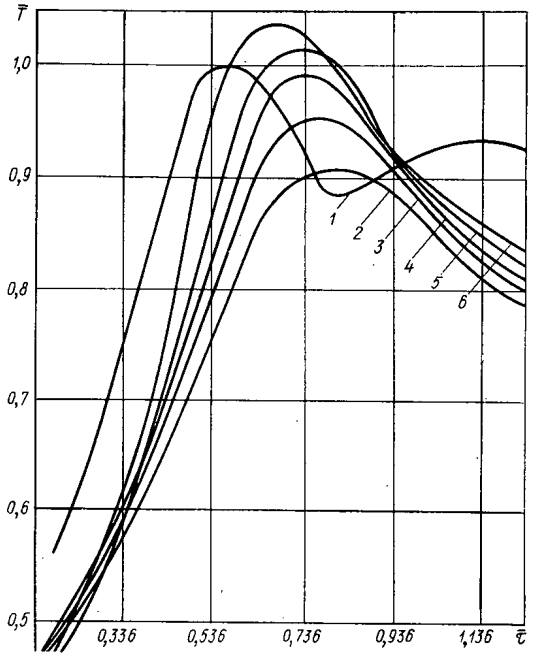

Fig. 5. Variation in fuel-element jacket temperature when there is a break in a duct at the reactor outlet: 1) τ = 0 sec; 2) 0.5 sec; 3) 1.5 sec; 4) 2 sec; 5) 2.5 sec; 6) 3 sec.

which indicates the length of time the segment could maintain a nominal coolant flow rate. The difference between the maximum and minimum pressure values results in natural flow of the coolant between the high-pressure and low-pressure sides. Relatively low flow velocities in the dissociating coolant in the liquid phase will result in large values of the coefficient K_m. In individual segments, according to the data of the Nuclear Energy Institute of the Academy of Sciences of the Byelorussian SSR, this length of time that the coolant continues to flow after the pump stops may vary from 20 to 60 sec, depending on the design and the parameters of the cycle.

For gas-cooled loops with other coolants, this coefficient is much lower. In a two-loop conversion system the difference between the maximum and minimum pressure values in the first loop depends only on the hydraulic resistances and has a low value, which cannot maintain the necessary coolant circulation. In a single-loop conversion system this difference depends on the pressure ratio in the thermodynamic cycle. When the coolant used is helium, this values varies from 2 to 7 [6]. In a gas–liquid cycle with a dissociating coolant the pressure ratio is about 70 when the difference between the pressures ranges up to 160 atm.

The following basic assumptions were made in the investigation of breakdown situations: the gas in the loop expands polytropically; the fuel and the jacket of the fuel element have a temperature equal to the value obtained by averaging over the radius; the processes in each volume correspond to equilibrium properties; the characteristics of the turbines conform to Fluegel's equations; and the reactor kinetics are characterized by a concentrated model with six groups of delayed neutrons.

We can see from Fig. 3 how the flow rate, pressure, and temperature of the dissociating coolant at the reactor inlet vary when the main circulating pumps fail (there is no overshoot of the pumps, and vapor is formed only as a result of the heat contained in the coolant). When the whole station loses power, the vapor goes past the turbines into the condenser.

Owing to the accumulation of gas on the high-pressure side, continuous circulation is maintained for a fairly long time, affording an opportunity for action to restore the power or shut down the reactor and organize the shutdown cooling process.

Let us consider a breakdown in which there is a break in the main vapor duct with an effective cross section equal to the area of one branch on the segment between the reactor and the high-pressure turbine. The variation of the coolant flow rate, temperature, and pressure at the reactor inlet is shown for two cases of this kind of breakdown in Fig. 4. The coolant flow rate sharply increases at first, after which it diminishes as time increases. The reactor control systems maintain constant power, and the breakdown protection system is not yet activated. In Fig. 5 we show how the fuel-element jacket temperature varies along the zone. The maximum temperature drop is about 10%.

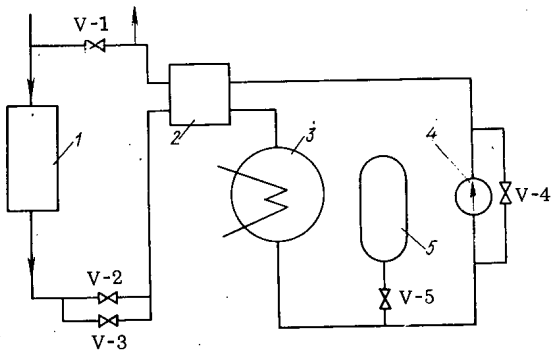

Fig. 6. Diagram of shutdown cooling system: 1) reactor; 2) regenerator; 3) condenser; 4) pump; 5) tank of liquid coolant.

A study of the power variation resulting from the temperature effects following a failure of the automatic power-regulating system showed that when the value $N = 1.15\ N_0$ is reached, the breakdown-protection system will be activated, with a delay of 0.5 sec. The variation in jacket temperature vertically along the zone does not exceed the allowable values.

Thus, when there is a break in the main vapor duct at the reactor outlet, the accumulation of gas on the high-pressure side may maintain continuous circulation, affording an opportunity to take steps to shut down the reactor and initiate the process of shutdown cooling. The greatest danger in such a breakdown may result from the substantially increased pressure drop in the structural elements of the reactor due to the increase in hydraulic resistances when the coolant flow rate is high.

A break in the main vapor duct at the reactor inlet is a very serious kind of breakdown. Depending on the cross-sectional area of the break, the forward circulation may be reduced and reverse circulation may take place. There may be points with zero coolant flow in the gas passages. When there is reverse circulation, the coolant stops at the instant the break takes place, after which it flows in the reverse direction owing to the accumulation of gas in the segment between the reactor and the high-pressure turbine. The gas in the high-pressure cavity flows out in two directions at the same time: through the reactor and through the high-pressure turbine into the regenerator, after which it passes through the low-pressure turbine into the condenser.

In order to estimate the properties of reactor self-regulation when there is a sudden variation in reactivity, we compared it with a sodium-cooled reactor. To obtain an equal power-excursion value, we must introduce twice as much reactivity into the reactor using the dissociating coolant.

The density effect makes very little change in transient regimes. Even when the coolant is completely removed and the regulating system fails, the power excursion does not exceed the allowable values.

The special physicochemical and thermophysical properties of N_2O_4, whose boiling point lies in the operating-temperature range, makes it possible to use the coolant in the liquid phase for shutdown cooling of a gas-cooled reactor [11]. A special system is provided for emergency shutdown cooling. The initial (emergency) cooling of the reactor, as was shown, can be carried out by means of the main loop, after which the shutdown cooling system is connected.

In Fig. 6 we show a diagram of the shutdown cooling system, which is a closed gas–liquid loop connected to the reactor in parallel with the main loop. While the power station is in operation, the coolant passes through the shutdown cooling system by way of the shutoff valve V-3, heating the heat-exchange apparatus and the ducts. The coolant passes from the reactor to the regenerator and is then condensed; it enters the regenerator by way of valve V-4, bypassing the pump and is discharged to the condenser of the main loop.

When there is a breakdown, the heat is initially removed by the main loop owing to the coolant flowing through it. Then, by means of the breakdown-protection system, shutdown cooling takes place; for this purpose valves V-1 and V-2 are opened and the main loop is disconnected. The shutdown cooling system operates on a gas–liquid cycle. After reducing the pressure and temperature of the coolant, there is a change to liquid circulation. For this purpose, valve V-5 is opened and the liquid from the tank enters the loop. The shutdown cooling system is fed by an independent source of electric power.

It should be noted that an emergency shutdown cooling system using a liquid product can be used in ordinary operation.

On the basis of the foregoing, we may state the following conclusions.

1. The special properties of a flow circuit and a thermodynamic cycle using a dissociating coolant make it possible to maintain continuity of circulation and ensure both initial cooling of the reactor and shutdown cooling after the breakdown-protection system has been activated.

2. The special physicochemical properties of dissociating coolants make it possible to use the coolant in the lquid phase for shutdown cooling of a gas-cooled reactor.

3. In order to prevent any deformation and rupture of structural elements of the reactor, means should be provided for limiting the flow rate of the coolant coming out of the maximum-pressure region.

4. For single-loop atomic power stations with a dissociating coolant, it is desirable to use a special emergency shutdown cooling system.

LITERATURE CITED

1. D. Okrent et al. (United States), Third Geneva Conference (1964), Report No. 267.
2. W. J. McCarthy Jr. et al. (United States), Third Geneva Conference (1964), Report No. 284.
3. K. Grattion et al. (Netherlands), Fourth Geneva Conference (1971), Report No. 023.
4. O. M. Kovalevich, in: Status and Prospects of Work Designed to Develop Atomic Power Stations with Fast Reactors, Vol. II [in Russian], SÉV Symposium, Obninsk (1967), p. 344.
5. Yu. E. Bagdasarov et al., Technological Problems of Fast Reactors [in Russian], Atomizdat, Moscow (1969).
6. A. K. Krasin, Reactors of Atomic Power Stations [in Russian], Izd-vo Nauka i Tekhnika, Minsk (1971).
7. V. B. Nesterenko, Proceedings of the All-Union Conference on Dissociating Gases as Coolants and Working Fluids of Power Installations [in Russian], Izd-vo Nauka i Tekhnika, Minsk (1970), p. 11.
8. Thermodynamic and Transfer Properties of Chemically Reacting Gaseous Systems [in Russian], A. K. Krasin and V. B. Nesterenko (editors), Izd-vo Nauka i Tekhnika, Minsk, Part I (1967); Part II (1971).
9. V. B. Nesterenko, Physicotechnological Foundations of the Use of Dissociating Gases as Coolants and Working Fluids at Atomic Power Stations [in Russian], Izd-vo Nauka i Tekhnika, Minsk (1971).
10. V. B. Nesterenko et al., Izv. AN BSSR, Seriya Fiz.-Énerg. Nauk, 3, 5 (1971).

CHOOSING ABSORBING-ROD EFFICIENCY FOR SHIELDING AGAINST EXCESSIVE POWER LEVELS

A. A. Sarkisov, V. N. Puchkov, and B. A. Mel'nikov

UDC 621.039.566.8

Most of the emergency shielding (ES) algorithms in use specify reactor shutdown when an excessive power level is signalled. This has two extremely undesirable effects: 1) significant thermal stresses arise in the core structural elements; this has a negative effect on their reliability; 2) restarting the reactor takes a great deal of time which significantly decreases the installation's adjustability.

It is known that most cases of triggering the shielding when excessive power is signalled are caused by reactivity release when the control system malfunctions or by errors made by personnel.

In several cases when the reactivity release is caused by moving the controls it is possible when the power is exceeded to a certain extent to stop the action of the source of disturbance by inserting an interlock into the absorber control circuit. Then, to end the emergency situation, instead of shutting down the reactor, one can rapidly insert into the core absorbing rods whose efficiency is equal to the magnitude of the released reactivity. Functionally, these duties can be given, for instance, to the reserve regulator which is constantly in "hot" reserve. In this variant, the emergency shielding rods must play the role of an insurance unit. For this purpose, their triggering level must be increased a bit.

The main problem of this study consisted of determining the minimum efficiency for absorbing-rods which would provide reliable reactor shielding during reactivity disturbances in all cases when these rods are triggered simultaneously with stopping the effect of the source of disturbance. The study was made using the IR-100 reactor and an electronic model of reactor kinetics made on an MN-14 analog computer.

While the experiment was performed on the IR-100, an absorbing rod was located in the central experimental channel; it was moved out of the core by a special servomechanism at various constant speeds. The rod was moved in the range where its differential efficiency is practically constant. Removal of the rod began at a certain steady-state power level $N_0 = 0.5\ N_p = \text{const}$, and ended when the ES was triggered by a signal that the prescribed power N_p had been exceeded by a factor of 2. The prescribed power level was kept constant in all modes. The rate of reactivity release was varied within the limits $(8\text{-}32) \cdot 10^{-5}$ sec^{-1}.

As a result of the experiments, we obtained a family of curves determining the variation in relative reactor power as a function of the rate of reactivity release and the time. Since in all cases $\rho_0 = 0$ and the reactivity increases linearly, at any moment of time the magnitude of the released reactivity is $\dot{\rho}t$. Thus, the dependences we obtain can be given in the form $\rho = f(\dot{\rho}, N/N_0)$ (see Fig. 1).

By comparing the curves given in Fig. 1 it follows that at low rates of reactivity release the magnitude ρ corresponding to the given value of N/N_0 depends significantly on the reactivity-release rate. As $\dot{\rho}$ increases, this dependence approaches a saturation point, and becomes weaker. In connection with this, we continued the study on an electronic model of reactor kinetics, which allowed us to increase the reactivity-release rate to $68 \cdot 10^{-4}$ sec^{-1}.

When the process was described mathematically, the space distribution of neutrons in the core was disregarded and a one-group representation of the neutron spectrum was taken to be correct. The admissibility of such a simplification when studying transition processes with prolonged reactivity discontinuities

Translated from Atomnaya Énergiya, Vol. 34, No. 6, pp. 441-444, June, 1973. Original article submitted July 14, 1972.

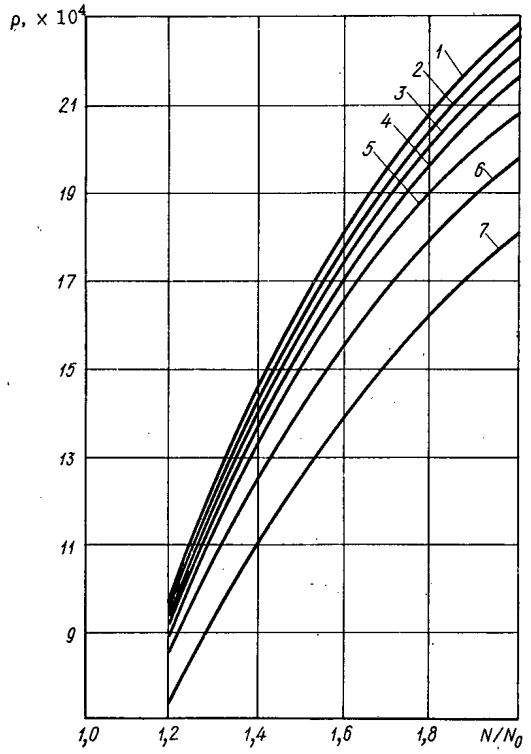

Fig. 1

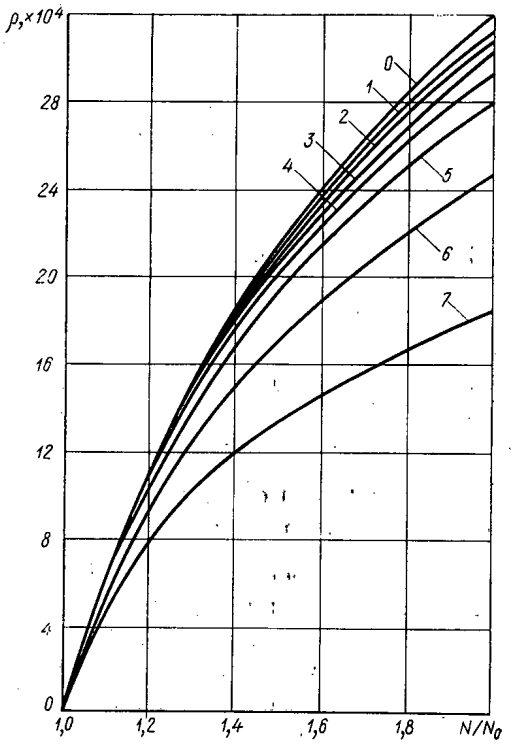

Fig. 2

Fig. 1. Dependence of the reactivity ρ released up to the time when the power increases by a factor of N/N_0, on the rate of reactivity release $\dot{\rho}$ (sec^{-1}): 1) $32 \cdot 10^{-5}$; 2) $28 \cdot 10^{-5}$; 3) $24 \cdot 10^{-5}$; 4) $20 \cdot 10^{-5}$; 5) $16 \cdot 10^{-5}$; 6) $12 \cdot 10^{-5}$; 7) $8 \cdot 10^{-5}$.

Fig. 2. Dependence of ρ released up to the time when the power increases by a factor of N/N_0 on the rate of reactivity release $\dot{\rho}$ (sec^{-1}): 0) limit; 1) $68 \cdot 10^{-4}$; 2) $56 \cdot 10^{-4}$; 3) $44 \cdot 10^{-4}$; 4) $32 \cdot 10^{-4}$; 5) $20 \cdot 10^{-4}$; 6) $8 \cdot 10^{-4}$; 7) $2 \cdot 10^{-4}$.

up to $\Delta\rho = 6 \cdot 10^{-3}$ has been shown in [1]. The differential equations have been recorded for all six groups of delayed neutrons, whose parameters were chosen in accordance with the recommendations in [2] ($\beta = 0.0064$).

The mean lifetime of prompt neutrons was taken to be $5 \cdot 10^{-5}$ sec. We did not simulate the inverse temperature relation, since we studied emergency regimes caused by releasing reactivity through removing regulating units from the core. Under such conditions, the reactivity temperature effect would only ameliorate the emergency situation by decreasing the reactivity-release rate.

The results obtained from the model were analyzed using the same method as the experimental data. The curves shown in Fig. 2 also support the fact that, beginning with certain large values of $\dot{\rho}$, the magnitude of the reactivity released up to the time when the threshold value N/N_0 is reached is practically independent of the rate of reactivity release and is determined only by the value of N/N_0. This indicates that at the limit the dependence $\rho = f(\dot{\rho}, N/N_0)$ simplifies to a relationship of the form $\rho = f(N/N_0)$, which is of greatest interest.

We can show that when we examine transient processes having durations no greater than 0.1 sec, when $N_p = N_0 = \text{const}$, and the triggering setting of the emergency-shielding system does not exceed 200-250% of N_0, then the limiting dependence in which we are interested has the form

$$\rho = \beta (1 - N_0/N). \tag{1}$$

This dependence characterizes the maximum reactivity which under the above indicated conditions can be released at the time the threshold power value is attained; it is shown in Fig. 2 as a limiting curve indicated by 0.

Thus, in the simplest case, when $N_p = N_0 = \text{const}$ and $\rho_0 = 0$, the efficiency of absorbing rods needed to compensate excess reactivity in the emergency situation under consideration can be determined from Eq. (1).

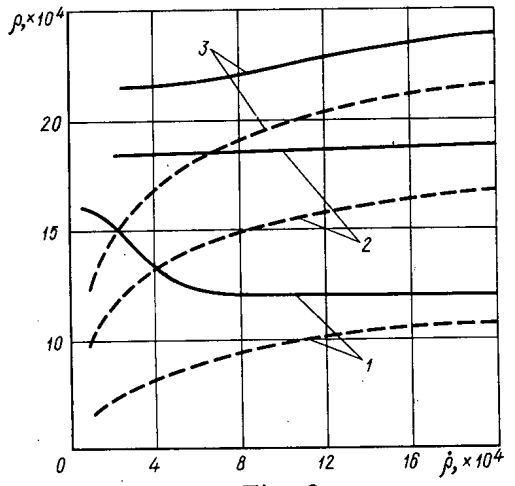

Fig. 3

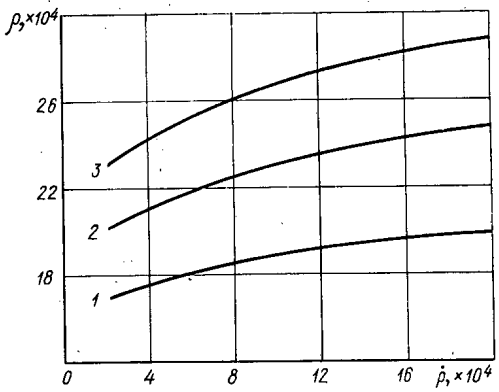

Fig. 4

Fig. 3. Dependence of reactivity ρ released when $\dot{N}_p = 5 \cdot 10^{-3}$ sec^{-1} and $\rho_0 = 0$ to the time of introducing the reserve regulator, on the value of $\dot{\rho}$ and the triggering setting: 1) $\Delta_{RR} = 0.2$; 2) 0.4; 3) 0.6.

Fig. 4. Dependence of the reactivity ρ released when $\dot{N}_p = 5 \cdot 10^{-3}$ sec^{-1} and $\rho_0 = 12 \cdot 10^{-4}$ up to the time the reserve regulator is introduced, on the value of $\dot{\rho}$ and the triggering setting: 1) $\Delta_{RR} = 0.2$; 2) 0.4; 3) 0.6.

However, in practice there may occur more complicated emergency situations in which the reactivity release when the power increases by a factor of N/N_0 exceeds the value obtained from Eq. (1). For example, if the above-studied emergency regime caused by releasing reactivity linearly is not limited by the condition N_p = const, then when $\dot{N}_p > 0$, the necessary absorbing-rod efficiency will be somewhat higher than when $\dot{N}_p$ = const. Here, the maximum reactivity release when the reserve-regulator rods are inserted will be greater, the greater the rate of increase of the prescribed power level.

To determine the absorbing-rod efficiency needed to compensate excess reactivity in the emergency system studied we can approximate the initial dependences $N/N_0 = \varphi(\dot{\rho}, t)$ by a function of the type

$$N/N_0 = \exp(k\dot{\rho}^m t^n). \tag{2}$$

The values of the coefficients, k, m, and n are determined from the composition and structure of the core as functions of β, l^*, and $\sum_{i=1}^{6} \beta_i t_i$.

The efficiency of the reserve-regulator rods is defined as the product $\dot{\rho}t$, where t is the time from the start of the emergency process until the insertion of the rods, which can be found from the relationship

$$e^{k\dot{\rho}^m t^n} - \frac{N_{p_0} + \dot{N}_p t}{N_{p_0}} = \Delta_{RR} \tag{3}$$

Here, Δ_{RR} is the setting for inserting the reserve-regulator rods.

The calculations using the method described were made in accordance with the modeled reactor. Here, the rate of power increase was taken to be 0.5% per second in the calculations. In Fig. 3, the solid curves show the results of calculations for three values of Δ_{RR} with $\dot{N}_p = 5 \cdot 10^{-3}$ sec^{-1}. For comparison, we show by dashed lines on the same figure the dependences $\rho = f(\dot{\rho}, N/N_0)$ when N_p = const.

The emergency situation examined can be made more rigorous if we assume that at the time the imbalance between N and N_p appeared the reactivity was nonzero ($\rho_0 \neq 0$), but corresponded to some value causing reactor excursion with maximum allowable period. In this case, the necessary reserve-regulator-rod efficiency can be determined from

$$\rho_{RR} = \rho_0 + \dot{\rho}t. \tag{4}$$

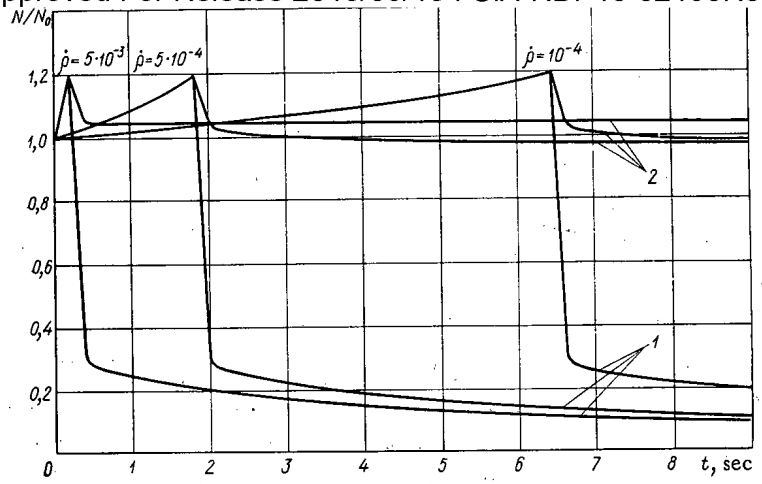

Fig. 5. Transient processes when absorbing rods having efficiencies $20 \cdot 10^{-3}$ (curve 1) and $1.1 \cdot 10^{-3}$ (curve 2) are actuated.

The time t from the start of the mismatch between the prescribed and actual power levels, as in the previous case, can be found from Eq. (3), but the values of the coefficients k, m, and n in Eq. (2) must, in this case, be changed according to the initial reactivity ρ_0. Besides this, the values of N_0 and N_{p0} are here taken not at the start of the transient process, but at the instant N_p is exceeded.

Figure 4 shows results of calculating the maximum values of reactivity released to the time when the power increases to $(N/N_0)^*$ equal to 1.2, 1.4, and 1.6, when $\dot{N}_p = 5 \cdot 10^{-3}$ sec^{-1} and $\rho_0 = 12 \cdot 10^{-4}$. All calculations were made in accordance with the modeled reactor.

Comparison of the curves in Figs. 3 and 4 shows that the greatest reactivity can be released when ρ_0 corresponds to the maximum allowable period and the given power in the transient process increases at a maximal rate. However, in this case even when $(N/N_0)^* = 1.6$, the necessary reserve-regulator rod efficiency is only $2.88 \cdot 10^{-3}$. This allows us to conclude that, to eliminate the studied emergency situations caused by release of reactivity, we can effectively use relatively "light" absorbing rods.

To illustrate the advantages of the suggested reactor-shielding method during reactivity disturbances, we made two series of calculations on an electronic model. In both cases, from the initial state $\rho_0 = 0$ reactivity was released at rates of 10^{-4}, $5 \cdot 10^{-4}$, and $5 \cdot 10^{-3}$ sec^{-1}. However, in the first variant, when the prescribed power level was exceeded by 20%, "heavy" emergency shielding rods were actuated, having a total "weight" of $20 \cdot 10^{-3}$; the second variant used "light" absorbing rods whose efficiency was $1.1 \cdot 10^{-3}$, determined from Eq. (1).

It is clear from Fig. 5 that in the emergency regimes examined, the use of "light" absorbing rods instead of the traditional system of shutting down the reactor allows one to ensure reliable shielding of the reactor from accidentally exceeding the prescribed power level while minimizing thermal stresses. Besides this, triggering of the reserve regulator in this case practically does not interfere with the prescribed working regime of the power station.

LITERATURE CITED

1. I. I. Sidorova, Analog Modeling in Nuclear Technology [in Russian], Atomizdat, Moscow (1969).
2. G. Keepin et al., Phys. Rev., 107, 1044 (1957).

NEUTRON TRANSPORT EQUATION SUITABLE FOR OBTAINING APPROXIMATE THERMALIZATION EQUATIONS

N. I. Laletin

UDC 539.125.52:621.039.51.12

It often proves useful to convert an equation describing some physical process into an equivalent equation which, in some specific sense, is more convenient. The usual procedure for such a conversation is as follows. The operator $\hat{A}$ of the original equation $\hat{A}f = S'$ is divided into a sum of two $\hat{A} = \hat{A}_0 + \hat{B}$. If there exists an operator A_0^{-1} reciprocal (inverse) to $\hat{A}_0$, then for the unknown function f we have an equation

$$f = \hat{A}_0^{-1}S - \hat{A}_0^{-1}Bf.$$

Examples of this kind of transformation include the following: in quantum mechanics, the derivation of the integral form of Schrödinger's equation from the differential form [1]; in the theory of neutron transport, the derivation of the Wigner–Weinberg–Corngold–Orlov equation [3-4] and the Peierls equation [2] from the Boltzmann relationship. This kind of transformation will be useful if we make a successful choice of $\hat{A}_0$, i.e., essentially if we choose an operator reasonably characteristic of the group of problems evoking our particular interest.

When considering the thermalization of neutrons this type of transformation requires a certain modification. We have to start by choosing a characteristic solution, and in this regard cannot dispense with physical considerations.

Let us consider the very simple problem of the energy spectrum of the slow neutrons arising from a monoenergetic, spatially-uniform source in an infinite homogeneous medium [5]. The equation for this case takes the form

$$[\Sigma_a(\varepsilon) + \Sigma_s(\varepsilon)]\,\Phi(\varepsilon) = \int_0^\infty \Sigma_s(\varepsilon' \to \varepsilon)\,\Phi(\varepsilon')\,d\varepsilon' + \delta(\varepsilon - \varepsilon_1). \tag{1}$$

Here $\varepsilon = E/kT$ is the energy E of the neutrons in units of kT, where T is the temperature of the medium and k is Boltzmann's constant, $\Phi(\varepsilon)$ is the neutron flux of energy ε, $\Sigma_a(\varepsilon)$ and $\Sigma_s(\varepsilon)$ are the macroscopic neutron absorption and inelastic scattering cross sections, $\Sigma_s(\varepsilon' \to \varepsilon)$ is the scattering cross section of a neutron with energy ε' in the range close to the energy ε, $\delta(x)$ is the Dirac δ-function, ε_1 is the energy of the source neutrons. We shall consider that

$$\varepsilon_1 \gg 1.$$

Let us rewrite Eq. (1):

$$\frac{dQ}{d\varepsilon} = \Sigma_a(\varepsilon)\,\Phi(\varepsilon) - \delta(\varepsilon - \varepsilon_1), \tag{2}$$

where we have introduced the nomenclature

$$Q(\varepsilon) = \int_0^\varepsilon d\varepsilon'' \int_\varepsilon^\infty d\varepsilon' \Sigma_s(\varepsilon' \to \varepsilon'')\,\Phi(\varepsilon') - \int_\varepsilon^\infty d\varepsilon'' \int_0^\varepsilon d\varepsilon' \Sigma_s(\varepsilon' \to \varepsilon'')\,\Phi(\varepsilon'). \tag{3}$$

We see from the foregoing equation that $Q(\varepsilon)$ is the generalized slowing-down density for the case in which the nuclei are moving. It is natural to call $Q(\varepsilon)$ the current along the energy axis.

Translated from Atomnaya Énergiya, Vol. 34, No. 6, pp. 445-449, June, 1973. Original article submitted April 17, 1972.

As auxiliary functions for the transformation of Eq. (2) we take the solution to the equation

$$\frac{dQ}{d\varepsilon}=0.$$

One solution corresponding to $Q(\varepsilon) \equiv 0$ is the equilibrium distribution $M(\varepsilon) = \varepsilon e^{-\varepsilon}$. Another solution will be the function for which $Q(\varepsilon) = \text{const} \neq 0$ (without reducing generality we may take the constant as 1).

Let us denote this solution by $I(\varepsilon)$ and present the basic information relating to it which will be needed for the future.

In the slowing-down range ($\varepsilon \gg 1$) $I(\varepsilon)$ will transform into the well-known Fermi spectrum $I(\varepsilon) \sim 1/\xi_0\Sigma_S\varepsilon$. Here ξ_0 is the logarithmic mean of the energy loss in a collision with a stationary nucleus. Generally speaking, the function $I(\varepsilon)$ may be divided into two parts: $I(\varepsilon) = -(\delta(\varepsilon)/\Sigma_S(\varepsilon)) + I_r(\varepsilon)$, where $I_r(\varepsilon)$ is the regular component of the solution. This component is accurately defined apart from the addition of a Maxwell function with an arbitrary factor. It is therefore more convenient to deal with the function

$$i(\varepsilon)=\frac{d}{d\varepsilon}[I_r(\varepsilon)/M(\varepsilon)].$$

Making allowance for the behavior of $i(\varepsilon)$ at $\varepsilon \gg 1$ we introduce the new function

$$z(\varepsilon)=e^{\varepsilon}\int_{\varepsilon}^{\infty} i(\varepsilon')\,e^{-\varepsilon'}\,d\varepsilon'.$$

Then $i(\varepsilon) = z(\varepsilon) - (d/d\varepsilon)z(\varepsilon)$.

Since in the limiting cases of the gas model ($m = 1$ and $m \gg 1$ where m is the mass number of the slowing-down nucleus) the function $z(\varepsilon)$ may be expressed by a unique formula [6]

$$z_{g.m}(\varepsilon)=\frac{1}{\xi_0\Sigma_s(\varepsilon)M(\varepsilon)};$$

it is reasonable in the general case to express $z(\varepsilon)$ in the form

$$z(\varepsilon)=\frac{1+t(\varepsilon)}{\xi_0\Sigma_s(\varepsilon)M(\varepsilon)}.$$

It is easy to show that $t(\varepsilon)$ satisfies an integral equation of the second kind which may be solved numerically by standard methods. Hence $t(\varepsilon) \equiv 0$ for a gas with $m = 1$ while for a gas with $m \gg 1$ this function only differs appreciably from zero for $\varepsilon < 1/m$.

We note that in the expression for $z(\varepsilon)$ the quantity $t(\varepsilon)$ enters in the combination $\xi_0\Sigma_S(\varepsilon)/[1 + t(\varepsilon)]$. Let us introduce the quantity $\xi(\varepsilon) = \xi_0/[1 + t(\varepsilon)]$. We may assume that this in some way characterizes the width of the distribution of singly-scattered neutrons having an energy ε before collision.

Using the two characteristic solutions of $M(\varepsilon)$ and $I(\varepsilon)$ at our disposal we may transform the original kinetic equation (1). In the formal procedure under consideration, the first step is that of separating out an operator $\hat{A}_0$ determined by the characteristic solutions. In the present case a suitable operator will be

$$\hat{A}_0 f=\int_0^{\infty}\Sigma_s(\varepsilon'\to\varepsilon)f(\varepsilon')\,d\varepsilon'-\Sigma_s(\varepsilon)f(\varepsilon).$$

However, there is no continuous reciprocal operator A_0^{-1} in the class of functions satisfying the natural physical requirements, since there is no solution to the equation

$$\int_0^{\infty}\Sigma_s(\varepsilon'\to\varepsilon)f(\varepsilon')\,d\varepsilon'-\Sigma_s(\varepsilon)f(\varepsilon)=-\delta(\varepsilon-\varepsilon_1).$$

Physically this is readily understandable, being due to the fact that there can be no steady-state neutron distribution in an infinite nonabsorbing medium with a constantly acting source. However, a solution exists for the equation

$$\int_0^{\infty}\Sigma_s(\varepsilon'\to\varepsilon)f(\varepsilon')\,d\varepsilon'-\Sigma_s(\varepsilon)f(\varepsilon)=\delta(\varepsilon-\varepsilon_0)-\delta(\varepsilon-\varepsilon_1), \tag{4}$$

and this will be used later. This solution is defined apart from the addition of a Maxwell function with an arbitrary factor. Apart from obvious physical considerations we may use a formal mathematical argument as a verification of the existence of a solution to Eq. (4). It is well known that, if a homogeneous equation $\hat{A}_0 f = 0$ has a nontrivial solution, the corresponding inhomogeneous equation $\hat{A}_0 f = \varphi$ will only have a solution if the right-hand side of the equation $\varphi(x)$ is orthogonal to the solution of the conjugate homogeneous equation $\hat{A}_0^+ f^+ = 0$. Since in the present case the solution of the conjugate equation

$$\hat{A}^+ f^+ = \int_0^\infty \Sigma_s (\varepsilon \to \varepsilon') [f^+ (\varepsilon') - f^+ (\varepsilon)] \, d\varepsilon' = 0$$

is constant, it is required that the integral of the right-hand side of Eq. (4) should vanish, and this is indeed the case.

In order to simplify the calculations we may put $\varepsilon_1 \to \infty$ into Eq. (4), although this will not reduce the generality of the consideration. The solution of the equation so obtained we call $G(\varepsilon/\varepsilon_0)$. Since the left-hand side of Eq. (4) is the quantity $dQ/d\varepsilon$, it is easy to show that $Q = 0$ for $\varepsilon < \varepsilon_0$ and $Q = 1$ for $\varepsilon > \varepsilon_0$. We then proceed as follows. On considering the energy range $\varepsilon < \varepsilon_0$, we may reasonably assume that, if the neutron sink situated at $\varepsilon = \varepsilon_0$ in the problem is displaced in the direction of infinite energies, then this will only make an appreciable difference to the solution in the energy range of present interest in the immediate vicinity of $\varepsilon = \varepsilon_0$, i.e., the chief component of the solution $G(\varepsilon/\varepsilon_i)$ for $\varepsilon < \varepsilon_0$ will be the Maxwell function $M(\varepsilon)$. An analogous discussion when considering the range $\varepsilon > \varepsilon_0$ strongly suggests that the chief component of the solution will in this case be $I(\varepsilon)$. Guided by these considerations, we express $G(\varepsilon/\varepsilon_0)$ in the form

$$G(\varepsilon/\varepsilon_0) = \frac{g(\varepsilon/\varepsilon_0)}{\Sigma_s(\varepsilon)} - \frac{\delta(\varepsilon-\varepsilon_0)}{\Sigma_s(\varepsilon)} + \begin{cases} C_1(\varepsilon_0) M(\varepsilon), & \varepsilon < \varepsilon_0; \\ C_2(\varepsilon_0) M(\varepsilon) + I(\varepsilon), & \varepsilon \geqslant \varepsilon_0. \end{cases} \tag{5}$$

After requiring that the equation $C_1(\varepsilon_0) M(\varepsilon_0) = C_2(\varepsilon_0) M(\varepsilon_0) + I(\varepsilon_0)$ should be satisfied, we are left with only one arbitrary function. We rewrite the expression for $G(\varepsilon/\varepsilon_0)$

$$G(\varepsilon/\varepsilon_0) = \frac{g(\varepsilon/\varepsilon_0)}{\Sigma_s(\varepsilon)} - \frac{\delta(\varepsilon-\varepsilon_0)}{\Sigma_s(\varepsilon)} + C(\varepsilon_0) M(\varepsilon) + \begin{cases} 0, & \varepsilon < \varepsilon_0; \\ I(\varepsilon) - \dfrac{I(\varepsilon_0)}{M(\varepsilon_0)} M(\varepsilon), & \varepsilon \geqslant \varepsilon_0. \end{cases}$$

Equation (5) signifies that, instead of the unknown function $G(\varepsilon/\varepsilon_0)$, we have introduced the unknown function $g(\varepsilon/\varepsilon_0)$. The usefulness of this change depends on how valid are the considerations serving as a basis for Eq. (5).

Substituting (5a) into (4) and making a number of transformations, we obtain an equation for $g(\varepsilon/\varepsilon_0)$

$$\int_0^\infty g(\varepsilon'/\varepsilon_0) \frac{\Sigma_s(\varepsilon' \to \varepsilon)}{\Sigma_s(\varepsilon')} \, d\varepsilon' - g(\varepsilon/\varepsilon_0) = S(\varepsilon/\varepsilon_0). \tag{6}$$

The expression for $S(\varepsilon/\varepsilon_0)$ takes the form

$$S(\varepsilon/\varepsilon_0) = \frac{\Sigma_s(\varepsilon_0 \to \varepsilon)}{\Sigma_s(\varepsilon_0)} - \begin{cases} \displaystyle\int_{\varepsilon_0}^\infty \left[I(\varepsilon') - \frac{I(\varepsilon_0)}{M(\varepsilon_0)} M(\varepsilon') \right] \\ \quad \times \Sigma_s(\varepsilon' \to \varepsilon) \, d\varepsilon', \quad \varepsilon < \varepsilon_0; \\ \displaystyle\int_0^{\varepsilon_0} \left[\frac{I(\varepsilon_0)}{M(\varepsilon_0)} M(\varepsilon') - I(\varepsilon') \right] \\ \quad \times \Sigma_s(\varepsilon' \to \varepsilon) \, d\varepsilon', \quad \varepsilon > \varepsilon_0. \end{cases}$$

It is easy to see that $S(\varepsilon/\varepsilon_0)$ is an alternating function only differing from zero in a narrow range of energies ε close to the value ε_0 (in the region of the energy transferred by a neutron in a single collision). The integral of $S(\varepsilon/\varepsilon_0)$ with respect to ε equals zero

$$\int_0^\infty S(\varepsilon/\varepsilon_0) \, d\varepsilon = 0.$$

The function $g(\varepsilon/\varepsilon_0)$ is not determined uniquely by Eq. (6). In order to avoid the indeterminacy, we transform Eq. (6) by means of (5a), assuming $C(\varepsilon_0) = \text{const} = C$ in the latter.

We obtain an equation

$$g(\varepsilon/\varepsilon_0) - \int_0^\infty S(\varepsilon'/\varepsilon_0) \, g(\varepsilon/\varepsilon') \, d\varepsilon' = h(\varepsilon/\varepsilon_0).$$

Here

$$h(\varepsilon/\varepsilon_0) = -S(\varepsilon/\varepsilon_0) + \Sigma_s(\varepsilon) M(\varepsilon) \int_0^{\varepsilon} S(\varepsilon'/\varepsilon_0) \int_{\varepsilon'}^{\varepsilon} i(\varepsilon'')\, d\varepsilon''\, d\varepsilon'.$$

The function $g(\varepsilon/\varepsilon_0)$ so defined is alternating, the interval over which it deviates appreciably from zero being similar to the corresponding interval for $S(\varepsilon/\varepsilon_0)$. For $\varepsilon \gg 1$ we have

$$g(\varepsilon/\varepsilon_0) \sim \left[\frac{1}{\xi_0 \varepsilon} - \frac{1}{\varepsilon_0} P_A\left(\frac{\varepsilon}{\varepsilon_0}\right)\right] \chi(\varepsilon_0 - \varepsilon).$$

where $P_A(x)$ is the Placzek function [4], $\chi(x) = \begin{cases} 1, & x \geqslant 0; \\ 0, & x < 0 \end{cases}$ is the Heaviside function.

For a gas with m = 1 we have $g(\varepsilon/\varepsilon_0) \equiv 0$. We now use Eq. (5a) to transform Eq. (1). We write this in the form

$$\int_0^{\infty} \Sigma_s(\varepsilon' \to \varepsilon)\, \Phi(\varepsilon')\, d\varepsilon' - \Sigma_s(\varepsilon)\, \Phi(\varepsilon) = \Sigma_a(\varepsilon)\, \Phi(\varepsilon) - \delta(\varepsilon - \varepsilon_1).$$

The right-hand side of this equation may be written as follows

$$\int_0^{\infty} \Sigma_a(\varepsilon')\, \Phi(\varepsilon')\, [\delta(\varepsilon - \varepsilon') - \delta(\varepsilon - \varepsilon_1)]\, d\varepsilon'.$$

This form of writing is permissible since $\int_0^{\infty} \Sigma_a(\varepsilon)\Phi(\varepsilon)d\varepsilon = 1$. Putting $\varepsilon_1 \to \infty$ we obtain

$$\Phi(\varepsilon) = \int_0^{\infty} G(\varepsilon/\varepsilon')\, \Sigma_a(\varepsilon')\, \Phi(\varepsilon')\, d\varepsilon'.$$

If in this we substitute the expression for $G(\varepsilon/\varepsilon')$ in (5a) we obtain

$$\Phi(\varepsilon) = \int_0^{\infty} g(\varepsilon/\varepsilon') \frac{\Sigma_a(\varepsilon')}{\Sigma_s(\varepsilon)} \Phi(\varepsilon')\, d\varepsilon' - \frac{\Sigma_a(\varepsilon)}{\Sigma_s(\varepsilon)} \Phi(\varepsilon)$$

$$+ CM(\varepsilon) \int_0^{\infty} \Sigma_a(\varepsilon')\, \Phi(\varepsilon')\, d\varepsilon' + \int_0^{\varepsilon} \left[I(\varepsilon) - \frac{I(\varepsilon')}{M(\varepsilon')} M(\varepsilon)\right] \Sigma_a(\varepsilon')\, \Phi(\varepsilon')\, d\varepsilon'.$$

Transforming the last integral on the right, we arrive at the equation

$$\Phi(\varepsilon) = M(\varepsilon)\left[C + \int_0^{\varepsilon} i(\varepsilon')\, Q(\varepsilon')\, d\varepsilon'\right]$$

$$+ \frac{1}{\Sigma_s(\varepsilon)}\left[\int_0^{\infty} g(\varepsilon/\varepsilon') \frac{dQ}{d\varepsilon'} d\varepsilon' - \frac{dQ}{d\varepsilon}\right]. \qquad (7)$$

Here $i(\varepsilon') = (d/d\varepsilon')[I_p(\varepsilon')/M(\varepsilon')]$, $Q(\varepsilon)$ is the current along the energy axis, equal in the present case to $Q(\varepsilon) = \int_0^{\varepsilon} \Sigma_a(\varepsilon')\Phi(\varepsilon')d\varepsilon'$. The constant C is determined from the condition $\int_0^{\infty} \Sigma_a(\varepsilon')\Phi(\varepsilon')d\varepsilon' = 1$, i.e.,

$$C = \frac{1}{\Sigma_s}\left(1 + \int_0^{\infty} [\Sigma_s \Phi(\varepsilon) - \Sigma_s M(\varepsilon) \int_0^{\varepsilon} i(\varepsilon')\, Q(\varepsilon')\, d\varepsilon']\, d\varepsilon - \bar{g}\right). \qquad (8)$$

Here $\bar{\Sigma}_s = \int_0^{\infty} \Sigma_s(\varepsilon) M(\varepsilon) d\varepsilon$ is the scattering cross section averaged with respect to the Maxwell spectrum, while $\bar{g} = \int_0^{\infty} d\varepsilon \int_0^{\infty} d\varepsilon' g(\varepsilon/\varepsilon') \Sigma_a(\varepsilon') \Phi(\varepsilon')$. The integral in Eq. (8) exists because, although $\Sigma_s(\varepsilon)\Phi(\varepsilon) \sim 1/\xi_0\varepsilon$ as $\varepsilon \to \infty$, yet in view of the fact that $Q(\varepsilon) \to 1$ as $\varepsilon \to \infty$ the second term in the integrand behaves in the following way as $\varepsilon \to \infty$

$$\Sigma_s(\varepsilon)\, M(\varepsilon) \int_0^{\varepsilon} i(\varepsilon')\, Q(\varepsilon')\, d\varepsilon' \sim \Sigma_s(\varepsilon)\, M(\varepsilon) \frac{I(\varepsilon)}{M(\varepsilon)} \sim \frac{1}{\xi_0 \varepsilon}$$

and the whole integrand falls off more rapidly than $1/\varepsilon$.

Together with Eq. (8), Eq. (7) is exactly equivalent to Eq. (1). Let us compare them. Information as to the scattering of the neutron by the target nuclei, which appeared in (1), in the form of the cross section $\Sigma_s(\varepsilon' \to \varepsilon)$, now appears in two functions: $i(\varepsilon')$ and $g(\varepsilon/\varepsilon')$. The chief part is played by the function $i(\varepsilon')$, which depends simply on one variable and enters into an integral with a variable upper limit. If we further compare the integral $\int_0^\infty \Sigma_a \Phi(\varepsilon') g(\varepsilon/\varepsilon') d\varepsilon'$ with the collision integral of Eq. (1) $\int_0^\infty \Sigma_s(\varepsilon' \to \varepsilon)\Phi(\varepsilon')d\varepsilon'$, we see that the former is as a rule the smaller, since it depends on the absorption density and not on the scattering density, and also because of the fact that $g(\varepsilon/\varepsilon')$, unlike $\Sigma_s(\varepsilon' \to \varepsilon)$, is an alternating function. We also note that in Eq. (7) the "trivial" Maxwell part of the solution is separated out, so that attention may be concentrated upon the deviations from the Maxwell distribution. This makes Eq. (7) more convenient for a qualitative analysis of the solution.

As already mentioned, the assumption so far made, to the effect that the energy of the source neutrons is infinitely great, does not constitute any limitation. It may, in particular, be shown that Eq. (7) remains valid for a neutron source described by the function $S(\varepsilon)$, whereupon the current along the energy axis $Q(\varepsilon)$ should be written

$$Q(\varepsilon) = \int_0^\varepsilon [\Sigma_a(\varepsilon')\Phi(\varepsilon') - S(\varepsilon')]\, d\varepsilon'.$$

Using Eq. (7) it is easy [7] to obtain all the well-known approximate thermalization equations. For this it is essential to approximate the integral $\int_0^\infty g(\varepsilon/\varepsilon')\Sigma_a\Phi(\varepsilon')d\varepsilon'$ in some suitable manner.

Let us rewrite Eq. (7):

$$\Phi(\varepsilon) = \frac{1}{\Sigma_a(\varepsilon)} \frac{d}{d\varepsilon}\left[\frac{1}{i(\varepsilon)}\frac{d}{d\varepsilon}\left(\frac{\Phi(\varepsilon)}{M(\varepsilon)} + \frac{\gamma(\varepsilon_1\Phi)\,\Sigma_a\Phi(\varepsilon)}{\xi_0\Sigma_s(\varepsilon)M(\varepsilon)}\right)\right].$$

Here

$$\gamma(\varepsilon_1\Phi) = \xi_0\left(1 - \frac{\int \bar{g}(\varepsilon_1\varepsilon')\,\Sigma_a(\varepsilon')\,\Phi(\varepsilon')\,d\varepsilon'}{\Sigma_a(\varepsilon)\,\Phi(\varepsilon)}\right).$$

If we consider that $(\int g(\varepsilon/\varepsilon')\Sigma_a\Phi(\varepsilon')d\varepsilon')/(\Sigma_a\Phi(\varepsilon)) \approx g_1(\varepsilon)$, Eq. (10) transforms into a differential equation of the second order. Using the expression for $\Sigma_s(\varepsilon)$ obtained with the gas model, and expanding all the quantities in Eq. (10) in powers of 1/m, we obtain the Wilkins [8] and Corngold [9] equations. Here the conditions $\varepsilon > 1/m$ and $\Sigma a(1)/\xi_0\Sigma_0 \ll 1$ have to be satisfied.

If in Eq. (10) we put

$$z(\varepsilon) = \frac{1}{\xi_0\Sigma_s(\varepsilon)M(\varepsilon)}\left[i(\varepsilon) = z(\varepsilon) - \frac{d}{d\varepsilon}z(\varepsilon)\right];$$

$$\Sigma_s(\varepsilon) = \Sigma_0\left[\left(1 + \frac{1}{2m\varepsilon}\right)\operatorname{erf}\sqrt{m\varepsilon} + \frac{e^{-m\varepsilon}}{\sqrt{\pi m\varepsilon}}\right];$$

$$\gamma(\varepsilon\Phi) = \gamma_0 = 1 - \frac{1}{2}\frac{\alpha(\ln\alpha)^2}{(1-\alpha)\xi_0}, \quad \alpha = \left(\frac{m-1}{m+1}\right)^2,$$

we obtain an equation incorporating three limiting cases: the Wigner–Wilkins equation for m = 1 and the Wilkins and Corngold equations for $m \gg 1$. This equation, which was earlier proposed in [6], should thus give reasonable results for a gas of any arbitrary mass.

If the functions $i(\varepsilon)$ and $\gamma(\varepsilon)$ are chosen so that, in a medium of low absorption behaving as $1/\sqrt{\varepsilon}$, the approximate equation should give a solution as close as possible to the solution of the exact equation, we obtain the equation of the "generalized heavy-gas model" [10, 11] and that of the "secondary" model [11]. Furthermore, Eq. (10) enables us to derive formulas providing a more reliable determination of the functions $i(\varepsilon)$ and $\gamma(\varepsilon)$ than those of [10, 11].

Of the two functions entering into the approximate equations under consideration, the principal part is, of course, played by the function $i(\varepsilon)$ for all energies ε, and especially for $\varepsilon \gg 1$, where its role becomes dominant. In media with not too strong an absorption, however, the function $\gamma(\varepsilon)$ only affects the behavior of the solution for $\varepsilon \ll 1$, when the Maxwell component of the solution plays the major part. The weak dependence of the neutron spectra on the function $\gamma(\varepsilon)$ in media with an absorption cross section varying as $1/\sqrt{\varepsilon}$ is demonstrated by the results of the calculations in [10, 12]. However, if the absorption varies

in a resonance manner, the role of the function $\gamma(\varepsilon)$ becomes more important. This may be seen from the corresponding curves of [11, 12].

These considerations served as a basis for the proposition that the thermalization of neutrons in water should be described by means of a two-constant model [12]. In choosing the function $\xi(\varepsilon)\Sigma_s(\varepsilon) = \text{const}$ allowance was made for the fact (noted by many research workers) that the neutron spectra in water with an absorber varying as $1/\sqrt{\varepsilon}$ were excellently described by the "heavy-gas" model. The function $\gamma(\varepsilon)$ was introduced so that the model should also satisfactorily describe thermalization in water with a resonance absorber. Since all the "interesting" resonances in the absorption cross sections lie in the range $\varepsilon \gg 1$, the simplest relationship $\gamma(\varepsilon) = \gamma_0 = 1$ was chosen. As we have just shown, this simple model gives a completely acceptable accuracy.

In conclusion, we note that there is no difficulty in carrying out a transformation similar to the one of the present analysis for an equation with the spatial dependence of [7].

LITERATURE CITED

1. D. Schiff, Quantum Mechanics [Russian translation], IL, Moscow (1957).
2. B. Davison, Theory of Neutron Transport [Russian translation], Atomizdat, Moscow (1960).
3. N. Corngold, Proc. Phys. Soc., A70, 793 (1957).
4. A. Weinberg and E. Wigner, Physical Theory of Nuclear Reactors [Russian translation], IL, Moscow (1961).
5. N. I. Laletin, Preprint IAÉ-2146 (1971).
6. N. I. Laletin, At. Énerg., 14, 458 (1963).
7. N. I. Laletin, Preprint IAÉ-2145 (1971).
8. E. Cohen (USA), First Geneva Conference (1955), Paper No. R/611.
9. N. Corngold, Ann. Phys., 6, 368 (1959).
10. H. Pitcher, AEEW-M-350 (1963).
11. M. Cadilhac et al., BNL-719 (c-32), Vol. 2 (1962), p. 439; in: Thermalization of Neutrons [Russian translation], Atomizdat, Moscow (1964); M. Cadilhac et al. (France), Third Geneva Conference (1964), Paper No. R/73.
12. N. I. Laletin, At. Énerg., 17, 193 (1964).

EFFECT OF SCATTERING ANISOTROPY ON THE THERMAL-NEUTRON USE FACTOR

N. I. Laletin, N. V. Sultanov,
Yu. A. Vlasov, and S. I. Konyaev

UDC 621.039:512.4

In calculating the use factor of the thermal neutrons in a heterogeneous reactor, anisotropic scattering is usually taken into account in only a very coarse manner. The transport approximation [1] is nearly always used, and only sometimes the linearly-anisotropic approximation [1, 2]. In these approximations the zeroth and first angular moments of the scattering indicatrix are correctly taken into account, but the higher moments are distorted. In the transport approximation all the angular moments with numbers $n \geq 2$ are regarded as being equal to the first angular moment, while in the linearly-anisotropic approximation they are put equal to zero.

The general opinion to the effect that such a distortion would not lead to any serious errors in the thermal-neutron use factor was recently questioned [3]. When calculating certain two-zone plane cells, Eccleston and McCormick [3] observed that allowance for the second angular moment of the scattering indicatrix led to a change in the disadvantage factor comparable in magnitude with the corresponding change associated with the first angular moment. In addition to this, both changes were of the same sign.

If these conclusions [3] are valid, then in calculating uranium–water cells it is extremely vital to allow for the second angular moment of the scattering indicatrix. We note that for many of the methods employed this implies serious complication of the computing process.

The validity of the results presented in [3], however, arouses serious misgivings. It was in fact shown in [4, 5]* that

$$\Theta_1 - \Theta_0 = \Sigma_{am} V_m \Sigma_{sm}^{(1)} 3 \int_{V_m} \Psi_{m,0}^{(1)} \Psi_{m,1}^{(1)} \, d\bar{r}. \tag{1}$$

Here Θ_0 and Θ_1 are the thermal-neutron use factors on the isotropic and linearly-anisotropic approximations respectively†; Σ_{am} is the absorption cross section in the moderator; V_m is the volume of the moderator; $\Sigma_{sm}^{(1)}$ is the first angular moment of the scattering cross section in the moderator; $\Psi_{m,0}^{(1)}$ and $\Psi_{m,1}^{(1)}$ are the first angular moments of the neutron distribution function in the moderator calculated on the isotropic ($\Psi_{m,0}^{(1)}$) and linearly-anisotropic ($\Psi_{m,1}^{(1)}$) approximations.

By $\Psi^{(n)}$ we understand $2n + 1$-component vectors with components $\Psi^{(n),k} = \int \Psi(\bar{r}, \bar{\Omega}) P_n^k(\bar{\Omega}\bar{r}/r) \, e^{ik\varphi} d\Omega$, while $\Psi_i^{(n)} \Psi_j^{(n)}$ is their scalar product (here $P_n^k(\mu)$ are associated Legendre polynomials with the usual normalization [6]).

If we slightly transform the equations of [4] we obtain

$$\Theta_2 - \Theta_1 \approx -\Sigma_{am} V_m 5 \Sigma_{sm} \int_{V_m} \Psi_{m,0}^{(2)} \Psi_{m,2}^{(2)} \, d\bar{r}. \tag{2}$$

*The change in the thermal-neutron use factor $\delta\Theta$ is simply related to the corresponding change in the disadvantage factor δd:

$$\left(\frac{\delta\Theta}{(1-\Theta)\Theta} = \frac{\delta d}{d} \right).$$

†Two-zone cells are here under consideration, scattering always being regarded as isotropic in the fuel.

Translated from Atomnaya Énergiya, Vol. 34, No. 6, pp. 450-454, June, 1973. Original article submitted August 22, 1972.

TABLE 1. Discrete Value of ν_0

m_{eff}	K					Transport approximation*
	0	1	2	3	4	
1	6,33192	10,87639	10,88836	10,88836	10,88836	3,71085
2,06	6,33192	7,68370	7,68501			5,22654

*The calculations on the transport approximation involve replacing Σ_s by $\Sigma_s(1-\overline{\mu})$.

TABLE 2. Rate of Convergence of G_N

G_N	G_1	G_3	G_5	G_7	G_9	G_{11}	G_{13}
d	1,0902	1,1442	1,1572	1,1611	1,1625	1,1630	1,1635 (1,1631)*

*The brackets indicate a calculation in which the integral in (3) was computed by a 27-point quadrature formula of the Gauss type.

Here Θ_2 is the thermal-neutron use factor calculated on an approximation in which the three first terms are left in the Legendre-polynomial expansion of the scattering indicatrix in the moderator, $\Sigma^{(2)}_{sm}$ is the second angular moment of the scattering cross section in the moderator, $\Psi^{(2)}_{m,2}$ is the second angular moment of the distribution function in the approximation under consideration.

It follows from Eqs. (1) and (2) that the following relationships must be satisfied for the results of [3] to be valid:

$$\left|3\Sigma^{(1)}_{sm}\int_{V_m}\Psi^{(1)}_{m,0}\Psi^{(1)}_{m,1}\,d\bar{r}\right| \approx \left|5\Sigma^{(2)}_{sm}\int_{V_m}\Psi^{(2)}_{m,0}\Psi^{(2)}_{m,2}\,d\bar{r}\right|$$

and

$$\int_{V_m}\Psi^{(2)}_{m,0}\Psi^{(2)}_{m,2}\,d\bar{r} < 0 \quad (\text{in [3] } \Sigma^{(2)}_{sm} > 0).$$

Both these are improbable. It is, in fact, most unlikely that the integral of the product of the first angular moments $\Psi(\bar{r}, \bar{\Omega})$, which are substantially different from zero over the whole moderator, would be smaller than the integral of the second moments, which only have an appreciable value close to the boundary with the fuel (in [3] $5\Sigma^{(2)}_{sm} < 3\Sigma^{(1)}_{sm}$). It is hard, furthermore, to imagine that $\Psi^{(2)}_{m,0}$ and $\Psi^{(2)}_{m,2}$, which constitute the same quantity calculated on different approximations, should differ so much that the integral of their product would be negative.

We therefore made some calculations for the cells considered in [3], and for cylindrical cells similar to them.

Calculations Based on the G_N Approximations of the Method of Surface Pseudocells

In order to study the cells in question we used the PRAKTINEP(AR) computer program. This constitutes a modification* of the PRAKTINEP program [7], differing from it in that allowance is made for scattering anisotropy. The angular moments of the plane Green's function calculated in the program take the form

*This modification and the calculations based on the PRAKTINEP(AR) program were effected by N. V. Sultanov.

TABLE 3. Disadvantage Factor

m_{eff}	K	Data of [3]		G_{11}	
		cell I	cell II	cell I	cell II
1,2·06	0	1,2317	1,6284	1,2314	1,6284
1	1	1,1634 (5,5) *	1,3599 (16,5)	1,1630 (5,6)	1,3599 (16,5)
	2	1,0664 (13,4)	1,1924 (26,8)	1,1679 (5,2)	1,3682 (16)
	4	1,0554 (14,3)	1,1752 (27,8)	1,1678 (5,2)	1,3682 (16)
2,06	1	1,1986 (2,7)	1,4988 (8)	1,1982 (2,7)	1,4989 (8)
	2	1,1405 (7,4)	1,4049 (13,7)	1,1991 (2,6)	1,5002 (7,9)

* The brackets everywhere indicate the difference between the present approximation and the isotropic approximation (in %).

$$G_{nm}(x \mid x') = \begin{cases} \sum_{i=1}^{M} \frac{A_n(\nu_i^+) A_m(\nu_i^+)}{M(\nu_i^+)} e^{-\frac{x-x'}{\nu_i^+}} + \\ + \int_0^1 \frac{A_n(\nu) A_m(\nu)}{M(\nu)} e^{-\frac{x-x'}{\nu}} d\nu \quad \text{for} \quad x > x'; \\ - \sum_{i=1}^{M} \frac{A_n(\nu_i^-) A_m(\nu_i^-)}{M(\nu_i^-)} e^{-\frac{x'-x}{\nu_i^-}} - \\ - \int_{-1}^{0} \frac{A_n(\nu) A_m(\nu)}{M(\nu)} e^{-\frac{x'-x}{\nu}} d\nu \quad \text{for} \quad x < x', \end{cases}$$

where ν_i^+ and ν_i^- are points of the discrete spectrum of ν [8]:

$$A_n(\nu) = c\nu \sum_{m=0}^{k} b_m h_m(\nu) \begin{cases} P_m(\nu) Q_n(\nu) & \text{for} \quad m \leqslant n \\ & \text{for} \quad \nu \notin [-1, 1]; \\ Q_m(\nu) P_n(\nu) & \text{for} \quad m > n \end{cases}$$

$$A_n(\nu) = P_n(\nu) + c\nu \sum_{m=0}^{\min(k, n)} b_m h_m(\nu) [P_m(\nu) Q_n(\nu) - P_n(\nu) Q_m(\nu)] \quad \text{for} \quad \nu \in [-1, 1],$$

here b_m is the coefficient from the representation of the scattering cross section in the moderator

$$\Sigma_s(\Omega\Omega) = \sum_{m=0}^{K} b_m P_m(\Omega\Omega),$$

where K is the number of the greatest moment left in the expansion of $\Sigma_s(\Omega\Omega)$, $h_m(\nu)$ is a polynomial of the m-th order [8], $M(\nu_i^{\pm})$ and $M(\nu)$ are the norms of the elementary Case solutions [8].

In obtaining the moments of the Green's function we used the elementary Case solutions with anisotropic scattering from [8]. In studying the cells we assumed that the scattering in the fuel was isotropic and in the moderator anisotropic. The effective mass of the moderator m_{eff} was either equal to 1 (allowing for the maximum scattering anisotropy) or 2.06 (allowing for anisotropy close to the real value [9]). The scattering and absorption cross sections and also the intensities of the sources were constant in each zone. The following are the data relating to the various cells.

General: $\Sigma_{tot}^{fuel} = 0.715$ cm^{-1}, $c^{fuel} = \Sigma_s/\Sigma_{tot} = 0.55370$; $\Sigma_{tot}^{mod} = 2.33$ cm^{-1}; $c^{mod} = 0.99163$.

Moderator: m = 1; $b_0 = 1$; $b_1 = 2$; $b_2 = 1.25$; $b_3 = 0$; $b_4 = -0.375$; m = 2; $b_0 = 1$; $b_1 = 0.97088$; $b_2 = 0.24428$. Cell I: thickness of fuel 0.4 cm, of moderator 0.7 cm; cell II: thickness of fuel 0.8 cm, of moderator 1.4 cm.

TABLE 4. Disadvantage Factors in the Transport Approximation

m_{eff}	G_{11}	
	cell I	cell II
1	1,1501	1,3555
	(1,1) *	(0,3)
2,06	1,1933	1,4976
	(0,4)	(0,08)

*The brackets indicate the difference between the d in the transport approximation and the d in the linearly-anisotropic approximation in percent.

In all the calculations the integral in [3] was calculated from a ten-point quadrature formula of the Gauss type. Changing to a 27-point formula made hardly any difference to the reduced disadvantage factors (in certain cases the changes amounted to one unit in the fourth place of decimals).

It is well known that the number of positive discrete values in Eq. (2) is one greater than the number of roots of the polynomial

$$1+\sum_{k=1}^{K} b_k P_k(z)\, h_k(z),$$

lying in the segment [0, 1]. In all the cells considered the number of positive discrete values of ν_i equals 1.*

The discrete value of ν_0 constituting the root of the equation [8]

$$1-c\nu\sum_{k=0}^{K} b_k Q_k(\nu)\, h_k(\nu)=0,$$

may be found by the method of dividing the segment into halves, $Q_k(\nu)$ being calculated in terms of hypergeometric function [6]. The results of our calculations of the values of ν_0 carried out with double accuracy for the moderators of the cells in question are given in Table 1 in terms of free paths. We note that the values differ somewhat from those given in [3]. The rate of convergence of the G_N approximations is indicated in Table 2. The results refer to the cell I (m_{eff} = 1, K = 1). In other cases the convergence is roughly the same (cell I) or considerably better (cell II).

We see from Table 3 that the disadvantage factors calculated by the PRAKTINEP(AR) program and by the method of [3] practically coincide in the isotropic (K = 0) and linearly-anisotropic (K = 1) approximations for scattering in the moderator, while in the remaining approximations (K = 2, 4) they differ very considerably. Not only the magnitude of the deviation from the linearly-anisotropic approximation but also its sign changes.

It follows from the PRAKTINEP(AR) calculations that the influence of scattering anisotropy on the disadvantage factor in the one-velocity approximation in plane geometry is excellently taken into account by the linearly-anisotropic approximation (for m_{eff} = 2.06 the difference is 0.1%).

Table 4 gives some calculations for the cells under consideration based on the transport approximation (replacing Σ_s by $\Sigma_s(1-\mu)$).

In addition to this, we also calculated the same cells using programs designed to solve the inhomogeneous neutron transport equations on the P_3 approximation by the method of spherical harmonics. The authors of these programs are Yu. A. Vlasov (plane geometry) and S. I. Konyaev (cylindrical geometry).

Calculations on the P_3 Approximation

The programs employed enable us to allow for the zeroth, first, second, and third moments of the scattering indicatrix and several of the first moments of the source. The mesh method forms a basis for the algorithms of this solution. The use of high-accuracy integration formulas enabled us to construct difference equations with a high degree of local approximation ([10], Chapter 7).

The system of difference equations were solved by matrix factorization, which guaranteed stability of the solution of the problem.

By way of boundary conditions, we used conditions of the Marshak–Vladimirov type. These boundary conditions are described below, taking the cases of plane and cylindrical geometry separately.

*If the transport scattering indicatrix is expanded in Legendre polynomials and limited in the expansion to two, three, and four terms for the moderator with m = 1, and three of for terms for the moderator with m = 2.06, a second discrete positive value appears.

TABLE 5. Disadvantage Factors

m_{eff}	Approximation	p_3^{pl}		p_3^{cyl}	
		cell I	cell II	cell I	cell II
1	$K=0$	1,1798	1,5801	1,1314	1,4051
	$K=1$	1,1114	1,3114	1,0900	1,2408
	$K=2$	1,1154	1,3202	1,0957	1,2575
	Transport	1,0817	1,2931	1,0683	1,2401

Plane Geometry

The one-velocity kinetic equation and the system of equations for the P_3 approximation were given in [10]. We assume that the solution $\Psi(x, \mu)$ of the kinetic equation satisfies the boundary conditions

$$\begin{aligned} \Psi(x, \mu) &= v_1(\mu) \quad \text{for} \quad \mu > 0; \\ \Psi(H, \mu) &= v_2(\mu) \quad \text{for} \quad \mu < 0. \end{aligned} \tag{4}$$

Let us set out the expansion of the solution $\Psi(x, \mu)$ in Legendre polynomials

$$\Psi(x, \mu) = \sum_{k=0}^{3} \Psi_k(x) P_k(\mu)(2k+1). \tag{5}$$

Equations (4), rewritten with due allowance for the expansion (5), are now multiplied by μ and μ^3 are integrated with respect to μ: the first from 0 to 1, the second from -1 to 0.

We accordingly obtain the relationships:

$$\left.\begin{aligned} \frac{1}{2}\Psi_0(0) + \Psi_1(0) + \frac{5}{8}\Psi_2(0) &= V1; \\ \frac{1}{4}\Psi_0(0) + \frac{3}{5}\Psi_1(0) + \frac{5}{8}\Psi_2(0) & \\ + \frac{2}{5}\Psi_3(0) &= V2; \\ -\frac{1}{2}\Psi_0(H) + \Psi_1(H) - \frac{5}{2}\Psi_2(H) &= W1; \\ -\frac{1}{4}\Psi_0(H) + \frac{3}{5}\Psi_1(H) - \frac{5}{8}\Psi_2(H) & \\ + \frac{2}{5}\Psi_3(H) &= W2; \end{aligned}\right\} \tag{6}$$

$$V1 = \int_0^1 \mu v_1(\mu)\, d\mu; \quad V2 = \int_0^1 \mu^3 v_1(\mu)\, d\mu;$$

$$W1 = \int_{-1}^0 \mu v_2(\mu)\, d\mu; \quad W2 = \int_{-1}^0 \mu^3 v_2(\mu)\, d\mu,$$

which constitute the boundary conditions for the system of equations in the P_3 approximation [10].

For the plane cell it is natural to specify the following boundary conditions

$$\begin{aligned} \frac{d\Psi_0(x)}{dx} &= 0 \quad \text{for} \quad x = 0 \quad \text{and for} \quad x = H; \\ \Psi_0(0) &= \Psi_1(H) = 0. \end{aligned} \tag{7}$$

Conditions (7) are not consequences of conditions (6), nor are they derived from them; however, by appropriately choosing the constants V1, V2, W1, W2 we may obtain a numerical solution satisfying conditions (7). The results of the calculations are shown in Table 5.

Cylindrical Geometry

The one-velocity kinetic equation and the system of equations for the P_3 approximation are given in [10]. The boundary conditions for these equations have the following form for r = R

$$-(1-\varkappa)(16\Psi_{00} - 10\Psi_{20} + 5\Psi_{22}) + 32(1+\varkappa)\Psi_{11} = 8V^{00};$$

$$5(1-\varkappa)(8\Psi_{00} - 50\Psi_{20} + 5\Psi_{22}) - 128(1+\varkappa)(\Psi_{11} - \Psi_{31}) = 320V^{10};$$

TABLE 6. Deviations of the Disadvantage Factors

Parameters	d_1-d_0 *				d_2-d_1				d_4-d_2	
	$m_{eff}=1$		$m_{eff}=2{,}06$		$m_{eff}=1$		$m_{eff}=2{,}06$		$m_{eff}=1$	
	cells				cells				cells	
	I	II	I	II	I	II	I	II	I	II
From [3]	−0,0683	−0,2685	−0,0331	−0,1296	−0,0970	−0,1675	−0,0581	−0,0939	−0,0110	−0,0172
G_{11}	−0,0684	−0,2685	−0,0331	−0,1296	+0,0049	+0,0083	+0,0009	+0,0013	−0,0001	0,0000
P_3^{pl}	−0,0684	−0,2687	—	—	+0,0040	+0,0088	—	—	—	—
P_3^{cyl}	−0,0414	−0,1643	—	—	+0,0057	+0,0167	—	—	—	—

* d_i – value of d when i terms are left in the expansion of the scattering indicatrix.

$$-30(1-\nu)(4\Psi_{00}-5\Psi_{20})-175\left(1-\frac{5}{21}\cdot\nu\right)\Psi_{22}+64\left(1+\frac{2}{3}\nu\right)(6\Psi_{11}-\Psi_{31})+32\Psi_{33}=160V^{12} \quad (8)$$

and for r = 0, $\Psi_{11} = \Psi_{31} = \Psi_{33} = 0$ [10]. Here $\nu = (\varkappa/2)(3-\tilde{a})$

$$V^{kl}=\frac{4}{\pi}\int_{\pi/2}^{\pi}d\varphi\cos l\varphi\cos\varphi\int_{0}^{\pi/2}VP_{2k}^{l}(\cos\vartheta)\sin^2\vartheta\,d\vartheta.$$

For the cell $\varkappa = 1$. By suitably choosing the parameter $\tilde{a}$ we may make $d\Psi_0/dr|_{r=R}$ vanish.

The algorithm of the program ensures that the following conditions should be satisfied (for the cell):

$$\Psi_1(R)=0;\quad \frac{d\Psi_0}{dr}\Big|_{r=0}=0.$$

We calculated cells which were, in a certain sense, equivalent to the cells of [3], with dimensions given by the conditions

$$V_b/V_{mod}=\text{const};\quad V_b/S_b=\text{const},$$

where V_b and V_{mod} are the volumes of the block and the moderator, S_b is the surface area of the block, the dimensions of cell I are 0, 0.4, 0.85, and the dimensions of cell II are 0, 0.8, 1.7.

The values of Σ, Σ_s, and $g(\mu \to \mu')$ remained the same as in the plane geometry.

The results of our calculations of the equivalent cylindrical cells are presented in Table 6.

CONCLUSIONS

The results of the calculations presented in Table 6 are qualitatively in mutual agreement, and clearly contradict the results of [3]. It follows from our results that there is really no need to take account of the second and higher angular moments of the scattering indicatrix in practical calculations of the thermal –neutron use factor.

LITERATURE CITED

1. H. Honeck, Nucl. Sci. and Engng., 18, 49 (1964).
2. H. Takahashi, Nucl. Sci. and Engng., 24, 23 (1970).
3. G. Eccleston and N. McCormick, J. Nucl. Energy, 24, 23 (1970).
4. N. I. Laletin, Preprint IAE-2138, Moscow (1971).
5. P. Benoist, Nucl. Sci. and Engng., 30, 85 (1967).
6. I. S. Gradshtein and I. M. Ryzhik, Tables of Integrals, Sums, Series, and Products [in Russian], Fizmatgiz, Moscow (1963).
7. N. I. Laletin, Preprint IAE-1374, Moscow (1967).
8. J. Mika, Nucl. Sci. and Engng., 11, 415 (1961).
9. T. Krieger and M. Nelkin, Phys. Rev., 106, 290 (1957).
10. G. I. Marchuk and V. I. Lebedev, Numerical Methods in the Theory of Neutron Transport [in Russian], Atomizdat, Moscow (1971).

GENESIS OF RADIOGENIC LEAD HALOS IN PRECAMBRIAN URANIUM DEPOSITS

A. V. Tarkhanov and V. I. Zhykova

UDC 550.8:553.495

Precambrian uranium deposits [1-5] are exceptionally favorable subjects for investigating the possibilities of using the lead-isotope survey technique. On the one hand, this results from the long lifetime of uranium ores, which ensures the buildup of a large mass of radiogenic lead, and on the other hand, from the complex postformation geological history of the development of the deposit which led in a number of cases to separation of the lead and the undecayed portion of the uranium.

This paper discusses the ratio of lead and uranium in uranium minerals, ores, and surrounding rocks, the type of occurrence for radiogenic lead, the genesis of lead halos, and the possibilities for using isotopic lead ratios in surveying deposits and evaluating anomalies.

The absolute age of a uranium deposit is close to 1800 million years according to data from many investigations including our own (Table 1). As simple calculations show, the lead content in minerals and rocks of this age is given by the expression

$$Pb_r = 0.35U + 0.09Th + Pb_b,$$

where U and Th are respectively the uranium and thorium content in a mineral or rock; Pb_b is the background lead content in rock.

In the overwhelming majority of samples from deposits investigated, the actual lead content did not correspond to the calculated value. Ordinarily, a deficiency of radiogenic lead is noted in uranium minerals and an excess in the surrounding rock. In uranium ores, the ratio of the actual content of lead to the calculated value varies from 22 to 520%.

In one of the deposits studied, uraninite was the main uranium mineral; pitchblende was present in lesser amount. Uraninite, which forms more or less uniform inclusions in ores, is in the form of coarse-zoned skeletal or relict crystals of cubic or octahedral shape. The crystal dimensions are hundredths and thousands of a millimeter. Pitchblende is mainly concentrated in thin carbonate veins forming collomorphic surface crusts or inclusions of individual spherulites. The surrounding rock is characterized by extremely low background content of uranium (>0.0001%), thorium (>0.0001%), and lead (>0.001%).

The thorium content in uranium ores does not exceed a few ten-thousandths of a percent. In that case, the amount of lead in minerals and rocks should be 35% of the uranium present in them. However,

TABLE 1. Isotopic Composition of Lead in Uraninites and Uranium Ores

Sample	Pb^{204}	Pb^{206}	Pb^{207}	Pb^{208}	Pb^{207} */Pb^{206}	Age, 10^6 yr.
Uraninite	0,3	100	11,32	0,85	0,11	1800
Uraninite	0,057	100	11,64	1,74	0,11	1800
Uraninite	0,05	100	11,33	1,40	0,11	1800
Uranium ore	0,02	100	10,95	0,03	0,107	1750

*Correcter for ordinary lead [6].

Translated from Atomnaya Énergiya, Vol. 34, No. 6, pp. 455-459, June, 1973. Original article submitted August 3, 1972.

TABLE 2. Content of Uranium, Lead, and Sulfide Sulfur in Uranium Minerals According to Chemical Analysis, wt. %

Mineral	Uranium	Lead			Sulfide sulfur	Ratio of actual total lead content to calculated value, %
		galena	nongalena	calculated content for age 1800 million years		
Uranite	53,99	3,88	10,56	18,9	0,6	75
Uranite	57,59	not determined	18,65	20,3	not determined	92
Uranite	40,45	4,98	5,03	14,1	0,77	71
Pitchblende	56,63	3,43	13,59	19,8	0,53	86
Pitchblende	65,96	11,64	1,75	23,0	1,80	57

the actual lead content in uraninites and pitchblendes was considerably lower (Table 2), and from an analysis of 27 samples was on the average 73% of the value calculated for an age of 1800 million years. Furthermore, the distribution of the relative content for the samples was the following: one sample contained 45%, one 57%, three 60-70%, eighteen 70-80%, one 92%, and one 103%. On the average, therefore, more than a quarter of the radiogenic lead which built up over 1800 million years through the decay of uranium was removed as the result of some geological process or other.

Characteristics of uranium oxides are increased reflectivity (to 23%), microhardness (to 950 kg/mm^2), elementary cell parameter a_0 (to 5.495 Å), and high lead content (to 10-18%). Chemical, x-ray structure, spectral, thermal, mineralographic, and mineralogic studies made in conjunction with B. M. Eloeb and N. G. Nazarenko established the presence of quartz, carbonate, and galena impurities in uranium oxides. Since no other suflides of any kind were detected in the samples, all the sulfide sulfur was assumed to be associated with galena. However, the actual lead content in the samples was considerably greater than the amount needed for galena formation (see Table 2). The excess lead (nongalena lead) most likely enters the crystal lattice of uranium minerals increasing their physical parameters.

To verify the assumptions made above, pitchblende with a high content of nongalena lead was heated to temperatures of 500-1000°C in air and in a current of hydrogen and to 800°C in a vacuum. Heating in air at 600°C and above facilitated the formation of a cubic phase with the parameter a_0 = 5.60 Å, which is identical to the compound $PbUO_{4-x}$ [7].

According to the data of V. A. Kirkinskii [8], the compound $PbUO_{4-x}$ is not formed through the interaction of uranium oxide with galena lead which indicates the participation of nongalena lead in the formation of this phase in our case. The transitional phase U_3O_8 does not arise during the heating, which also confirms data concerning the occurence of nongalena lead in the samples that hinders transition of the uranium dioxide structure into UO_3 even at elevated temperatures.

Heating in a vacuum at 800°C reduces the lattice parameter from 5.495 Å in the original sample to 5.44 ± 0.01 Å, which can only be explained by the escape of lead from the mineral lattice.

In a current of hydrogen, a fluorite-type structure is maintained up to 1000°C. Furthermore, as the temperature increases to 600-700°C, the lattice parameter gradually decreases from 5.495 to 5.41 Å. Further increases in temperature leads to an increase in the lattice parameter to 5.435 Å at 900-1000°C. Results of chemical analyses show that even at 700°C all the uranium in the sample is in the tetravalent state. Therefore the decrease in the parameter can be explained by the escape of lead from the crystal lattice of pitchblende with this tendency being so great that it overcompensates for the increase in the parameter resulting from uranium reduction and ordering of the crystal structure during heating. The presence of lines for elementary lead in roentgenograms along with the lines from uranium dioxide confirms the correctness of the conclusions.

Galena is constantly noted in uranium minerals. In uraninite, it forms an inclusion of fine cubic crystals (Fig. 1); in pitchblende, it is made up of independent fibrous veins (Fig. 2). Sometimes veins of galena are encountered outside the limits of uraninite or pitchblende accumulations.

The lead content in uranium ores (Table 3), just as in minerals, fails to correspond to calculated values more often than not. On the whole, a deficiency of radiogenic lead is noted in some ore bodies but the lead content in individual samples is several times greater than the calculated value, which is probably associated with significant removal of uranium.

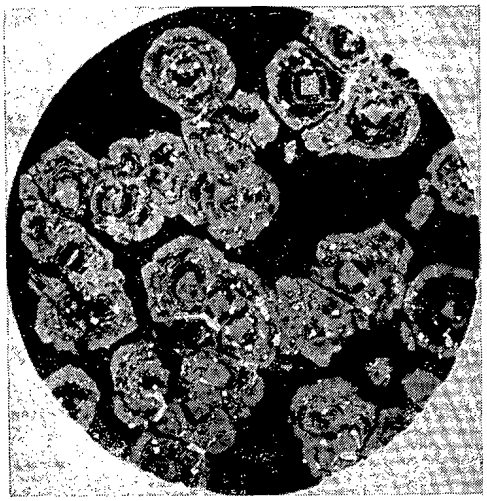

Fig. 1. Galena inclusions (white) in zonal uraninite crystals.

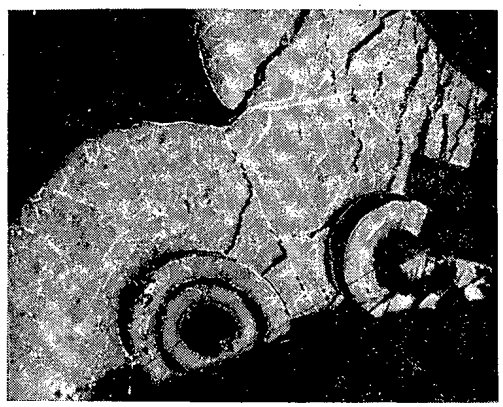

Fig. 2. Galena deposits (white) in pitchblende.

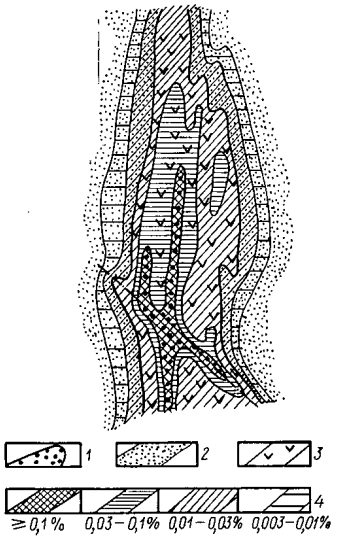

Fig. 3. Diagram of structure of radiogenic lead halo around ore body (section): 1) uranium ore; 2) metamorphic rock; 3) metasomatites; 4) lead content.

In surrounding metasomatically changed rocks, radiogenic lead halos are found which are traced more than 200 m above the ore bodies. Furthermore, the width of the halo is considerably greater than the thickness of the ore body (Fig. 3). Lead distribution in halos is extremely nonuniform. Boundaries of isoconcentration fields are shown in Fig. 3 for predominantly encountered concentrations. In fact, even in a concentration field of 0.1% and above, the lead content in a number of samples does not exceed a few thousandths of a percent. The type of lead occurrence in halos has not been established reliably; however, a portion of it is undoubtedly in the form of galena. Evidence of this is the constant discovery of seams of this mineral (thickness up to 1 cm) in metasomatites bordering on the ore body. Uranium content in halos is considerably below the lead content (Table 4); the latter is ten times greater than the amount of lead which can be accumulated through the decay of uranium over 1800 million years. Nevertheless, from data obtained in isotopic studies, the major portion of the lead is radiogenic both in the total samples and in the galena selected within halo boundaries (Table 5). It is noteworthy that the Pb^{207}/Pb^{206} ratio corrected for ordinary lead corresponding to the metamorphism age of ore (400-600 million years) varies from 0.11 to 0.128.

One can make the following assumptions about the genesis of radiogenic lead halos: 1) the lead was formed in situ through radioactive decay of uranium, the undecayed portion of which was carried outside the boundaries of the halo; 2) the lead halos were formed simultaneously with the uranium ores because of radiogenic lead carried away together with uranium from some ancient uranium-rich stratum; 3) the halos arose because of radiogenic lead carried away from uranium ores after the lapse of a certain time after their formation.

The first assumption is improbable because, judging from the dimensions of a radiogenic lead halo, a very thick and rich ore body should be located in the upper portion of the deposit. However, ore bodies in a deposit of this kind are localized only in metasomatites, and only the very first stages of metasomatic changes in rock (pre-ore formation) are observed within the boundaries of the halos discussed.

Under the second assumption, knowing the age of the deposit and assigning an age to the productive strata, one can calculate [6] the Pb^{207}/Pb^{206} ratio in the radiogenic lead in the halo which is formed around the ore body simultaneously with the deposit. If the age of the productive stratum is 2000 million years, this ratio should be 0.22; if it is 2300 million years, the ratio should be 0.26; and if 2500 million years, 0.29. The clear disagreement of these values with actually observed ratios (see Table 5) demands rejection also of the second explanation for the genesis of radiogenic lead halos. As calculations indicate, the

TABLE 3. Uranium and Lead Content in Uranium Ores, Arbitrary Units

Uranium	Lead		Ratio of actual to calculated lead content, %
	actual content	calculated content for an age of 1800 million years	
240*	60	84	71,5
200†	60	70	86
2500	880	880	100
96	20	34	59
54	12	18	67
600	640	210	320
136	20	48	42
72	16	26	62
108	36	38	95
240	440	84	520
36	4	12	33
560	800	196	410
98	8	34	23,6
294	160	102	157
242	94	146	66
528	40	1840	22
280	600	182	330

*Average over 21 samples from a single ore body.
†Average over 30 samples from an ore deposit.

TABLE. 4. Uranium and Lead Content in Rocks Surrounding Ore Bodies,* wt. %

Uranium	Lead		Ratio of actual to calculated lead content, %
	actual content	calc. content for age of 1800 million years	
0,00060	0,0110	0,00020	5500
0,00036	0,0240	0,00013	18500
0,00018	0,0170	0,00006	28000
0,00054	0,0490	0,00019	26000
0,00018	0,0100	0,00006	17000
0,00063	0,0070	0,00022	3500
0,00018	0,0090	0,00006	15000
0,00360	0,0570	0,00130	4400
0,00180	0,0530	0,00060	8800
0,00350	0,0160	0,00120	1300
0,00270	0,0400	0,00950	4200
0,00090	0,0150	0,00030	5000
0,00030	0,0075	0,00010	7500

*Samples selected within boundaries of lead halo.

TABLE 5. Isotopic Composition of Lead in Galena and Pyrite

Sample	Pb^{204}	Pb^{206}	Pb^{207}	Pb^{208}	Pb^{207*}/Pb^{206}
Pyrite	0,340	100	17,46	—	0,126
Galena†	0,020	100	13,04	0,58	0,128
	0,110	100	13,77	4,20	0,122
	0,100	100	14,19	4,87	0,126
	—	100	12,41	2,20	0,124

*Data of A. I. Tugarinov [6].
†Corrected for ordinary lead 400 million years old.

most characteristic Pb^{207}/Pb^{206} ratios for lead halos (0.122-0.128) can be obtained only by the separation of radiogenic lead 400-600 million years ago from uranium ores with an absolute age of 1800 million years. Evidence in favor of such an assumption is the persistent deficiency of radiogenic lead in uranium minerals and portions of uranium ores. The possibility of radiogenic lead migration from uranium minerals was experimentally confirmed by A. I. Tugarinov [6] and also by the results given above for our experiments on heating of pitchblende.

The process of lead removal from uranium minerals can be associated either with one of the stages of tektonic activity which manifest themselves in the formation of numerous explosive disruptions and the introduction of dikes of basic and ultrabasic rocks or with the formation of Lower Paleozoic erosion crusts. The specific role of each of these processes in the post-ore formation history of uranium deposits and the associated change in the mineral composition of ore and surrounding rock is not clear at the present time and should be the subject of a special study. Whatever the reason for lead migration, it is responsible for the formation of halos of considerable size with increased concentrations of radiogenic lead. The existence of these halos undoubtedly should be used in prospecting for uranium deposits especially since great additional expenditure is not required. On the basis of presently employed techniques for surveying and prospecting for deposits, one can contemplate the following sequence of operations for revealing and evaluating radiogenic lead anomalies.

1. Through data from semiquantitative spectral analysis of all metallometric samples collected from an area under investigation, samples are selected in which the lead content is three or more times greater than the uranium content and at the same time is greater than the background lead content in rocks.

2. The lead content in the selected samples is checked by one of the available quantitative analytic methods, polarography, for example, following which the final number of samples for a study of the isotopic composition of the lead is established.

3. Through data from relatively inexpensive isotopic spectral analysis of gross samples, samples are selected which contain predominantly radiogenic lead and which are also plotted on the appropriate maps and sections using standard symbols to make it possible to determine the intensity and size of radiogenic lead halos.

4. For genetic characterization of halos, the content of uranium, thorium, and lead is determined in certain samples which are selected after consideration of all existing geologic data and a mass-spectrometric analysis is made of the isotopic composition of the lead.

In the interpretation of the resultant data, one should bear in mind that intense and sizeable halos of radiogenic lead may be associated only with relatively large concentrations of uranium; however, not every large uranium deposit must necessarily have a lead halo of considerable size. Moreover, not every halo can be discovered by metallometric sampling because of the exceptionally nonuniform lead content in it. For uranium deposits with an absolute age of 1800 million years, the isotopic composition of radiogenic lead, including corrections for ordinary lead and radiogenic lead formed in situ through decay of uranium, is characterized by the absence or extremely low content of Pb^{208} and a Pb^{207}/Pb^{206} ratio of 0.12-0.13. It should be noted that in the areas investigated there are thorium–uranium ore manifestations the formation of which is associated with potassium metasomatism of granites and pegmatites. The absolute age of the uranium and uranium-containing minerals in these manifestations is about 2000 million years. It is natural to expect that 400-600 million years ago processes also occurred in them which led to the formation of radiogenic lead halos just as in the deposits studied by us. As calculations indicate, the characteristic Pb^{207}/Pb^{206} ratio for lead in such halos should be 0.14-0.15 and the Pb^{208} content should also be increased, which makes it possible to distinguish them with sufficient reliability from halos associated with the more promising deposits 1800 million years old. Therefore, one can consider that Precambrian uranium deposits are very favorable subjects for the application of the isotopic lead technique in surveying for deposits of this kind.

LITERATURE CITED

1. D. Ya. Surazhskii, Methods of Surveying and Exploring for Uranium Deposits [in Russian], Atomizdat, Moscow (1960).
2. R. P. Petrov, V. S. Karpenko, and Yu. A. Meshcherskii, Uranium Deposits in Precambrian Iron Ores [in Russian], Atomizdat, Moscow (1969).
3. V. S. Kazakov, A. V. Kuzmenko, and N. S. Rutkevich, in: Geology and Genesis of Endogenic Uranium Deposits [in Russian], Nauka, Moscow (1968).
4. V. I. Zhukova, in: Uranium Deposits, Zonality, and Paragenesis [in Russian], Atomizdat, Moscow (1970), p. 5.
5. K. N. Chernetsova, ibid., p. 34.
6. A. I. Tugarinov, Geology – Methods of Determining Absolute Age of Rocks [in Russian], Gosgeoltekhizdat, Moscow (1961).
7. C. Frondel and I. Barnes, Acta Cryst., 11, No. 8, 562 (1958).
8. V. A. Kirkinskii, in: Reports on Genetic and Experimental Mineralogy [in Russian], Vol. IV, Nauka, Novosibirsk (1966), p. 30.

DETERMINATION OF STABLE NEON ISOTOPES IN RADIOACTIVE MINERALS AND NATURAL GASES

Yu. A. Shukolyukov, G. Sh. Ashkinadze, and V. B. Sharif-Zade

UDC 621.039.1

Radioactive minerals contain the isotopes Ne^{21} and Ne^{22} which are formed in (α, n), (α, p), and other nuclear reactions [1-4] in amounts from $\approx 10^{-9}$ to $\approx 10^{-6}$ cm^3/g. In their migration, the isotopes Ne^{21} and Ne^{22}, like the radiogenic isotopes of xenon, krypton, argon, and helium [5, 6], leave the crystal structure of the minerals and appear as a constituent of the natural gases. In natural gases, the content of radiogenic Ne^{21} and Ne^{22} varies from 10^{-8} to 10^{-6} volume percent [7, 8].

The determination of microamounts of the stable isotopes Ne^{21} and Ne^{22} in natural objects is of interest in studies of the physicochemical conditions for the existence of radioactive minerals, in studies of natural nuclear processes, and of the genesis of natural helium-containing gases, and in working out certain problems in prospecting for radioactive elements.

Separation of Neon from Minerals and Gases for Isotopic Analysis

The equipment used was constructed with the help of I. N. Tolstikhin. To separate neon, mineral samples were fused in a vacuum furnace by means of a tungsten spiral (Fig. 1a). First, the furnace was baked out at 200-250°C for several hours. In the determination of neon isotopes in gases, the gas container was opened by means of the device sketched in Fig. 1b.

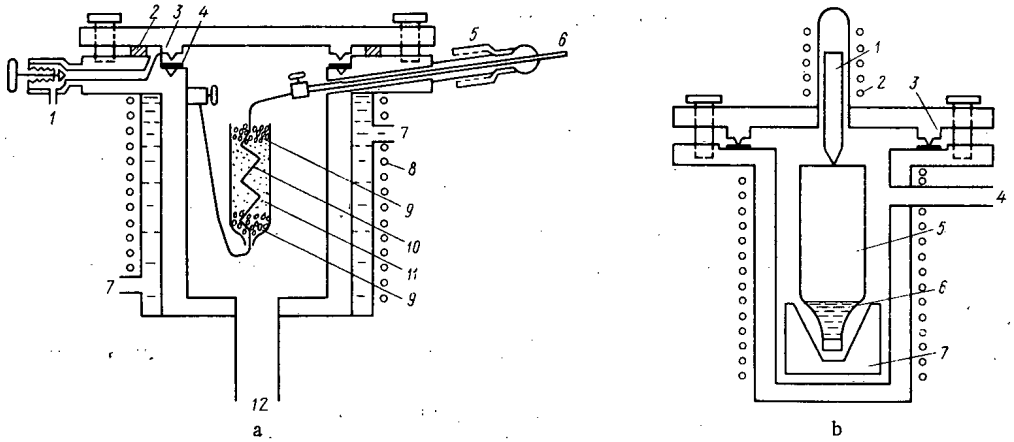

Fig. 1. Apparatus for extraction of gases from samples: a) vacuum furnace: 1) forevacuum line; 2) rubber gasket ring; 3) vacuum gasket; 4) copper gasket; 5) vacuum seal for electrode; 6) molybdenum electrode; 7) water cooling; 8) nichrome heater winding; 9) crushed quartz; 10) tungsten spiral; 11) mineral sample; 12) high-vacuum line: b) container for extraction of neon from samples of natural gases: 1) iron core for smashing glass gas containers; 2) electromagnet winding; 3) knife-edge vacuum seal; 4) vacuum line; 5) glass gas containers; 6) sealing water column; 7) centering jig.

Translated from Atomnaya Énergiya, Vol. 34, No. 6, pp. 461-464, June, 1973. Original article submitted July 31, 1972.

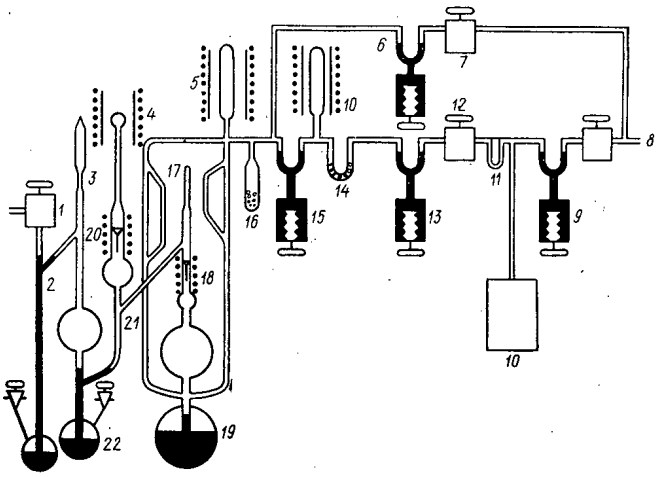

Fig. 2. Diagram of system for neon purification: 1, 7, 8, 12) metal sylphon valves; 2, 21) mercury seals; 3) sealable glass ampul; 4) diffusion cell; 5) metallic calcium getter; 6, 9, 13, 15) mercury seals controlled by sylphon level regulators; 10) vacuum furnace; 11) glass cold trap; 14, 16) tube containing activated charcoal; 17) measuring capillary of compression manometers; 18, 20) electromagnetic valves; 19) mercury compression manometer pump; 22) mercury Toeppler pump.

As a rule, the volume of contaminating gases was 10^7–10^8 times greater than the volume of neon and subsequent operations amounted to separation of the neon from all other gases.

A glass system was used which was first pumped down to a pressure of $(1\text{-}3)\cdot 10^{-7}$ torr by means of a DRN-10 mercury diffusion pump (Fig. 2). In the pumping lines, Du-6 metal sylphon valves were used. Parts of the system where gases remained a comparatively long time during the course of an experiment were provided with U-shaped mercury seals controlled by metal sylphons.

After the completion of fusion with mercury seals closed, water vapor and carbon dioxide was frozen out in a trap cooled to −196°C. Then the temperature of a titanium getter was raised to 1000°C, the main portion of the chemically active gases was absorbed, and the gases were transferred into a manometer-pump with electromagnetic valve [10] by opening the seals controlled by a sylphon level regulator. Furthermore, the heavy noble gases (argon, krypton, and xenon) were adsorbed on activated charcoal held in a glass tube at −196°C. Having shut the seals, the gases were released from the manometer pump for final purification in a calcium absorber. For this purpose, it was heated to 650°C and then the temperature was reduced to 300°C. As a result, a mixture of two gases remained: helium and neon in a ratio of approximately $10^6 : 1$.

By means of the manometer pump, mercury seal, and electromagnetic valve, the helium–neon mixture was transferred into a diffusion cell which was a quartz bulb 2 cm in diameter having a wall 50 μ thick. For a temperature T, wall thickness l, and pressure p, an amount of gas diffuses through S cm^2 of a quartz wall per unit time which is given by the following expression:

$$\frac{dQ}{dt} = \mathrm{K}(T)\cdot PlS.$$

The coefficient K(T) depends on the kind of gas for a given temperature; the permeability of quartz for helium is considerably greater than the permeability for neon.

A temperature of 1000°C was chosen as the working temperature. The main portion of the helium migrated through the wall of the diffusion cell in 4-6 h. The amount remaining was usually no more than $(2\text{-}3)\cdot 10^{-4}$ cm^3. During the period when the diffusion cell was in operation, the neon loss did not exceed 3-5% (Fig. 3). After removal of the main portion of the helium, the remaining gas was transferred by a Toeppler pump into a sealable glass ampul with a closed mercury seal.

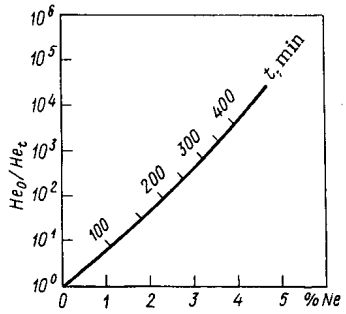

Fig. 3. Difference in diffusion rates through a quartz membrane for helium and neon: He_0 is the original amount of helium in diffusion cell; He_t is the amount of helium at the time t; % Ne is the neon fraction which diffuses out of the cell up to the time t.

Isotopic Analysis of Neon

The total amount of neon, including instrumental background, was $\sim 10^{-6}$ cm^3. The background was atmospheric neon (Ne^{20}, 90.50%; Ne^{21}, 0.269%; Ne^{22}, 9.23%) [8], which was present in the system because of incomplete vacuum conditions resulting from desorption from internal surfaces of the system and from the surface of the sample. To measure such an amount of neon, a standard MV2302 mass spectrometer (accelerating voltage, 3 kV; resolution, 4000-5000; electron multiplier at output; nonuniform 180° magnetic field) was modified [10].

The measurements were made in a quasistatic vacuum mode in which the high-vacuum valves were shut. Gases escaping from internal surfaces were absorbed by a titanium getter pump connected to the analyzer chamber.

The amount of ion current from $(Ne^{20})^+$ was distorted by the presence of a line from the ion $(Ar^{40})^{++}$ in the mass spectrometer. To eliminate this effect, and the effect of the superposition of the $(CO_2)^{++}$ line on the $(Ne^{22})^+$ line as well, the ionizing voltage was kept below 38 V. To reduce the effect of the $(Ne^{20}H^1)^+$ ion on measurements of $(Ne^{21})^+$, the titanium getter was thoroughly outgassed before each experiment until there was significant reduction in the hydrogen background. As special experiments demonstrated, the ions $(H_2^1O^{18})^+$, $(D_2^2O^{17})^+$, $(D_2^2O^{18})^+$, etc. played no important role since water vapor was efficiently frozen out in the cold trap of the feed system and was decomposed in the titanium getter in the analyzer chamber. There were no noticeable lines in the spectrum of organic radicals unresolved from neon lines.

Because of discrimination effects, the measured isotopic composition of atmospheric neon usually differed by 1-3% from the isotopic composition determined with mass spectrometers previously calibrated by means of mixtures of separated neon isotopes [7, 11]. The appropriate correction was made to the neon results obtained from the samples studied.

The total amount of neon in the samples was determined by the peak-height method. For this purpose, a definite amount of a neon standard was admitted into the analyzer chamber and the dependence of the output signal from the mass spectrometer on the amount of standard determined. Using this dependence, one could determine the total volume of neon in a sample from the magnitude of the signal.

To admit neon into the analyzer chamber and to select a given volume of a neon standard, a special feed system was used (Fig. 4). The neon sample under investigation, which was in a glass ampul, was placed in a sylphon ampul-crusher. After obtaining a vacuum of $\sim 10^{-7}$ torr, the ampul was crushed and the neon discharged through a sylphon valve into the analyzer chamber, the high-vacuum valves of which had been closed in advance. After the measurements, the neon was pumped out of the chamber through the high-vacuum valves.

The required amount of neon standard was withdrawn from a glass bulb into a measuring capillary by means of valves and a mercury seal. The volume of gas in the capillary was measured by the compression method. The ratio between the volumes of the sphere of the compression manometer and the capillary tube ($V_{sph}/V_c = 500$) was determined in advance. Therefore, knowing the original volume of gas in the measuring capillary and distributing it between the sphere of the manometer and the capillary tube, one can calculate the volume of gas reaching the capillary tube. In this way, the required volume of neon (from 10^{-9} to 10^{-6} cm^3) was measured out. The accuracy in determining microamounts of neon by this method was ±10-15%.

The quantity of the radiogenic isotopes Ne^{21} and Ne^{22} in radioactive minerals or natural gases was calculated from the expressions

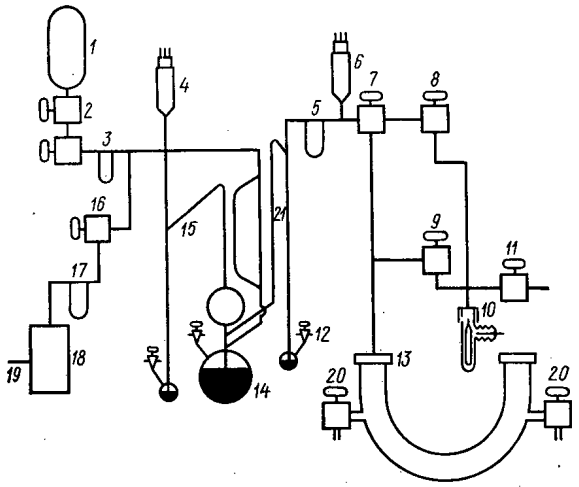

Fig. 4. Diagram of mass-spectrometer feed system for measurement of microamounts of neon: 1) bulb containing neon standard; 2) metal valves for withdrawing neon standard; 3, 5, 17) cold traps; 4, 6) manometer tubes; 7, 8, 9, 11, 16) metal sylphon valves; 10) sylphon ampul-crusher; 12) mercury seal; 13) mass-spectrometer chamber; 14) compression mercury manometer pump; 15) measuring capillary; 18) mercury diffusion pump; 19) forevacuum line; 20) high-vacuum sylphon valves; 21) capillary tube for sampling neon.

$$Ne^{21}_{rad} = N^{21}_{meas} - \left(\frac{Ne^{21}}{Ne^{20}}\right)_{atm} \cdot Ne^{20}_{meas}$$

$$Ne^{22}_{rad} = Ne^{22}_{meas} - \left(\frac{Ne^{20}}{Ne^{22}}\right)_{atm} \cdot Ne^{20}_{meas}$$

By means of the method described, neon isotopes were determined in pitchblende, smarskite, betafite, monazite, britholite, and lovchorrite, in natural gases from regions where there are uranium deposits and from shot holes in salt strata, etc. [3, 4, 8].

The authors thank É. K. Gerling for discussions of the work and A. B. Verkhovskii for help in performing the experiments.

LITERATURE CITED

1. G. Wetherill, Phys. Rev., 96, No. 3, 679 (1954).
2. D. Bogard et al., J. Geophys. Res., 70, No. 3, 307 (1965).
3. V. B. Sharif-Zade et al., Geokhimiya, No. 3, 314 (1972).
4. Yu. A. Shukolyukov et al., At. Energ., 31, 530 (1971).
5. Yu. A. Shukolyukov and G. Sh. Ashkinadze, Geokhimiya, No. 10, 1083 (1967).
6. I. M. Morozova and G. Sh. Ashkinadze, Mingration of Noble Gas Atoms in Minerals [in Russian], Nauka, Leningrad (1971).
7. D. Emerson et al., Internat. J. of Mass Spectrometry and Ion Phys., 1, No. 1, 105 (1968).
8. Yu. A. Shukolyukov and V. B. Sharif-Zade, and G. Sh. Ashkinadze, Geokhimiya, No. 3, 568 (1973).
9. I. N. Tolstikhin, Author's Abstract of Candidate's Dissertation, Leningrad (1966).
10. Yu. A. Shukolyukov, Fission of Uranium Nuclei in Nature [in Russian], Atomizdat, Moscow (1971).
11. J. Walton and A. Cameron, Z. Naturforsch., 21a, No. 1/2, 115 (1966).

LOSSLESS PARTICLE CAPTURE IN RF-ACCELERATION MODE IN PROTON SYNCHROTRON

É. A. Myaé and P. T. Pashkov

UDC 621.384:634.5

The feasibility of practically 100% particle capture in the resonance-acceleration mode was established a relatively long time ago (so-called adiabatic capture [1-3]). Here, one assumes that the time for establishing the accelerating potential is significantly greater than the particles' phase-oscillation period. Realizing such capture in a proton synchrotron is impeded due to the unattainably high value of the beam turning toward the accelerator inner chamber wall [2], since the particle energy increases at an insufficient rate to compensate the growing magnetic field. It is shown in [4] that a capture efficiency close to 100% can be attained also when the accelerating-potential amplitude grows even more rapidly, if the ratio frequency is modulated such that the particles on the average are not accelerated. However, this paper does not discuss questions related to the transition from the capture mode to the acceleration mode.

The present article examines the fundamental properties of synchrotron capture and the transition to the acceleration mode at constant radius. Here, the accelerating-potential amplitude rises in a time comparable to the synchrotron-oscillation period, while the magnetic field varies with time. The high frequency is programmed such that there is no increase in synchronous-particle energy upon capture, and the separatrix area is constant in the transition region to steady-state acceleration. As a result, the equilibrium beam radius changes, but this variation need not exceed the allowable limits.

Characteristics of the Capture Process

The equation for phase oscillations with a time-dependent accelerating potential V = V(t) can be written in the form

$$\frac{d}{dt}\Delta p = \frac{eV(t)}{2\pi mcR_0}\cos\varphi - \frac{dp}{dt};$$
$$\frac{d\varphi}{dt} = \frac{qc}{R_0}\frac{\alpha\gamma^2-1}{\gamma^3}\Delta p, \tag{1}$$

where γ is the synchronous particle's energy in potential-energy units; φ is the particle phase compared to the rf field; R_0 is the mean accelerator radius; α is the orbit expansion coefficient; m is the particle rest mass; c is the speed of light; p is the synchronous momentum in mc units; Δp is the deviation of the particle momentum from the synchronous value; q is the degree of acceleration.

We assume in Eq. (1) that the effect of betatron emf on the acceleration process is insignificant, and the beam turning in the capture process is small compared to the mean accelerator radius. We introduce

$$\tau = t\Omega_0, \tag{2}$$

where Ω_0 is the frequency of small synchrotron oscillations at the time capture ends (when $t = t_0$ and $V(t_0) = V_0$):

$$\Omega_0^2 = \frac{qeV_0|1-\alpha\gamma_0^2|}{2\pi m\gamma_0^3 R_0^2}. \tag{3}$$

Transforming Eq. (1), we have

$$y' = f(\tau)\cos\varphi - \varkappa p';$$
$$\varphi' = \frac{\alpha(p^2+1)-1}{|\alpha(p_0^2+1)-1|}\left(\frac{p_0^2+1}{p^2+1}\right)^{3/2} y; \tag{4}$$

Translated from Atomnaya Énergiya, Vol. 34, No. 6, pp. 465-469, June, 1973. Original article submitted August 9, 1972.

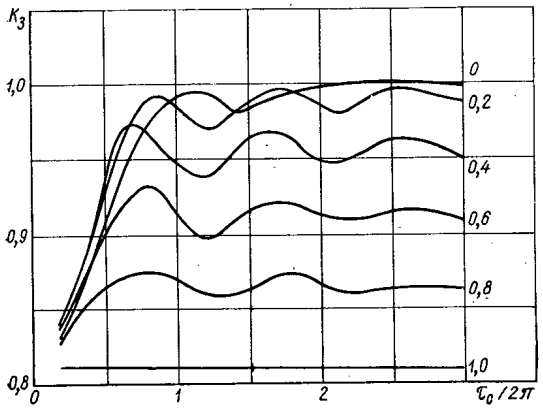

Fig. 1. Dependence of the capture efficiency on the growth rate of the accelerating-potential amplitude.

here $p_0 - p$ at the time of injection (the prime indicates differentiation with respect to τ; $f(\tau) = V(\tau)/V_0$),

$$y = \varkappa \Delta p, \tag{5}$$

where

$$\varkappa = \sqrt{2\pi q \frac{mc^2 |1-\alpha\gamma_0^2|}{eV_0\gamma_0^3}}. \tag{6}$$

We find the energy increase for a synchronous particle:

$$\frac{d\gamma}{dt} = \frac{\gamma(\gamma^2-1)}{\alpha\gamma^2-1}\left(\frac{\alpha}{H}\cdot\frac{dH}{dt} - \frac{1}{\omega_0}\cdot\frac{d\omega_0}{dt}\right), \tag{7}$$

where H is the accelerator magnetic field and ω_0 is the radio frequency. It has been shown [4] that to achieve ~100% capture it is necessary for the momentum of the synchronous particle to remain constant ($p = p_0$) when $0 \le t \le t_0$; therefore, the radio frequency must vary according to

$$\frac{1}{\omega_0}\cdot\frac{d\omega_0}{dt} = \frac{\alpha}{H}\cdot\frac{dH}{dt}. \tag{8}$$

In this case, the phase equation is simplified, and Eq. (4) can be written

$$\varphi'' = \pm f(\tau)\cos\varphi, \tag{9}$$

where the plus and minus signs refer, respectively, to the supercritical and subcritical zones.

At the time of injection, the bunch in the phase plane appears as a rectangle with area $4\pi y_0$. The area of the separatrix S_0 at the end of capture ($\tau = \tau_0$) must be greater than or equal to the area of this rectangle ($\lambda = 4\pi y_0/S_0 \le 1$); otherwise the capture coefficient is always less than 100%. Since

$$S_0 = 4\sqrt{2}\int_{-\pi/2}^{\pi/2}\sqrt{1+\sin\varphi}\,d\varphi = 16, \tag{10}$$

we obtain

$$y_0 \leqslant \frac{4}{\pi}. \tag{11}$$

Using Eqs. (5), (6), and (11), we may find the required accelerating potential amplitude at the end of capture as a function of the beam spread from the injection momenta $(\Delta p/p)_i$:

$$\frac{eV_0}{mc^2} \geqslant \left(\frac{\pi}{2}\right)^3 \frac{q(\gamma_0^2-1)|1-\alpha\gamma_0^2|}{\gamma_0^3}\left(\frac{\Delta p}{p}\right)_i^2. \tag{12}$$

The condition given by Eq. (12) is not sufficient for lossless capture. We must still find out what is the greatest allowable growth rate for the accelerating-potential amplitude for which there are no particle losses when Eq. (12) is satisfied. For this purpose, Eq. (9) was integrated numerically on a computer. The calculations were made in the following manner. The rectangle in the phase plane ($|y| \le y_0$, $-(3\pi/2) \le \varphi \le \pi/2$), which represents the bunch after injection into the subcritical zone (the results hold for the supercritical zone if we replace φ by $-\varphi$), was broken down into ~1000 similar rectangles. The centers of these "macroparticles" were taken as initial conditions for solving Eq. (9). The accuracy for determining the capture coefficient in this way is ~0.5%. The accelerating-potential amplitude varied linearly from the initial value V_i to V_0.

Figure 1 shows values of the capture coefficient as a function of the accelerating-potential amplitude growth rate. The quantity $\tau_0/2\pi$ is plotted on the x axis; the parameter used is the ratio of the initial potential to the potential at the end of capture. The curves correspond to the case $\lambda = 0.9$, when the separatrix area is 10% greater than the area occupied by the beam. It is clear that the capture coefficient undergoes small oscillations, which are caused by the fact that the particle phase motion in the given region is not adiabatic and the bunch boundary has a shape different from that of the phase trajectories. Figure 2 shows the evolution of a bunch on a phase plane during capture with initial potential equal to zero.

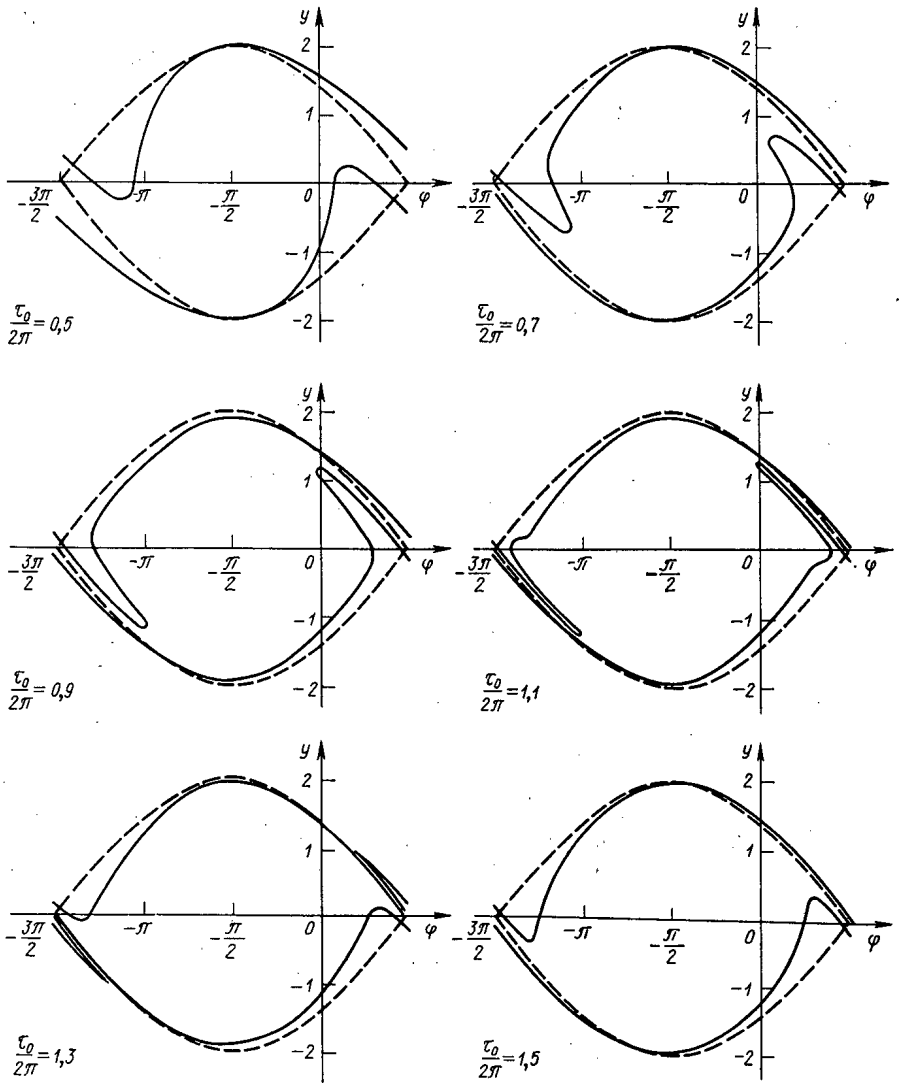

Fig. 2. Position of bunch relative to separatrix in phase plane.

When $\tau_0/2\pi \approx 1.4$, part of the bunch leaves the bounds of the separatrix (when $\tau_0/2\pi = 1.3$ in Fig. 2), but later the particles return again to the separatrix.

Figure 3 shows the capture coefficient at the time $t = t_0$ for three values of λ ($V_i = 0$). It is clear that as λ decreases the capture-coefficient oscillations also decrease, and when $\lambda = 0.8$, they are absent. The first maximum when $\lambda = 0.9$ is close to unity; therefore, we later investigated this case.

Transition to Acceleration Mode

In order to eliminate particle losses from the transition region, the separatrix area S must, at least, not decrease with time. Using the equation for the separatrix area

$$S = 16F(\cos\varphi_S)\sqrt{\frac{eV\gamma^3}{\pi q m c^2 |1-\alpha\gamma^2|}}, \tag{13}$$

where

$$F(\cos\varphi_S) = \frac{\oint \sqrt{\sin\varphi + \sin\varphi_S - (\varphi+\varphi_S)\cos\varphi_S}\, d\varphi}{\oint \sqrt{1+\sin\varphi}\, d\varphi} \tag{14}$$

depends on the synchronous phase, and assuming that S = const when $\tau_0 \le \tau \le \tau_1$ (in this case, the beam momentum spread at the end of the transition region is minimal), and also taking into account the fact that for $t = t_0$, $F(\cos\varphi_S) = F(0) = 1$, we obtain

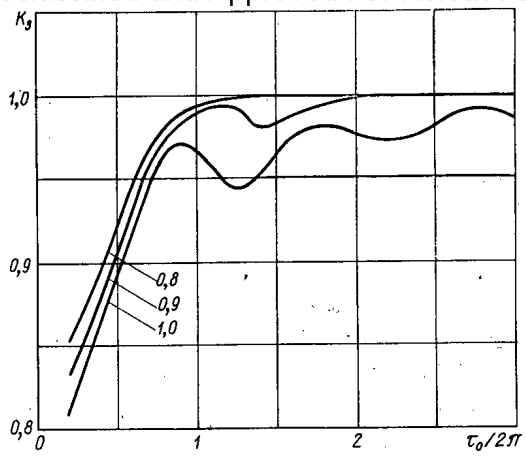

Fig. 3. Capture coefficient at time $t = t_0$ for various λ.

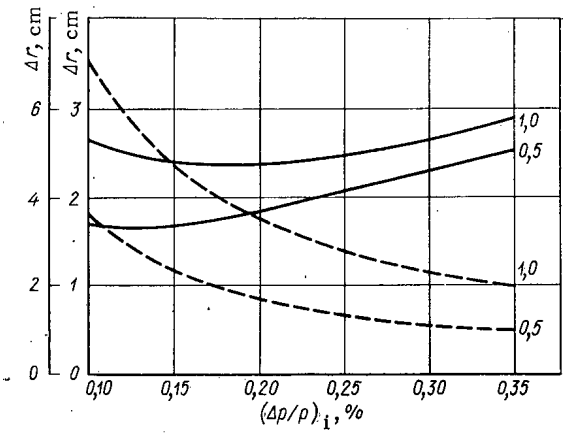

Fig. 4. Radial aperture of IHEP accelerator vacuum chamber needed for lossless capture.

$$1 = F(\cos\varphi_S)\sqrt{f(\tau)\frac{1-\alpha(p_0^2+1)}{1-\alpha(p^2+1)}\left(\frac{p^2+1}{p_0^2+1}\right)^{3/2}}. \tag{15}$$

Determining $\cos\varphi_S$ from Eq. (15) and using the expression for the synchronous phase

$$\cos\varphi_S = \frac{2\pi mcR_0}{eV}\frac{dp}{dt}, \tag{16}$$

we write an equation for the variation of a synchronous momentum with growth τ in the form

$$p' = \frac{1}{\varkappa} f(\tau)\,\Phi(x);$$
$$x = \sqrt{\frac{1}{f(\tau)}\frac{1-\alpha(p^2+1)}{1-\alpha(p_0^2+1)}\left(\frac{p_0^2+1}{p^2+1}\right)^{3/2}}, \tag{17}$$

where Φ is the inverse function of F in Eq. (14). In order for the acceleration mode at constant radius to begin when $t = t_1$, f must at this time satisfy the boundary condition

$$f_1 = \frac{2\pi RR_0}{cV_0\Phi(x_1)}\left(\frac{dH}{dt}\right)_{t_1}, \tag{18}$$

where x_1 is the value of x at time t_1 and R is the orbit radius in the magnet. Equation (17), taking the conditions in Eq. (18) into account, can be solved by successive approximations.

When the dependence H(t) is known, we may realize the required dependence p(t) by modulating the frequency of the accelerating potential in accordance with Eq. (7). In general, the integration of this equation requires numerical calculations. If we assume that during injection $\alpha\gamma^2 \ll 1$, which holds for all proton synchrotrons in existence, then it follows from Eq. (7) that

$$\omega_0(t) = \omega_0\,\frac{\beta(t)}{\beta}\left[\frac{H(t)}{H}\right]^{\alpha}, \tag{19}$$

where ω_{0i}, H_i, and β_i are, respectively, the frequency, accelerator field, and synchronous particle speed at the time of injection.

The radio-frequency program chosen in this way can still not ensure lossless capture, since it may happen that either the phase-motion parameters vary too rapidly (nonadiabatically), or the radial beam turning exceeds the allowable limits. The largest radial translation of a synchronous particle at time t is determined from

$$\Delta R = \psi_m R_0\left(\frac{\Delta p_\tau}{p_0} - \frac{\Delta H_\tau}{H}\right), \tag{20}$$

where Δp_τ and ΔH_τ are the changes in the synchronous momentum and magnetic field from the time of injection; ψ_m is the maximum value of the function which characterizes the nonequilibrium orbit. After determining the maximum beam turning and the separatrix dimension along the radius, we can find the portion of the radial vacuum-chamber aperture necessary for capture. For a given value of dH/dt, the desired

aperture depends on the beam-momentum spread during injection and, in specific cases, requires numerical calculation. To verify capture, Eqs. (4) and (17) must be integrated concurrently in the interval $\tau_0 \leq \tau \leq \tau_1$. The position of particles on the phase plane when $\tau = \tau_0$ is determined from the solution of Eq. (9).

As an example, we will study the capture of particles in the accelerator of the Institute of High-Energy Physics when $V_i/V_0 = 0.2$. Equations (4) and (16) were integrated from $\tau_0/2\pi = 0.8$ (first maximum of the capture curve, Fig. 1) to $\tau = \tau_1$ with an interval of $\Delta\tau/2\pi = 0.2$. Independent of the beam-momentum spread during injection, total capture takes place when $\tau_1/\pi \geq 2$. The values of f_1 and the capture coefficient at the time t_1 are weakly dependent on the form of the function $f = f(\tau)$ in the transition region; therefore, we can limit our attention to linear growth of $f(\tau)$. About 1000 particles were integrated. Figure 4 shows the results of the calculations. The solid lines show the region of the chamber occupied by beam synchrotron oscillations during the capture process Δr (the minimum values of t_1 with 100% capture are taken). The magnitude of the beam turning around the radius Δr_1 from time $t = 0$ to $t = t_1$ is given by the dashed curves. The value of dH/dt is given as a parameter. It follows from Fig. 4 that when the injected-beam momentum spread is ±0.25% for 100% capture, the radial aperture of the vacuum chamber which is free from betatron oscillations and radial distortion of the closed orbit must be ~4 cm for $dH/dt = 0.5$ kOe/sec and ~5 cm for $dH/dt = 1$ kOe/sec.

Allowances for Magnetic-Field and RF-Field Parameters

We will examine the effect on particle capture of deviations in the magnetic field and radio frequency, and also of their rates of variation from the ideal values, when Eq. (8) for $0 \leq \tau \leq \tau_0$ is not satisfied and the synchronous-particle energy varies. Taking Eq. (7) into account, we obtain:

$$\Delta p' \leqslant \frac{\alpha\gamma^2 p\dot{H}}{H\Omega_0 |1-\alpha\gamma^2|}\left(\frac{\Delta\dot{H}}{\dot{H}}+\frac{\Delta H}{H}+\frac{\Delta\dot{\omega}_0}{\dot{\omega}_0}+\frac{\Delta\omega_0}{\omega_0}\right). \tag{21}$$

Results of numerical calculations show that when $\Delta p' \leq 5 \cdot 10^{-6}$, the capture efficiency remains greater than 99%. The coefficient before the round brackets in Eq. (21) is approximately $5 \cdot 10^{-5}$ for the IHEP accelerator, i.e., the sum of all errors should not exceed 10%.

We will find the allowable magnetic-field drifts in the orbit $(\Delta H/H)_i$ and the radio frequencies $(\Delta\omega_0/\omega_0)_i$ equivalent to increasing λ (see, for example, [1, 4]), from the calculated values during injection:

$$\left(\frac{\Delta H}{H}\right)_i \leqslant \frac{|\alpha\gamma^2-1|}{\alpha\gamma^2}\left(\frac{\Delta p}{p}\right)_{\text{allowed}};$$
$$\left(\frac{\Delta\omega_0}{\omega_0}\right)_i \leqslant \frac{|\alpha\gamma^2-1|}{\gamma^2}\left(\frac{\Delta p}{p}\right)_{\text{allowed}}; \tag{22}$$

where $(\Delta p/p)_{\text{allowed}}$ is the permissible relative deviation of the synchronous momentum from the calculated value. If we take $(\Delta p/p)_{\text{allowed}} = 1.2 \cdot 10^{-4}$, which corresponds to changing the synchronous radius by about 0.5 mm, we obtain

$$\left(\frac{\Delta H}{H}\right)_i \leqslant 10^{-2}, \quad \left(\frac{\Delta\omega_0}{\omega_0}\right)_i \leqslant 10^{-4}.$$

Thus, the allowances for $\Delta H/H$ and $\Delta\omega_0/\omega_0$ are stricter than the possible allowances for these quantities calculated according to Eq. (21). We can assume that the increase in synchronous-particle energy from the theoretical law occurs due to deviation in the rates of magnetic-field and rf increase from the ideal values. In such a case, we have

$$\frac{\Delta\dot{H}}{\dot{H}} \leqslant 5 \cdot 10^{-2}; \quad \frac{\Delta\dot{\omega}_0}{\dot{\omega}_0} \leqslant 5 \cdot 10^{-2}.$$

From Eq. (12) we obtain the requirements on the amplitude of the rf potential V_0:

$$\frac{\Delta V_0}{V_0} \leqslant \frac{2\left(\frac{\Delta p}{p}\right)_{\text{allowed}}}{\left(\frac{\Delta p}{p}\right)_i} \tag{23}$$

Taking $(\Delta p/p)_i = \pm 0.25\%$, we find $\Delta V_0/V_0 \leq 0.1$.

In conclusion, the authors thank V. I. Balbekov for useful discussions and help in the work, L. A. Polyakova for computer calculations, and V. P. Sidorova for designing the illustrative material.

LITERATURE CITED

1. A. A. Kolomenskii and A. N. Lebedev, Theory of Cyclic Accelerators [in Russian], Fizmatgiz, Moscow (1962), Chap. 4.
2. J. Kaiser, Proc. Phys. Soc., 63A, 52 (1950).
3. I. S. Danilkin and V. E. Pisarev, At. Energ., 4, 503 (1958).
4. J. Peterson and P. Morton, UCID-10181, AS/Injection/06 (1966).

THE REP-5 HEAVY-CURRENT RELATIVISTIC-ELECTRON PULSE ACCELERATOR, WITH A BEAM CURRENT OF ABOUT 50 kA

G. R. Zablotskaya, B. A. Ivanov,
S. A. Kolyubakin, A. S. Perlin,
V. A. Rodichkin, and V. B. Shapiro

UDC 621.384.653:621.384.637

Interest has recently arisen in extremely powerful beams of relativistic electrons in view of the prospects of using these in controlled thermonuclear fusion reactions, the acceleration of heavy ions, and so forth [1-3]. Beams of this kind are obtained if electrons are directly accelerated by charge pulses lasting a few tens of nanoseconds, generated by pulse-shaping lines with distributed circuit parameters.

The REP-5 accelerator is based on the EG-5 electrostatic generator, and is intended to produce a heavy-current beam of relativistic electrons at an energy of some 2-3 MeV. The basic arrangement of the REP-5 is similar to that of the accelerator described in [4].

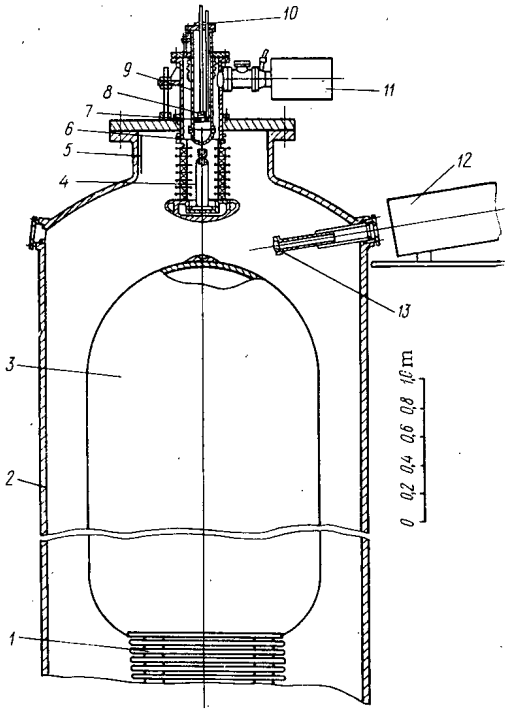

Fig. 1. Sketch of the accelerator: 1) charge generator; 2) high-pressure tank; 3) high-voltage electrode; 4) accelerator tube; 5) capacitive sensor; 6) anode foil; 7) Rogowski belt; 8) calorimeter; 9) drift chamber; 10) shunt; 11) titanium pump; 12) system of laser ignition; 13) lens.

In this paper we shall set out some results obtained during the first stages in the use of the installation, with a charge voltage of $U_c \approx 3$ MeV. The source of the charge voltage is a van de Graaf generator in a high-pressure tank 2.2 m in diameter (Fig. 1). A high-voltage electrode 1.6 m in diameter together with the accelerator tank forms a coaxial shaping line some 3 m long with a wave impedance of about 20 Ω. The line may be charged to a voltage of about 4 MeV, the stored energy then being about 4 kJ. Electrical insulation is provided by a gas mixture (25% CO_2 + 75% N_2) under a pressure of up to 16 atm. The accelerator tube is separated from the electrode by a gas space of ~ 30 Ω. Switching of the high voltage is effected by means of a modulated-Q laser, the output radiation of which comprises four or five pulses each 25 nsec long with a total energy of 2.5 J. At first the laser beam was directed across the lines of force of the electric field of the discharge gap at an angle of 20° to the surface normal (Fig. 1) and focussed on the end of the electrode by means of a lens with a focal length of 500 mm. In the next series of experiments the laser beam was directed along the accelerator axis, which reduced the trip time of the discharge gap to about 400 nsec. The ignition system ensures reliable switching of the voltage (U_b = 1.3-1.5, where U_b is the breakdown voltage of the gas gap in MV).

Two forms of accelerator-tube insulator construction were developed for the accelerator: 1) from cylindrical porcelain rings, and 2) from epoxy resin rings, with a

Translated from Atomnaya Énergiya, Vol. 34, No. 6, pp. 471-474, June, 1973. Original article submitted July 27, 1972.

Fig. 2

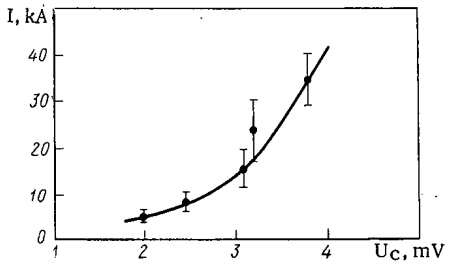

Fig. 3

Fig. 2. Oscillograms of current pulses in the drift chamber for $U_c \approx 3.18$ MV (1) and gun voltage for $U_c \approx 3$ MV (2).

Fig. 3. Amplitude of the electron current as a function of the charge voltage of the generator.

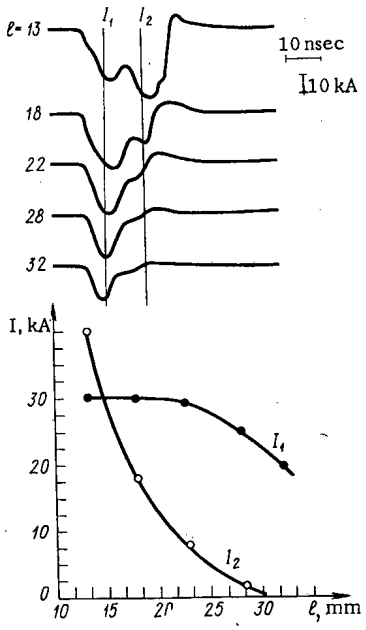

Fig. 4. Dependence of the shape and amplitude of the current pulse on the length of the accelerating gap ($U_c \approx 3.2$ MV; $p \approx 0.04$ mm Hg).

chamfer angle of the inner surface of the dielectric equal to 45°. When studying the configuration of the electric field in the tube an electrolytic tank was employed. The nonuniformity of the voltage distribution along the surface of the tube was about 40%. For the same length of insulator, the working voltage for a porcelain tube with cylindrical rings may be taken as about 1 MV, and for an epoxy resin tube with a chamfer of the dielectric about 3 MV. In a series of experiments, the porcelain tube withstood over 1000 pulses with an amplitude of more than 1 MV without damage.

The stainless steel cathodes have a cylindrical shape, with a sharp edge. The anode is a titanium or aluminum foil 50 μ thick (Fig. 1). The cathode–anode gap may be varied between 1 and 5 cm without breaking the vacuum. The beam passes through the anode foil into a metal drift chamber containing the diagnostic apparatus. The working pressure in the accelerating tube is held at 10^{-5}-10^{-6} mm Hg by means of a NORD-250 titanium pump. In the drift chamber the pressure varies from 10^{-3} mm Hg to atmospheric.

The energy stored in the beam is measured by means of a calorimeter with two thermocouples. A graphite disc 60 mm in diameter is fixed to a mobile metal rod so as to enable the calorimeter to move smoothly over the whole length of the chamber without breaking the vacuum. The beam current was determined with a low-inductance shunt connected between the calorimeter rod and the flange of the drift chamber. For measuring currents of ~10 kA a shunt comprising twenty parallel ULI-0.5 resistances of 2 Ω each was employed. For measuring currents of ~50 kA the resistance of the shunt was reduced to 20 mΩ. The time constant was about 10^{-9} sec.

For determining the current a Rogowski belt similar to that described in [5] was also employed. The belt was fixed to an independent moving rod. The shape of the current pulse was regulated by an auxiliary magnetic loop. The shape of the pulse of accelerating voltage was recorded with a capacitive sensor made of aluminum foil 20 × 80 cm in size, glued to the wall of the tank with insulating adhesive. The pulse signals were passed to an I2-7 oscillograph and photographed on aerial photographic film with a sensitivity of 2000 All-Union State Standard units. For a charge voltage of ~3 MV an electron beam with a current amplitude of about 50 kA and a pulse length of about 20 nsec was obtained.

Figure 2 shows the oscillograms of the current pulses in the drift chamber and the voltage on the gun. Figure 3 shows how the amplitude of the electron current depends on the charge voltage for an anode–cathode distance of 18 mm and a pressure in the chamber of about $3 \cdot 10^{-2}$ mm Hg, for which the defocusing of the beam is still appreciable. Thus the shunt only recorded that part of the current which fell on a calorimeter situated at 8 cm from the anode foil. The scattering of electrons in the anode foil also leads to a loss of some 30% of the particles injected into the drift chamber [6].

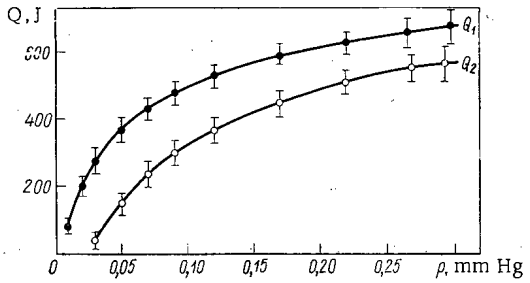

Fig. 5

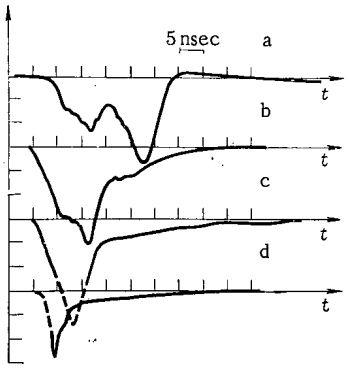

Fig. 6

Fig. 5. Relationship between the beam energy recorded with the calorimeter and the pressure in the drift chamber.

Fig. 6. Dependence of the shape of the current pulse on the pressure in the drift chamber: a) 0.045; b) 0.1; c) 0.16; d) 0.35 mm Hg.

According to the theory of Braginskii [7], the resistance of the spark channel in the liner-tube gap is a function of the current I and the pulse length τ. Estimates show that the voltage drop in the spark may amount to 30-50% of U_c. However, since the readings of the capacitive sensor in the experiments were only of a qualitative nature, the amplitude of the gun voltage pulse was not determined particularly accurately.

Figure 4 shows the way in which the shape and amplitude of the current pulse depend on the anode–cathode gap. The existence of a second peak at l = 13 mm and the shape dependence of its amplitude I_2 on the length l are apparently associated with the propagation of a cloud of plasma formed by explosion emission at the cathode in the accelerating gap [8]. When the plasma surface moves at a mean velocity of $\sim 5 \cdot 10^7$ cm/sec for 10 nsec the accelerating gap may contract by 5 mm, leading to the appearance of the second emission peak. The comparatively slight dependence of I_1 on l clearly indicates that the first maximum is due to field electron emission, whereas the current I_2 is evidently determined by the three-halves law and falls rapidly with increasing l.

Figure 5 shows the pressure dependence of the energy stored in the beam at the beginning and end of the drift chamber. For a pressure of some $3 \cdot 10^{-2}$ mm Hg, the beam energy at a distance of 18 and 45 cm from the anode foil is respectively $Q_1 \approx 300$ J and $Q_2 \approx 50$ J. The greatest value of the beam energy $\approx$700 J was found at a pressure of about 0.3 mm Hg. These results indicate focusing of the beam for a pressure of over 0.2 mm Hg. If $U_c \approx 3$ MV the energy stored in the line equals ~2.2 kJ, while the efficiency of energy transmission in the beam is over 30%.

The geometrical dimensions of the beam were determined from traces on a Plexiglas disk and a cellophane film situated at 40 and 4 cm respectively from the anode foil for a pressure of about 0.3 mm Hg in the chamber. The diameter of the main beam under focusing conditions was less than 1 cm.

The maximum energy of the accelerated electrons was determined from the transmission of the beam through aluminum foils of various thicknesses. By comparing the resultant data and the electron flux absorption curve with the monoenergetic and continuous spectra [9], we may conclude that there is a fairly wide energy spread of the particles in these experiments. The effective range was determined from the thickness of the foil which passed no more than 10% of the electrons. For a charge voltage U_c of some 3 and 3.6 MV the maximum electron energy W_{max} respectively equals ~1 and ~1.2 MeV. However, the errors of this method are extremely large, so that for an accurate determination of the energy spectrum of the electrons a magnetic analyzer should be used.

As a result of such experiments we found the relationship between the shape of the total current pulse and the pressure in the drift chamber (Fig. 6), which may be explained as being due to the appearance of a reverse current at a moderate gas density (the total current comprises the primary plus the reverse current). With increasing pressure the gas breakdown formation time required for the creation of the plasma diminishes. These data are in good agreement with the results of [6].

Subsequently it is proposed to increase the charge voltage of the generator, to improve the high-voltage switch and acceleration tube (so improving the parameters of the electron beam), and also to study the interaction of the beam with the plasma under conditions in which a reverse current appears when a strong longitudinal magnetic field is applied in the drift space.

In conclusion, the authors wish to thank L. V. Dubovii for presenting the problem and for valuable discussion, I. M. Roife, A. M. Timorin, M. P. Svin'in, and A. V. Lysov for interest and help in the work, and T. S. Gostev and V. I. Chernobrovin for taking part in the experiments.

LITERATURE CITED

1. F. Winterberg, Phys. Rev., 174, 212 (1968).
2. W. Link, IEEE Trans. Nucl. Sci., 14, 777 (1967).
3. D. Morrow et al., Appl. Phys. Lett., 19, 441 (1971).
4. S. Graybill and S. Nablo, Appl. Phys. Lett., 8, 18 (1966).
5. A. M. Stefanovskii, Pribory i Tekh. Eksperim., No. 2, 149 (1967).
6. L. Levine et al., J. Appl. Phys., 42, No. 5, 1863 (1971).
7. S. I. Braginskii, Zh. Eksp. Teor. Fiz., 34, No. 6, 1548 (1958).
8. V. M. Lagunov, A. S. Ponomarenko, and L. P. Fominskyii, Zh. Tekh. Fiz., 42, No. 9, 1825 (1972).
9. W. Price, Recording of Nuclear Radiation [Russian translation], IL, Moscow (1960).

NUMERICAL SOLUTION OF THE PROBLEM OF OPTIMIZATION OF A HETEROGENEOUS REACTOR BY MEANS OF BLOCKED, BURNUP ABSORBERS

A. V. Voronkov and V. A. Chuyanov

UDC 621.039:562.2

An analytic solution of the problem concerned with the selection of parameters for a burnup absorber, guaranteeing optimal behavior during the system's reactance time, can be obtained only in the simplest cases.

One is obliged to solve more realistic problems numerically, and in this case the fundamental difficulties arise because of the complex local structure of the optimized functional which results in a search for a minimum for surfaces with discontinuities in the derivative.

This limits the region of application of standard local methods in the search for a minimum, e.g., the gradient method of descent. A new method of solution for a problem of this kind is proposed in the present paper, using as an example the solution of the problem concerned with the selection of optimal parameters for the burnup absorber guaranteeing the prescribed time development of the coefficient of utilization of thermal neutrons for a two-dimensional mesh $\Theta(\mathbf{X}, t)$. A combined kinetic-diffusion method is utilized for the solution: the kinetic equation is solved exactly inside of the absorber and by the diffusion approximation in the remaining part of the mesh. Besides a reduction in calculated expenditures, this method allows one to localize the region of definition for an optimal change in the volume of the absorber, and, consequently, the selection of different variations also occurs in this region. A flat, nondiffusing absorber consisting of layers of different materials was utilized as an absorbing element.

It was shown that the function $\Theta(\mathbf{X}, t)$ is monotonic with respect to the individual components of the directional vector $\mathbf{X}$. For such functions the functional $\Phi(\mathbf{X})$ will always have a discontinuous derivative at a minimum point. At the same time, a minimum of the functional for any directional coordinate x_i, located within a region of change of variables, will be a minimum point also for all remaining coordinates, if the motion occurs along the coordinate axes. With the same motion in other directions, one can attain smaller values of the functional. With the solution of such a problem by means of any standard method of search for a many-variable function, the solution is terminated after entrance of the operating point on the surface of discontinuities for the optimized functional, even if, at the same time, it is sufficiently far from an absolute minimum.

A modified local search method is proposed which entails the fact that progression to a minimum occurs precisely on the surface of discontinuities. For this the surface of discontinuities is projected along one of the coordinates x_k $(1 \leq k \leq n)$ in a $(n-1)$-dimensional space and one of the local search methods for the function $\hat{\Pi}_k \Phi(\mathbf{X})$, where $\hat{\Pi}_k$ is the search operator for the minimum of the function $\Phi(\mathbf{X})$ corresponding to the x_k coordinate, is applied in this space. The number of calculations of the function $\Phi(\mathbf{X})$ (which determines the calculation time) in this case is approximately the same as that with the application of a local method to a differentiable function of the same dimensionality. The given method was applied in the calculation of different kinds of systems, and in all cases an absolute minimum was found which was verified by a detailed study of the behavior of the function $\Phi(\mathbf{X})$ in the entire region of variation of the varied parameters.

Translated from Atomnaya Énergiya, Vol. 34, No. 6, p. 475, June, 1973. Original article submitted April 25, 1972; abstract submitted April 25, 1972.

ANALYSIS OF A PULSED NEUTRON EXPERIMENT BY THE MOMENTS METHOD

D. A. Pankratenko and L. N. Topil'skii

UDC 539.125.5:539.1.08

The use of high-intensity pulsed neutron sources permits a substantial improvement in the statistics of counts obtained in pulsed experiments. With these sources the error in measuring the logarithmic decrement of a system is a few tenths of a percent. In view of this it becomes necessary to compare the various methods of analyzing measurements. The methods of most practical interest are those permitting a rapid and accurate determination of the background and the logarithmic decrement.

We use the moments method to obtain a system of equations relating the background Φ and the logarithmic decrement α to the measured number of counts N_i in the i-th analyzer channel (i = 1, ..., n), corrected for the dead time. It is shown that the moments method equation for the logarithmic decrement, obtained for the decrease in neutron density in the absence of background, agrees with the equation obtained by the maximum probability method with a Poisson distribution. In the iteration procedure used to solve the equations the logarithmic decrement is calculated by using the number of counts, corrected for background, calculated by the moments method. The iterative process is started with the zeroth approximation to the logarithmic decrement $\alpha^{(0)}$, obtained by any simple method.

The equation for the background is

$$\Phi = a + \sqrt{a^2 + b}. \tag{1}$$

Here

$$a = \frac{\nu_0\mu_2 + \nu_2\mu_0 - \nu_0\mu_1 - \nu_1\mu_0 - 4\nu_1\mu_1}{2\nu};$$

$$b = \frac{2\mu_1^2 + \mu_0\mu_1 - \mu_0\mu_2}{\nu};$$

$$\nu = \nu_0\nu_2 - \nu_0\nu_1 - 2\nu_1^2,$$

where

$$\nu_0 = n;\ \nu_1 = \frac{n(n-1)}{2};\ \nu_2 = \frac{n(n-1)(2n-1)}{6};$$

$$\mu_0 = \mu_0^e + \Delta\mu_0;$$

$$\mu_1 = \mu_1^e + \Delta\mu_0\left[n + \frac{1}{\exp(\alpha\tau) - 1}\right];$$

$$\mu_2 = \mu_2^e + \Delta\mu_0\left[n^2 + \frac{2n+1}{\exp(\alpha\tau) - 1} + \frac{2}{[\exp(\alpha\tau) - 1]^2}\right];$$

$$\Delta\mu_0 = \frac{\mu_0^e}{\exp(n\alpha\tau) - 1};$$

$$\mu_r^e = \sum_{i=1}^{n} (i-1)^r N_i;\quad r = 0, 1, 2;$$

τ is the width of an analyzer channel.

After substituting $\alpha^{(0)}$ into Eq. (1) and determining $\Phi^{(0)}$ the logarithmic decrement can be found in the $\alpha^{(1)}$ approximation

$$\alpha^{(1)} = \frac{1}{\tau}\ln\left(1 + \frac{\mu_0 - \Phi\nu_0}{\mu_1 - \Phi\nu_1}\right). \tag{2}$$

In this equation $\Phi = \Phi^{(0)}$. We then calculate $\Phi^{(1)}$, $\alpha^{(2)}$, etc., until we obtain for the j-th step

$$|\alpha^{(j-1)} - \alpha^{(j)}| < \varepsilon,$$

where ε is a given small number.

Translated from Atomnaya Énergiya, Vol. 34, No. 6, pp. 475-476, June, 1973. Original article submitted July 6, 1972.

An algorithm similar to the one given here was proposed by Rotter [1]; it can be obtained from the system (1), (2) under the conditions

$$\alpha\tau \ll 1, \quad n\alpha\tau \geqslant 10.$$

The results of calculating logarithmic decrements by the successive elimination of points are compared with similar calculations by the method of least squares for an adjusted exponent. The algorithm of the method can be programmed for a small computer such as the Nairi.

LITERATURE CITED

1. W. Rotter, J. Nucl. Energy, 23, 289 (1969).

AN INSTRUMENTAL-ACTIVATION METHOD FOR THE DETERMINATION OF Mo, Al, Ca, Mn, Cl, Na, AND K IN SOIL AND PLANT SAMPLES

R. Rustamov, Sh. Khatamov,
I. I. Orestova, and A. A. Kist

UDC 543.53

With the use of the high-resolution germanium–lithium semiconductor detector, which is the basis for the wide use of activation analysis in agriculture, broad possibilities have been opened for the instrumental-activation analysis of soil and biological samples. Irradiation and holding-time conditions have been optimized to the point where it is possible to conduct analyses with batches of 40-50 samples so as to determine simultaneously the Al, Ca, Mn, Cl, Na, and K content. Samples of soils and various cotton-plant organs, weighing 100 mg and 300 mg, respectively, were irradiated in a vertical channel of the VVR-S water-moderated water-cooled reactor for 8-10 min with a flux of 10^{12} neutrons $\cdot$ cm^{-2} $\cdot$ sec^{-1}.

The method was used for determining the molybdenum content in the leaves, stalks, bolls, and other organs of cotton plants grown in artificial (sandy and aqueous) media.

For the molybdenum determinations, the samples were irradiated with a flux of epicadmium neutrons. The quantitative determination of the elements was based on recordings of the γ-ray intensity at various energies: Mo^{101} (1,021 keV), Al^{28} (1,780 keV), Ca^{49} (3,083 keV, 2,061 keV), Cl^{38} (2,160 keV), Mn^{46} (847 keV), K^{42} (1,524 keV), and Na^{24} (1,368 keV, 2,750 keV).

In the determination of aluminum, the contribution of two interfering nuclear reactions – $Si^{28}(n,p)Al^{28}$ and $P^{31}(n, \alpha)Al^{28}$ – were taken into consideration.

The real sensitivity of the method was $2.8 \cdot 10^{-5}$ g/g for the Mo determination, $8.4 \cdot 10^{-7}$ g/g for Al, $7.5 \cdot 10^{-4}$ g/g for Ca, $1.2 \cdot 10^{-8}$ g/g for Mn, $2.1 \cdot 10^{-7}$ g/g for Cl, $7.1 \cdot 10^{-4}$ g/g for K, and $5 \cdot 10^{-8}$ g/g for Na.

The method was used in serial analyses for determining the percentage of various elements in soils and cotton-plant organs at various water and salinity levels in studies of the changes in the percentage of various elements in the organs of cotton plants infected with verticilliose wilt. It was found that in the diseased plants the transfer of manganese from the organs to the fruit elements is impaired. As a result, the manganese concentration in leaves, bolls, and other organs is increased.

Translated from Atomnaya Énergiya, Vol. 34, No. 6, p. 476, June, 1973. Original article submitted May 23, 1972; abstract submitted October 23, 1972.

OPTIMAL PLACEMENT OF A SPECIMEN IN RELATION TO A DETECTOR

A. N. Silant'ev and I. G. Shkuratova

UDC 539.108

In the γ-spectrometric analysis of specimens with low specific activity, it is very important to place the specimen in the optimum position with respect to the detector. We calculated the optimal values of specimen radius and of the product of solid angle and self-absorption coefficient for a number of values of the specimen volume, as shown in Table 1. The calculations were carried out for three values of μ, the coefficient of absorption of γ-radiation in the specimen material, and for cases in which the specimen was placed either over the end surface of the detector or around the detector. All values are shown in relative units of detector radius. In the calculations it was assumed that the distance between the end surface of the crystal and the material of the specimen was 0.15; the distance between the lateral surface of the crystal and the material of the specimen was assumed to be 0.25.

The experimental estimate of the optimal specimen dimensions is in good agreement with the calculated values.

The article discussed the method of interpolation of the resulting data for the case in which the coefficient of self-absorption of γ-radiation in the specimen material is different from those considered in the present study. It is shown that the self-absorption value can be represented as an exponential function of a quantity equal to 0.4 units less than the specimen radius when the value of the coefficient of self-absorption of γ-radiation in the specimen material is half the value considered in the present study.

TABLE 1. Optimal Radius of Specimen as a Function of Specimen Volume for Various Values of μ, Expressed in Relative Units

Volume of specimen	Optimal radius of specimen			Effective solid angle, with self-absorption taken into account		
	$\mu = 0$	$\mu = 0,3$	$\mu = 1$	$\mu = 0$	$\mu = 0,3$	$\mu = 1$
Specimen placed above end surface of detector						
0,5	0,50	0,53	0,57	0,24	0,21	0,14
1,0	0,68	0,69	0,75	0,22	0,19	0,13
2,0	0,85	0,87	0,95	0,20	0,16	0,10
5,0	1,11	1,14	1,22	0,14	0,11	0,07
Specimen placed around the detector						
5	1,45	1,45	1,45	0,20	0,17	0,12
10	1,65	1,65	1,65	0,18	0,14	0,09
20	1,95	1,95	1,95	0,14	0,11	0,06
50	2,54	2,54	2,54	0,10	0,07	0,03

A comparison of the calculated and experimental values of the efficiency of the recording of the γ-radiation from the specimen shows that the contribution of boundary effects for specimens placed around the detector is independent of the volume of the specimen being measured. It follows from this that the photoefficiency in the recording of the γ-radiation from a specimen placed around the detector is independent of specimen volume. On the other hand, the photoefficiency values found in the measurement of specimens placed around the detector are substantially different from those found for specimens placed over the end surface of the detector.

Translated from Atomnaya Énergiya, Vol. 34, No. 6, p. 477, June, 1973. Original article submitted May 4, 1972; abstract submitted January 17, 1972.

UTILIZATION OF METALLIC URANIUM IN POWER CHANNEL URANIUM – GRAPHITE REACTORS

A. D. Zhirnov, A. P. Sirotkin,
S. V. Bryunin, V. I. Pushkarev,
and V. I. Runin

UDC 621.039.524.2.034.44:33

Investigations, carried out for the purpose of attaining large burnups in metallic uranium [1], indicate that difficulties connected with the swelling of metallic uranium during irradiation can be overcome. One of the methods allowing one to reduce to a minimum the effect of swelling on the efficiency of the fuel elements is the creation of a central hole in the fuel element and the application of external guards.

It was experimentally established that in a fuel element with a 5% empty, internal space, a burnup in the 15,000-20,000 MW·day/tonU range is attainable. The allowable burnup rises with an increase in the empty space.

At the present time, uranium dioxide is used in the majority of power reactors, including channel, uranium–graphite reactors. This is due first of all to the high stability of the dioxide with high and economically feasible burnups. Extraction of encouraging results concerning the stability of the metallic uranium fuel elements during high burnups stimulated the authors of the work in question to estimate the change in the engineering and economic characteristics of an atomic electric power plant in the conversion from dioxide to metallic fuel (with minimal change in the design of the reactor and the heat-releasing assembly). Such a comparison was conducted using as an example a channel uranium–graphite reactor of the RBM-K type.

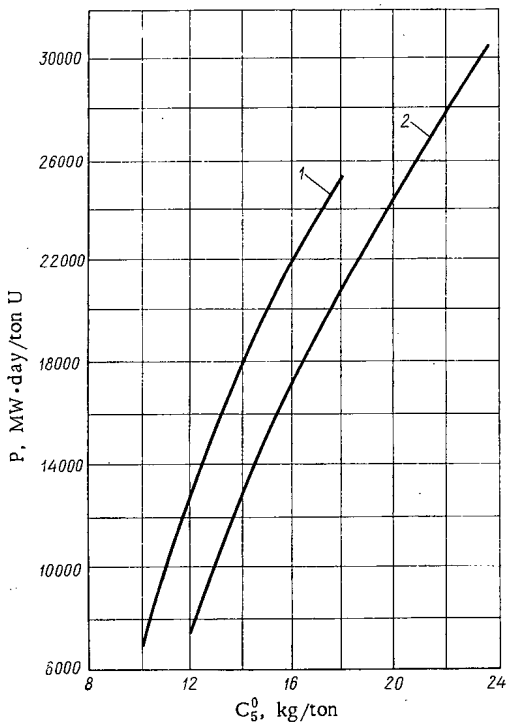

Fig. 1. Dependence of fuel burnup P on the initial concentration C_5^0. 1) Metallic uranium, hole 15% of volume; 2) UO_2.

The porosity of the fuel, the thickness of the fuel element casing, and the concentration of the uranium were varied in the calculations. The porosity of the fuel was taken equal to 0; 10 and 15%. The effective density of unalloyed, metallic uranium, allowing for the design characteristics of the fuel elements and the heat-releasing assembly, exceeded the effective density of the dioxide fuel by 2; 1.82 and 1.71 times, respectively.

One can rely upon the fact that in metallic uranium fuel elements, owing to smaller burnups and greater interaction of gaseous fission fragments in the metal, the thickness of the casing can be somewhat reduced in comparison with uranium dioxide fuel elements. In order to estimate the effect of the thickness of the casing on the engineering and economic characteristics in versions using metallic uranium together with a 0.9 mm thick fuel element casing (as for the dioxide), a 0.65 mm thick fuel element casing was also investigated. The concentration of the fuel was varied from 1.0 to 1.8% in each of the enumerated cases.

Translated from Atomnaya Énergiya, Vol. 34, No. 6, pp. 479-481, June, 1973. Original article submitted December 14, 1972.

26 July 1973

A E Vol 34, No. 6 (1973)

Page 479:

On the Use of Metallic Uranium in the Energy Channels of Uranium-Graphite Reactors

A.D. Zhirnov, A.P. Sirotkin, S.V. Bryunin, V.I. Pushkaryev, V.I. Runin

---

Research leading to achieving a high level of burnup in metallic uranium shows that problems connected with the swelling of metallic uranium irradiation can be overcome. One of the methods used to minimize the effect of swelling on the service of fuel elements is to use axial cavities in the fuel elements and the application of external restraints.

It has been experimentally established that in fuel elements with 5% free internal volume, a burnup level of 15,000 to 20,000 MWD/tU can be attained. The allowable burnup level increases with an increase in free volume.

At present, the majority of power reactors, including the graphite-pressure tube type use uranium dioxide. This is a result of the high stability of the dioxide at high economic burnup levels. Reliable results on the stability of metallic uranium fuel elements at high burnup levels caused the authors of this work to evaluate changes in the technical-economic indices of AES with the change over from dioxide fuel to metallic (with

minimal changes in the construction of the reactors and the fuel elements). Such a comparison was made on the graphite pressure tube type reactor - RBM-K.

The calculations were varied with regard to the porosity of the fuel, the thickness of the fuel element cladding and the enrichment of the uranium. The porosity of the fuel selected was 0, 10 and 15%. The effective density of the nonalloyed metallic uranium when the fuel assembly design and construction were taken into account exceeded the effective density of the dioxide fuel by 2; 1.82; and 1.71 times.

One might hope that as a consequence of the lower burnup level and the compression of the gaseous fission products the cladding thickness of the fuel elements with metallic uranium can be somewhat reduced in comparison to the fuel elements with uranium dioxide. In order to evaluate the effect of the thickness of the cladding on the technical-economic indices, for the variants with metallic uranium a cladding thickness of 0.65 mm was studied as well as 0.9 mm thickness (also used in the dioxide). In each of the above cases the fuel enrichment was varied from 1.0 to 1.8%. For a comparison, we studied variants of the fuel cycle with dioxide fuel enriched from 1.2 to 2.4% (Figure 1).

In carrying out the technical-economic analysis two goals were pursued: (1) the development of an optimal region for basic physical and constructional parameters for each fuel form, and (2) the determination of their relative economics.

In accordance with the methods [2,3] we used as a criterion of the effective utilization of the fuel load of AES the fuel component of the specific cost. The latter allows one to correctly decide the question concerning the effective utilization of fuel from the point of view of its time in the reactor, that is the optimal campaign and optimal level of fuel burnup.

Taking into account this criterion, the increase in fuel burnup and also the increase in cost connected with recycling fund (sic) of the AES which turns out to be effective in only a few cases was determined for each type of fuel, its physics, construction and economic characteristics, in particular its effective density and specific cost. This is the consequence of its initial fuel enrichment and its cost.

In the present stage of economic analysis, it is assumed that the use of metallic uranium in place of uranium dioxide in the RBM-K reactor does not lead to an additional capital outlay in the AES budget. All indications were calculated for work modes of the AES with chemical reprocessing of the

irradiated fuel. The power utilization factor was taken to be 0.8 and the normalized coefficient of effective capitalization -- 0.12.

For determining the optimum level of fuel burnup, the relationship of the specific cost and the fuel component of the specific cost was studied as function of the burnup level of the metallic uranium and dioxide fuel. (Figure 2.)

The specific cost and the fuel component of the specific cost for metallic uranium have minimum values for burnups of: ~ 11,500 MWD/t U in the case of solid fuel elements; ~ 12,500 MWD/t U for porosity of 10%; ~ 13,000 MWD/t U for porosity of 15%. The value of the initial enrichment corresponding to these burnups are 1.18; 1.21 and 1.23%, respectively.

Thus, the economically optimum burnup of metallic uranium fuel is found to be in the range 11,000-13,000 MWD/t U; this is significantly lower than the levels determined on the basis of experimental data.

In using uranium dioxide the specific cost and the fuel component of the specific cost are minimal at burnup levels of 20,000-22,000 MWD/t U. These burnup levels correspond to an initial enrichment of 1.8 - 1.9%.

The dependence of the economic indices on burnup level for metallic uranium has a sharper profile than with the dioxide; in this zone the optimum is more clearly defined. This is

explained by the significantly larger fuel load of the reactor (about two times) when using metallic uranium and, as a consequence, the larger sensitivity of the cost of recycle for the AES and the fuel component of the specific cost to the magnitude of the initial fuel enrichment.

A comparison of the economic indices shows that for metallic uranium and uranium dioxide obtained at their optimal initial enrichments and optimum burnup levels, a significant economic advantage in the use of metallic uranium.

In replacing uranium dioxide by metallic uranium the specific expense of electric power for variants of fuel elements without axial cavities and fuel elements with porosities of 10 and 15% are lowered by 6.2; 6.0; and 5.9%, respectively.

The presence of an axial cavity in the fuel element of metallic uranium leads to a worsening of the economic indices (Figure 3), none-the-less the significant advantages of metallic uranium when compared to dioxide are retained.

A reduction of metallic uranium fuel cladding thickness from 0.9 to 0.65 mm (porosity of fuel 15%) and a corresponding increase in fuel load leads to lowering of the optimum burnup level to about 11,500 MWD/tU. The specific cost for this decreases by 1.26%, electric power cost by 3.28%.

In considering the advantages of using in a RBM-K type rea reactor metallic uranium instead of uranium dioxide, one must also consider some lowering of the thruput of fuel (while the total load increases). For fuel elements of metallic uranium with a porosity of 15% the decrease in uranium thruput (in terms of natural uranium) amounts to 10%. This result is obtained without considering the return to the fuel cycle of the plutonium produced. The accumulation of Pu^{239} in the transition from oxide fuel to metallic uranium (optimum burnup) increases almost two times.

In carrying out the economic analysis, the importance of further experimental research on design, physics, economics in using metallic fuel in power reactors was shown.

The authors want to thank Yu. I. Koryakin for his useful remarks in this work.

Submitted for publication

14/12/72

1. Lezè, R et al "Atomic Technology at the Boundaries," No. 11, 12 (1971).

2. Methods of Determining Economic Effectiveness of Capital Investment. "Ekonomicheskaya Gazeta" No. 39, 1969.

3. Methods of Determining the Cost of Fuel Cycle and Economic Effectiveness of the Utilization of Nuclear Fuel in Condensing Atomic Power Stations with Thermal Reactors. M., SEV, 1970

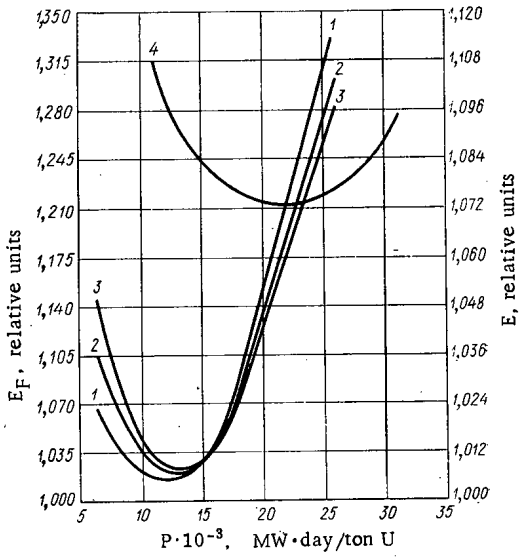

Fig. 2

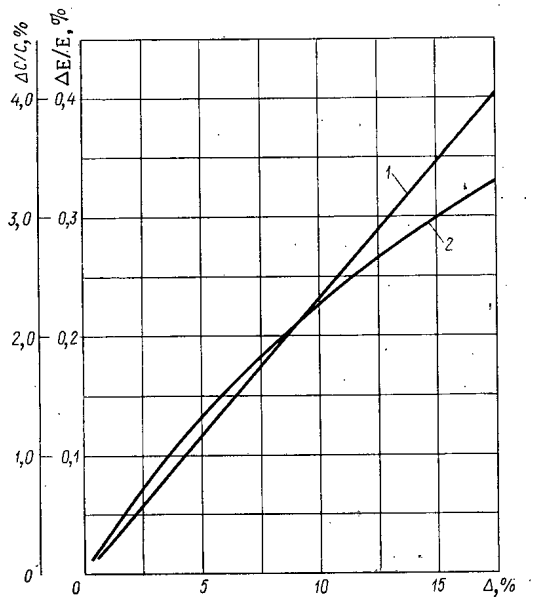

Fig. 3

Fig. 2. Dependence of the expenditure indicated E and fuel component of expenditure indicated E_F on fuel burnup: 1) uranium, solid fuel element; 2) uranium, 10% porosity; 3) uranium, 15% porosity; 4) UO_2.

Fig. 3. Effect of a fuel element's center hole dimensions Δ on the magnitude of the expenditures indicated and the electric power cost: 1) change in expenditures indicated ΔE/E; 2) change in cost ΔC/C.

Variations in the fuel cycle using dioxide fuel in concentrations of 1.2-2.4% (Fig. 1) were considered for comparison.

Two objectives were pursued by conducting an engineering and economic analysis: 1) development of an optimal range for the fundamental physical and structural parameters for each form of fuel; 2) determination of their relative economy.

According to the operating conditions [2, 3], the fuel component of the expenditure indicated is reflected in the criterion for the efficiency of utilization of the fuel charge in an atomic electric power plant. The latter permits one to solve correctly the problem of the efficiency of utilization of the fuel charge from the point of view of its duration in the reactor, i.e., from the point of view of the optimal operating period and the optimal fuel burnup.

Allowing for this criterion, the increase in the fuel burnup, as well as the increase in the amount of the operating costs for an atomic electric power plant connected with it due to the increase in the initial concentration of fuel and its cost occur only within certain limits determined for each form of its fuel by the physical, structural, and economic characteristics, in particular its effective density and its relative cost.

At a given stage of the economic analysis, it was assumed that the utilization of metallic uranium instead of uranium dioxide in a RBM-K type reactor does not lead to additional investment in the essential funds for an atomic electric power plant. All of the characteristics were calculated for the operating conditions of an atomic electric power plant with chemical treatment of the irradiated fuel. The coefficient of utilization of the established capacity was taken equal to 0.8 and the standard coefficient of investment effectiveness was taken equal to 0.12.

The dependence of the total expenditure indicated and the fuel component of the expenditure indicated on the metallic uranium and dioxide fuel burnup were considered for the determination of the optimal values of the fuel burnup (Fig. 2).

The expenditure indicated and the fuel component of the expenditure indicated during utilization of metallic uranium have minimal values with burnups: ~11,500 MW·day/tonU in the case of a solid fuel

element; ~12,500 MW · day/tonU with a 10% porosity of the fuel in the fuel element; ~13,000 MW · day/tonU with a 15% porosity. The values of the initial density corresponding to these burnups comprised 1.8; 1.21; and 1.23%.

Thus, the economically optimal burnups of metallic uranium fuel occur within the 11,000-13,000 MW · day/tonU limits, i.e., significantly lower than those values which are considered practicable from available experimental data.

With utilization of uranium dioxide the expenditure indicated and fuel component of the expenditure indicated were minimal for a burnup in the 20,000-22,000 MW · day/tonU range. This burnup corresponds to an initial density of 1.8-1.9%.

The dependencies of the economic characteristics on the fuel burnup for metallic uranium hava a more pronounced character in comparison with those for uranium dioxide; at the same time the zone of optimization is expressed more vividly. This is explained by the reactor's significantly large (approximately double) fuel charge during the utilization of metallic uranium and, as a consequence of this, the great sensitivity of the amount of the operating costs of an atomic electric power station and the fuel component of the expenditure indicated to the magnitude of the initial fuel density.

A comparison of the economic characteristics for metallic uranium and uranium dioxide, obtained at optimum for their initial concentration and optimum fuel burnup, indicates significant economic advantages for the utilization of metallic uranium.

With substitution of uranium dioxide by metallic uranium, the expenditures in electric power indicated for different fuel elements without a center hole and fuel elements with a porosity of 10 and 15% dropped correspondingly by 6.2; 6.0; and 5.9%.

The presence of a center hole in the metallic uranium fuel element results in a worsening of the economic characteristics (Fig. 3), nevertheless the significant advantages of metallic uranium in comparison with the oxide remain.

A reduction in the thickness of the metallic uranium fuel element casing from 0.9 to 0.65 mm (15% fuel porosity) and a corresponding increase in the fuel charge results in a reduction of the optimal fuel burnup to approximately 11,500 MW · day/tonU. At the same time, the expenditures indicated are reduced by 1.26%; the electric power cost by 3.28%.

One should also relate some of the reduction in the fuel consumption (with an increase in the charge as a whole) to the advantages for the utilization of metallic uranium together with uranium dioxide in RBMK type reactors. The reduction in uranium consumption (in the conversion to naturally occurring uranium) comprises ~10% for a metallic uranium fuel element with 15% porosity. This result was obtained neglecting the recovery of accumulated plutonium in the fuel cycle. The accumulation of Pu^{239} during the conversion from oxide fuel to metallic uranium (optimal fuel burnup) is nearly doubled.

The economic analysis conducted indicates the feasibility of further structural, physical, economic, but mainly experimental investigations on the application of metallic fuel in power reactors.

The authors thank Yu. I. Koryakin for helpful comments on the work.

LITERATURE CITED

1. R. Lezhe et al., Atomnaya Tekhnika za Rubezhom, No. 11, 12 (1971).
2. "Standard procedure for the determination of the economic effectiveness of investment," Ekonomicheskaya Gazeta, No. 39 (1969).
3. Procedure for the Determination of Fuel Cycle Consumption and the Economic Effectiveness of the Utilization of Nuclear Fuel in Condensation Atomic Electric Power Plants Using Thermal Neutron Reactors [in Russian], SEV, Moscow (1970).

STABILITY "IN THE LARGE" OF A STATIONARY REGIME OF A HETEROGENEOUS NUCLEAR REACTOR

V. V. Mikishev and Yu. F. Trunin

UDC 621.039:512:514

In thermally stressed nuclear installations, solid-phase inactive elements of the reactor (the moderator, shells of fuel elements and of fuel channels, supporting elements of the construction, etc.) can operate in a regime of large thermal charges, being formed both by convective heat exchange from the fuel elements and the coolant, and also from the considerable heat release due to the γ-radiation. For small geometric dimensions and large energy release the characteristic times of heating of the inactive elements can be measured in seconds, i.e., they will be comparable with the decay constant of nuclei of emitters of delayed neutrons. The inactive elements made a considerable contribution to the neutron multiplication constant in the reactor core, often positive in sign.

Under these conditions the effect of the inactive elements on the dynamic processes in the reactor can prove to be so significant that they can cause an instability in the stationary regime of operation of the nuclear installation.

We note that the rates of thermal processes in the inactive elements of thermally stressed reactors, as a rule, are considerably less than the characteristic rates of variation of processes in fuel elements and the coolant. Hence, the calculation of the dynamic effect of the inactive elements can be taken as a system of differential equations that describes the relatively slow processes, in which the effects of the nuclear fuel and the coolant are taken into account in the form of the instantaneous power contribution to the reactivity. A theoretical basis for the effect of such slow processes can be found in [1].

It is evident that the complete system of differential equations that describes the dynamics of the slow processes in the reactor should include the distributed equations of thermal conductivity for each inactive element, and, perhaps with some difficulty, should yield a qualitative analysis of the stability. The problem is considerably simplified if the partial differential equations are replaced by the averaged ordinary differential equations; in this case, the distributivity can be represented in the form of a time delay in deviations of the temperatures of the inactive elements that form the total reactivity [2].

Thus, the mathematical model that describes the slow processes in the reactor can be represented in the following form:

$$\frac{dN(t)}{dt}=\frac{\delta k(t)-\beta}{l}N(t)+\sum_{i=1}^{6}\lambda_i C_i(t); \tag{1}$$

$$\frac{dC_i(t)}{dt}=\frac{\beta_i}{l}N(t)-\lambda_i C_i(t),\quad i=1, 2, \ldots, 6; \tag{2}$$

$$\delta k(t)=\varepsilon_0[N(t)-N_0]+\sum_{k=1}^{M}\varepsilon_k[T_k(t-\tau_k)-T_{k0}]; \tag{3}$$

$$m_k c_k\frac{dT_k(t)}{dt}=m_k\left[A_k N(t)+B_k\int_0^{\infty}N(t-u)\,f_k(u)\,du\right]-K_k[T_k(t)-T_{k\,\text{in}}]. \tag{4}$$

$$k=1, 2, \ldots, M.$$

Translated from Atomnaya Énergiya, Vol. 34, No. 6, pp. 481-483, June, 1973. Original article submitted July 27, 1972.

Here (1) and (2) are the equations of neutron kinetics, written in the usual form [3]*; Eq. (3) is the equation for the reactivity, in which ε_0 and ε_k are the corresponding coefficients of reactivity. The heat-balance equation (4) in the k-th inactive element of the reactor takes account of the convective heat exchange and the heat release in the element, which in the general case is the sum of the energy of the neutron moderation, proportional to the instantaneous power of the reactor, and the energy of the absorbing γ-radiation of the reactor, which is separable into instantaneous and delayed components [4]. The function $f_k(u)$ characterizes the decrease in power of the delayed γ-radiation from the fission that occurs at the moment u = 0; the function $f_k(u)$ normalized to a single fission can be written in the form $f_k(u) = \sum_{j=1}^{m} g_{kj} e^{-\gamma_{kj} u}$. We have further that $T_k(t)$ is the mean temperature of the k-th element; m_k, c_k, and K_k are the mass, specific heat, and coefficient of heat transfer of the k-th element, respectively; A_k, B_k, g_{kj}, and γ_{kj} are positive constants; τ_k is a delay constant that characterizes the thermal inertia in the k-th element, together with the time constant in Eq. (4). The temperature of the medium that exchanges heat with the inactive element is assumed constant ($T_{k\,in}$ = const). The subscript "0" in Eq. (3) corresponds to the stationary value of the variable.

We introduce the dimensionless deviations of the variables

$$n(t)=\frac{N(t)-N_0}{N_0};\quad n_i(t)=\frac{C_i(t)-C_{i0}}{C_{i0}},$$

$$i=1, 2, \ldots, 6;\quad \theta_k(t)=\frac{T_k(t)-T_{k0}}{T_{k0}},\quad k=1, 2, \ldots, M$$

and the notation $\mu_0 = \varepsilon_0 N_0$; $\mu_k = \varepsilon_k T_{k0}$; $a_k = A_k N_0/c_k T_{k0}$; $b_k = B_k N_0/c_k T_{k0}$; $d_k = K_k/c_k m_k$; k = 1, 2, ..., M. We also introduce the new variable $\xi_{kj} = b_k g_{kj} \int_{-\infty}^{t} n(u) e^{-\gamma_{kj}(t-u)} du$. As a result, the system (1)-(4) acquires the form:

$$l\frac{dn}{dt}=-\sum_{i=1}^{6}\beta_i(n-n_i)+(n+1)\left[\mu_0 n+\sum_{k=1}^{M}\mu_k\theta_k(t-\tau_k)\right]; \tag{5}$$

$$\frac{dn_i}{dt}=\lambda_i(n-n_i),\quad i=1, 2, \ldots, 6; \tag{6}$$

$$\frac{d\theta_k}{dt}=a_k n-d_k\theta_k+\sum_{j=1}^{m}\xi_{kj}; \tag{7}$$

$$\frac{d\xi_{kj}}{dt}=b_k g_{kj} n-\gamma_{kj}\xi_{kj},\quad k=1, 2, \ldots, M, \tag{8}$$

$$j=1, 2, \ldots, m.$$

We investigate the stability of the trivial solution of the system (5)-(8) using the second method of Lyapunov, generalized to a system with time delay [5]. With this goal in mind, we consider the functional

$$V=l[n-\ln(n+1)]+\sum_{i=1}^{6}\frac{\beta_i}{\lambda_i}[n_i-\ln(n_i+1)]+\sum_{k=1}^{M}\left[\theta_k^2+2R_k\int_{t-\tau_k}^{t}\theta_k^2(v)\,dv\right]+\sum_{k=1}^{M}\sum_{j=1}^{m}\xi_{kj}^2, \tag{9}$$

where R_k is some positive constant.

Its total time derivative, calculated from the equations of system (5)-(8), has the form

$$\frac{dV}{dt}=-\sum_{i=1}^{6}\beta_i\frac{(n-n_i)^2}{(n+1)(n_i+1)}-\sum_{k=1}^{M}U_k[n, \theta_k, \theta_k(t-\tau_k)]-\sum_{k=1}^{M}\sum_{j=1}^{m}W_{kj}(n, \theta_k, \xi_{kj}); \tag{10}$$

where

$$U_k[n, \theta_k, \theta_k(t-\tau_k)]=-\frac{\mu_0}{2M}n^2-2a_k n\theta_k-\mu_k n\theta_k(t-\tau_k)+(d_k-R_k)\theta_k^2+2R_k\theta_k^2(t-\tau_k);$$

$$W_k(n, \theta_k, \xi_{kj})=-\frac{\mu_0}{2Mm}n^2-2b_k g_{kj} n\xi_{kj}-2\theta_k\xi_{kj}+\frac{d_k-R_k}{m}\theta_k^2+2\gamma_{kj}\xi_{kj}^2.$$

*In the dynamics of "slow" processes the parameter l/β is also small and unimportant; however, it is retained for convenience for the subsequent construction of a Lyapunov functional. Such a partial taking into account of insignificantly small parameters is based on [1].

We note that since the variables N and C_i are nonnegative, we have $n + 1 > 0$, $n_i + 1 > 0$ ($i = 1, 2, \ldots, 6$). Analyzing the quadratic forms $U_k[n, \theta_k, \theta_k(t-\tau_k)]$ and $W_k(n, \theta_k, \xi_{kj})$, we can show that the continuous functional (9) will be positive-definite, and its total derivative (10) will be negative-definite if the following conditions are satisfied:

$$\mu_0 < 0; \tag{11}$$

$$\mu_k^2 < \frac{4|\mu_0|}{M} R_k \frac{d_k - R_k - \frac{2a_k^2 M}{|\mu_0|}}{d_k - R_k} \tag{12}$$

for all $k=1, 2, \ldots, M$.

The interval of selection of the positive constant R_k depends essentially on the magnitude of the negative power coefficient of the reactivity. If the inequalities

$$\frac{2Mmb_k^2 g_{kj}^2 d_k}{2d_k\gamma_{kj} - m} < |\mu_0| < \frac{2Ma_k^2\gamma_{kj}}{m}\left(1 - \sqrt{1 - \frac{b_k^2 g_{kj}^2 m^2}{a_k^2\gamma_{kj}^2}}\right) \tag{13}$$

or

$$|\mu_0| > \frac{2Ma_k^2\gamma_{kj}}{m}\left(1 + \sqrt{1 - \frac{b_k^2 g_{kj}^2 m^2}{a_k^2\gamma_{kj}^2}}\right), \tag{14}$$

are satisfied, then

$$0 < R_k < d_k - \frac{|\mu_0|}{\frac{2\gamma_{kj}}{m}|\mu_0| - 2Mb_k^2 g_{kj}^2} \tag{15}$$

for all $k=1, 2, \ldots, M$; $j=1, 2, \ldots, m$.

If the magnitude of the power coefficient of reactivity is varied within the limits

$$\frac{2Ma_k^2\gamma_{kj}}{m}\left(1 - \sqrt{1 - \frac{b_k^2 g_{kj}^2 m^2}{a_k^2\gamma_{kj}^2}}\right) < |\mu_0| < \frac{2Ma_k^2\gamma_{kj}}{m}\left(1 + \sqrt{1 - \frac{b_k^2 g_{kj}^2 m^2}{a_k^2\gamma_{kj}^2}}\right), \tag{16}$$

then the interval of selection of R_k will be

$$0 < R_k < d_k - \frac{2a_k^2 M}{|\mu_0|} \quad \text{for all} \quad k=1, 2, \ldots, M. \tag{17}$$

We note that the inequalities (13)-(17) hold only for satisfaction of the conditions

$$-\frac{m^2}{d_k^2\gamma_{kj}^2} + 2\frac{m}{d_k\gamma_{kj}} < \frac{b_k^2 g_{kj}^2 m^2}{a_k^2\gamma_{kj}^2} < 1, \tag{18}$$

$$\frac{d_k\gamma_{kj}}{m} > 1 \quad \text{for all} \quad k=1, 2, \ldots, M; \quad j=1, 2, \ldots, m. \tag{19}$$

Conditions (11) and (12) essentially give the boundary of the stability region "in the large" in the parameter space that characterizes the feedback to the reactor.

The maximal stability region is obtained for

$$R_k = d_k - a_k\sqrt{\frac{2Md_k}{|\mu_0|}}. \tag{20}$$

In this case the boundary of the region and stability in the parameter space is determined by the following system of inequalities:

$$\mu_0 < 0; \tag{21}$$

$$|\mu_k| < 2\sqrt{2}\left(\sqrt{\frac{d_k|\mu_0|}{2M}} - a_k\right); \tag{22}$$

$$\frac{32}{9}\frac{Ma_k^2 d_k\gamma_{kj}^2}{m^2}\left(\cos\frac{\pi+\varphi}{3} + \frac{1}{2}\right)^2 < |\mu_0| < \frac{32}{9}\frac{Ma_k^2 d_k\gamma_{kj}^2}{m^2}\left(\cos\frac{\pi-\varphi}{3} + \frac{1}{2}\right)^2, \tag{23}$$

where

$$\varphi = \arccos\left|\frac{27}{16}\frac{b_k^2 g_{kj}^2 m^3}{a_k^2 d_k\gamma_{kj}^3} - 1\right|, \tag{24}$$

$k=1, 2, \ldots, M$; $j=1, 2, \ldots, m$

for satisfaction of the conditions (18) and (19).

Thus, the inequalities (21)-(23) are sufficient conditions for the asymptotic stability of the dynamic model (1)-(4) of a heterogeneous reactor, with stability existing for all initial perturbations of the stationary regime and for all delays τ_k.

LITERATURE CITED

1. A. A. Andronov et al., Theory of Oscillators, Addison-Wesley, Reading, Mass. (1966).
2. V. P. Rubanik, Oscillations of Quasilinear Systems with Delay [in Russian], Nauka, Moscow (1969).
3. M. A. Schultz, Control of Nuclear Reactors and Power Plants, 2nd ed., McGraw-Hill, New York (1961).
4. Shielding of Nuclear Reactors (Materials of KAE USA) [Russian translation], Izd.-vo Inostr. Lit., Moscow (1958).
5. N. N. Krasovskii, Some Problems in the Theory of Stability of Motion [in Russian], Fizmatgiz, Moscow (1959).

NUCLEAR-RADIATION DETECTORS BASED ON HIGH-PURITY GERMANIUM

V. P. Aver'yanova, M. I. Ginzburg, N. B. Strokan, V. P. Subashieva, and N. I. Tisnek

UDC 539.1.07

Recently, considerable attention has been given to obtaining germanium detectors that are stable at room temperature. In a study on this subject we were successful in applying the method of cold doping, i.e., the working volume of the detector was formed by the compensation of the initial conductivity by deep acceptor levels, connected with radiation defects [1-6].

It is evident that the less the difference concentration of impurities ($N_d - N_a$) in the original germanium, the less will be the number of defects required for compensation and, hence, to a small degree, there will appear undesirable effects of the capture of current carriers at the deep levels to be introduced. Since the possibility of successfully realizing the method of cold doping is directly connected with the depth of the purity of the initial germanium, there has recently been undertaken serious efforts in this direction and very good results have been obtained [7, 8, 9], which allow us to obtain detectors of high quality, without recourse to additional compensation [10, 11]. However, as usual, there exists a known limitation on the dimension of the working layer due to the capture of carriers at the levels of uncontrolled impurities. In this connection, it is important to determine which type of carrier is subjected to trapping, and to what extent.

We investigated the comparative characteristics of detectors made from single-crystal samples of imported n-type germanium with different concentration $3.0 \cdot 10^{10}$ cm^{-3} and small degree of compensation (the company General Electric), and also domestic p-type germanium with $N_a - N_d = 8 \cdot 10^{10}$ cm^{-3}.

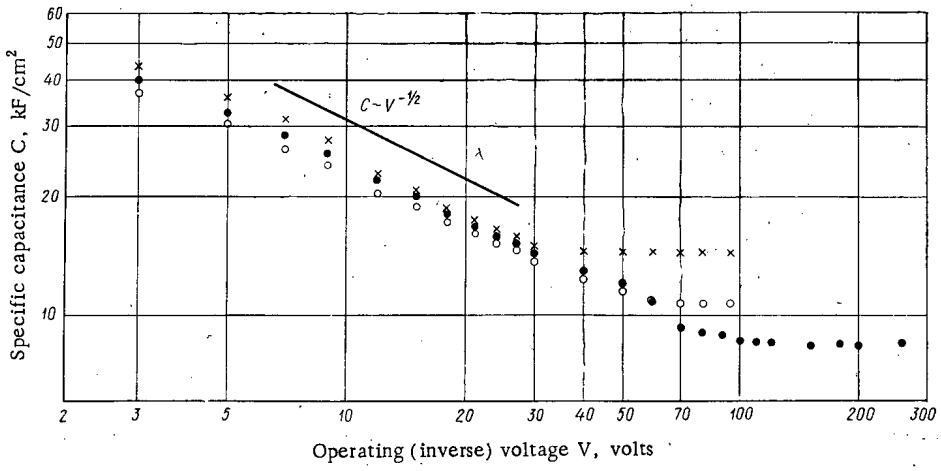

Fig. 1. Dependence of specific capacitance of detectors on applied displacement. The saturation corresponds to the propagation of the depleted region up to the opposite electrode: ●) sample 345 (2); ×) 345 (1); ○) 348.

Translated from Atomnaya Énergiya, Vol. 34, No. 6, pp. 483-485, June, 1973. Original article submitted September 18, 1972.

TABLE 1. Measurement Results of the Detector Characteristics

Sample No.	Capacitance concentration	R_γ, % Cs^{137}	R_β, % Bi^{207}	R_α, % Am^{241}	Carriers trapped	λ_γ, %
348 imported	4,5	0,2	0,7 (1,0 MeV)	0,6	electrons	0,15
345 (1) imported	5,8	0,5	0,7 (0,5 MeV) 0,2 (1,0 MeV)	—	holes	0,3
345 (2) domestic	5,4	0,7	1,0 (1,0 MeV)	—	electrons	0,4

Domestic samples of high-purity germanium were obtained by the authors from an improved method of zone refinement and the growth of single crystals according to the Czochralski method, excluding the intermediate operations of preparing germanium using the original material and containers of high degree of purity. The samples were cut from a crystal 250 mm long and 25 mm in diameter, grown in the [111] crystallographic direction.

The degree of purity of the germanium obtained was estimated by using the method of the separate determination of the concentration of the donors and the acceptors according to the Hall effect at liquid-helium temperature [12] and the method of determining the nature of the residual impurities by photothermal ionization [13].

Measurement results for the high-purity germanium used in manufacturing the detectors are as follows:

Difference concentration of carriers (at 77°K)	$8 \cdot 10^{10}$ cm^{-3}
Type of conductivity (at 77°K)	p
Donor concentration, N_d	$3.3 \cdot 10^{11}$ cm^{-3}
Acceptor concentration, N_a	$4.1 \cdot 10^{11}$ cm^{-3}
Total concentration of donors and acceptors, $N_a + N_d$	$7.4 \cdot 10^{11}$ cm^{-3}
Degree of compensation	80%
Mobility, μ (at 77°K)	$3.9 \cdot 10^4$ cm^2/V · sec
Uncompensated impurities and their concentrations:	
boron	$1.1 \cdot 10^{10}$ cm^{-3}
aluminum	$5.0 \cdot 10^{10}$ cm^{-3}
gallium	$1.9 \cdot 10^{10}$ cm^{-3}
Density of dislocations	$5 \cdot 10^2$ cm^{-2}

The technology for manufacturing the detectors is standard and involves the diffusion of impurities of lithium (330°C for 5 min) for the creation of an n^+ contact and the deposition on the opposite side of the disc of a layer of gold for the formation of a p-type electrode, which is an entrance window with a thin dead layer. For the etching before the preparation of the contacts for sample 348 (orientation [100]) we applied the standard etchant CP-4a. For detectors of 345 (1) and 345 (2) (orientation [111]) we used an etchant with anode control.

Volt–farad characteristics for three detectors are given in Fig. 1, and for small inverse voltages the characteristics are close to the dependence $C \sim V^{-1/2}$, which corresponds to a sharp n–p transition. The saturation of the capacitance with further increase in voltage results from the propagation of the depleted region up to the opposite contact. The thickness of this region is 1.4, 1.0, and 1.6 mm, respectively, for the detectors 348, 345 (1), and 345 (2) (see Table 1). The area of the p–n junctions of the detectors are, on an average, 1.6 cm^2.

The energy resolution of the detectors was determined for α-, β-, and γ-radiation (see Table 1). The difference in the resolution for the very same detector is connected with the fact that with recording

of γ quanta, electrons and holes drift, on the average, equal distances toward the electrodes. At the same time, for registering α and β particles in the sensitive region, it is mainly the electrons that drift, which allows us to finally establish which type of carrier is exposed to primary capture.

We can measure the magnitude of the loss of charge for a specific type of radiation. This was done by determining the dependence of the center of mass of the peak of total absorption on the inverse voltage across the detector. By extrapolating this dependence to $1/V = 0$ (i.e., to conditions of total collection of charge) we found the mean value of the relative losses of the collection of charge (λ_γ, %). This quantity proved to be a minimum for the sample 348; this sample also had better resolution based on γ quanta.

For β and α particles, the losses λ were not determined, since the samples 345 (1) and 345 (2) of the α particle were not recorded, and the resolution for β spectra depended on the energy of the β particles (see the data of 345 (1)). This indicates the presence near the gold layer of a region with low field intensity. Nevertheless, we note a very high resolution $R_\beta = 0.2\%$ for the detector 345 (1), which exceeds the theoretically possible limit by only a factor of 2.

The results allow us to conclude that construction of detectors with acceptable resolution is possible also for a considerable degree of compensation (detectors 345 (1) and 345 (2)). However, these samples give detectors of purer germanium (sample 348) both with respect to the magnitude of the loss of charge, and also with respect to the homogeneity of properties determined by the ratio R_γ/λ_γ. Therefore further purification from impurities (including deep current carriers causing trapping) is needed for obtaining detectors with a large sensitive-region volume.

It is evident that the role of cold doping in this case increases substantially. Actually, for the formation of an extended working zone we need a concentration $N_d - N_a \sim 10^9$ cm^{-3}. We can expect that this level is easily attainable with the preirradiation of n-type germanium with a concentration $\sim 10^{10}$ cm^{-3}, and does not lead to an increase in the loss of charge.

The authors thank E. M. Gershenzon and V. I. Sidorov for help on estimates of the degree of purity of the germanium samples studied, and S. M. Ryvkin for his interesting discussion.

LITERATURE CITED

1. S. M. Ryvkin et al., Zh. Tekh. Fiz., 34, 1535 (1964).
2. S. M. Ryvkin et al., Dokl. Akad. Nauk SSSR, No. 3, 145 (1965).
3. H. Kraner and H. Wegner, Bull. Amer. Phys. Soc., 13, 560 (1968).
4. L. Kimerling et al., IEEE Proc., 57, No. 2, 208 (1969).
5. E. Lawson, Nucl. Instrum. and Methods, 95, 361 (1971).
6. S. Ryvkin et al., Nucl. Instrum. and Methods, 95, 177 (1971).
7. R. Hall and T. Soltys, IEEE Trans., NS-18, No. 1, 160 (1971).
8. W. Hansen, Nucl. Instrum. and Methods, 94, 377 (1971).
9. B. A. Sakharov et al., Tsvetnye Metally, No. 7, 52 (1970).
10. R. Boertsch and R. Hall, IEEE Trans., NS-18, No. 1, 166 (1971).
11. J. Llacer, Nucl. Instrum. and Methods, 98, 259 (1972).
12. V. F. Bannaya, Dissertation, Moscow (1968).
13. T. M. Lifshits et al., Zavod. Lab., No. 8, 916 (1971).

DETERMINATION OF OIL – WATER INTERFACE USING A 6-8 MeV ELECTRON BEAM

M. M. Dorosh, A. M. Parlag,
V. A. Shkoda-Ul'yanov, I. I. Danilich,
V. M. Mazur, and A. Yu. Urgin

UDC 539.152.3

Detection of photoneutrons produced in strata by electron or photon irradiation [1-4] can be used for direct demarcation of the oil–water interface in cased wells. This conclusion is based on calculations of photoneutron yields from thick bodies of water and oil because of the presence of the isotopes C^{13} and deuterium. Oil-bearing strata are distinguished from water-bearing strata by the C^{13} content. The deuterium content in oil-bearing strata is greater than in water-bearing strata by 50% or more [5, 6]. Consequently, a considerably greater photoneutron yield is expected from oil-bearing strata. This is confirmed by data from the calculations in [1-4].

Calculated results for strata irradiated by bremsstrahlung radiation are shown in Fig. 1. Using the cross section for the reaction $O^{17}(\gamma, n) O^{16}$ [7], the contribution of this reaction to the photoneutron yield from a water-bearing stratum was also estimated. It proved to be insignificant.

A large amount of work on the development of a photoneutron technique for delineating the water–oil interface has been done by the staff at VNIIYaGG under the direction of A. K. Berzin [8-11]. They considered such questions as the spatial distribution of the neutrons, depth of penetration, effect of porosity and mineralization of perched water on the results, etc. In only one experimental work [12], however, were measurements made of the photoneutron yields from water and oil using models 8 liters in volume,

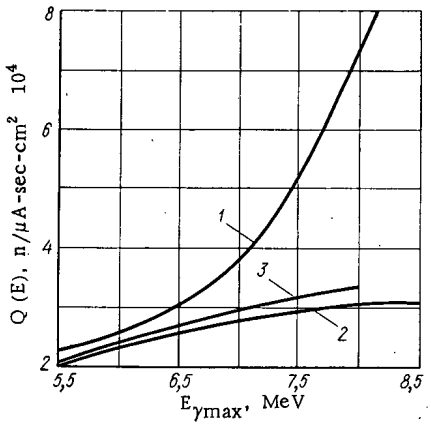

Fig. 1

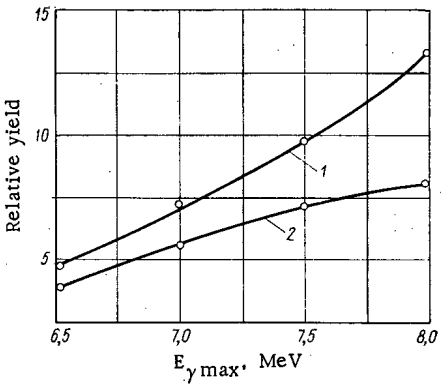

Fig. 2

Fig. 1. Calculated photoneutron yields from oil-bearing (1) and water-bearing (2) strata irradiated by bremsstrahlung; 3) photoneutron contribution from water-bearing layer because of $O^{17}(\gamma, n)O^{16}$ reaction.

Fig. 2. Experimental curves for photoneutron yields from oil (1) and water (2).

Translated from Atomnaya Énergiya, Vol. 34, No. 6, pp. 485-487, June, 1973. Original article submitted December 2, 1971; revision submitted January 16, 1973.

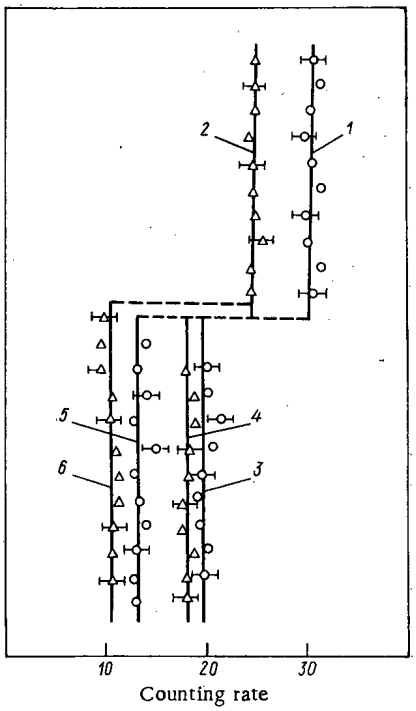

Fig. 3. Experimental photoneutron yields: 1) oil-bearing stratum; 3) water-bearing stratum (fresh water); 2, 4) the same for a cased-well model; 5) perched water with a mineralization of 34 g/liter (uncased well); 6) the same, (cased well).

and it was shown that there is a difference in the yields which, in essence, confirms the calculations. However, practical interest is in cases where the oil and water are in mixtures with sand or other rock, i.e., in strata. In addition, it is necessary to take into account the effects of the casing string and cementing ring.

For this purpose, measurements were made on models made up of the mixtures 70% SiO_2 + 30% H_2O (water-bearing stratum) and 70% SiO_2 + 30% oil (oil-bearing stratum) and also on models made up of pure water and pure oil. The ratios of the components are given in volume percent. Mixtures were placed in a metal tank 42 × 42 × 42 cm in size. Bremsstrahlung radiation was incident on the tank at a point where it was covered by a concrete slab 3 cm thick (density, 2.4 g/cm^3) and an iron plate 8 mm thick (to simulate casing pipe and cementing ring). A 10 MeV microtron with tantalum stopping target served as the γ-ray source. Measurements were made in the energy range 6.5-8.6 MeV at a current of 0.5 μA. Photoneutrons were recorded with an SI-10N BF_3 counter which was located in the scattered γ-ray field at 20 cm from the beam axis. The neutrons were recorded in the interval between γ-ray pulses from the microtron (frequency, 400 Hz). Delay time was 90 μsec and recording time, 1500 μsec.

The measured photoneutron yields from oil and fresh water are shown in Fig. 2. At γ-ray energies above 8.6 MeV, the external neutron background increases sharply and also the neutron yield from sand. Therefore measurements were made at energies no higher than 8.1 MeV. Studies were made both with fresh water and with natural perched water of low mineralization (34 g/liter).

Photoneutron yields from oil-bearing and water-bearing strata for one series of measurements at 8.1 MeV are shown in Fig. 3. The excess neutron yield from an oil-bearing stratum as compared to a water-bearing stratum (fresh water) is ~50% for an uncased well and ~30% for a cased well. This difference increases sharply even for low mineralization of perched waters (~30 g/liter).

The data from our measurements is not at variance with the data from [12]. However, to solve the question of commercial use of the proposed method it is necessary to make an even larger number of model measurements in order to clarify questions about depth of penetration of the method and to define more precisely the effect of well casing and cementing, etc.

The method of delineating the oil–water interface from photoneutron yield may be no less efficient then the method based on the detection of delayed neutrons [13] since the coefficients of stratum demarcation are practically identical (1.3-1.5) and the γ-ray energy required is only 6-8 MeV instead of 20-25 MeV.

The authors are grateful to L. A. Shabalina and V. I. Kleiman for calculating the photoneutron yield in the reaction $O^{17}(\gamma, n)O^{16}$.

LITERATURE CITED

1. V. I. Gomonai, A. M. Parlag, and V. A. Shkoda-Ul'yanov, Abstracts of Papers at Third All-Union Inter-University Conference on Electron Accelerators [in Russian], Izd. Tomsk. Gos. Un-ta (1959).
2. V. I. Gomonai et al., At. Energ., 9, 313 (1960).
3. N. P. Mazyukevich, A. M. Parlag, and V. A. Shkoda-Ul'yanov, Reports of Uzhgorod State University, Phys. Mat. Sciences Series [in Russian], No. 4, Uzhgorod (1961).
4. N. P. Mazyukevich, A. M. Parlag, and V. A. Shkoda-Ul'yanov, in: Nuclear Geophysics [in Russian], Gostoptekhizdat, Moscow (1963), p. 196.
5. I. V. Grinberg and M. E. Petrikovskaya, Geologicheskii Zhurnal, 17, 4 (1957).
6. A. S. Vaisberg, I. M. Chernolutskaya, A. M. Parlag, and V. A. Shkoda-Ul'yanov, Reports of Uzhgorod State University, Phys. Mat. Sciences Series [in Russian], No. 3, Uzhgorod (1960).

7. A. K. Berzin et al., in: Nuclear Geophysics [in Russian], No. 9, Nedra, Moscow (1971), p. 113.
8. A. K. Berzin et al., in: Nuclear Geophysics [in Russian], No. 9, Nedra, Moscow (1971), p. 116.
9. A. K. Berzin et al., in: Nuclear Geophysics [in Russian], No. 9, Nedra, Moscow (1971), p. 189.
10. A. K. Berzin et al., Abstracts of Reports at All-Union Scientific and Engineering Conference on 20 Years of Production and Use of Isotopes in the National Economy of the USSR [in Russian], Nuclear Geophysics Section, Atomizdat, Moscow (1968).
11. A. L. Gryaznov et al., "Possibilities of delineating oil- and water-bearing strata by a pulsed γ-neutron method." Deposited Manuscript in All-Union Geological Library, Leningrad. Bibliograf. Informatsiya, Ser. 9, VIMS, Moscow (1970).
12. A. K. Berzin, A. I. Kislov, R. P. Meshcheryakov, G. P. Mikhailov, and V. V. Sulin, Proceedings IV Inter-University Conference on Electron Accelerators (Tomsk, 1961) [in Russian], Izd. Vysshaya Shkola, Moscow (1964), p. 474.
13. M. M. Dorosh et al., At. Energ., 21, 35 (1966).

PENETRATION OF FAST NEUTRONS THROUGH AN AXISYMMETRIC SHIELD

A. N. Kozhevnikov, V. A. Khodakov, and A. V. Khrustalev

UDC 539.125.5:539.121.72

Analytical and numerical methods of solving the equation for the transport of radiation through a shield of complex configuration involve the familiar difficulties of many-dimensional geometry and the necessity of taking account of the energy dependence of the cross sections and the anisotropy of scattering processes in matter. In many cases the Monte Carlo method surmounts these difficulties by simulating particle trajectories directly, but it is not free of faults either, the main one being the necessity of simulating improbable events. This is the case in the calculation of deep penetrations of radiation, but the calculations can

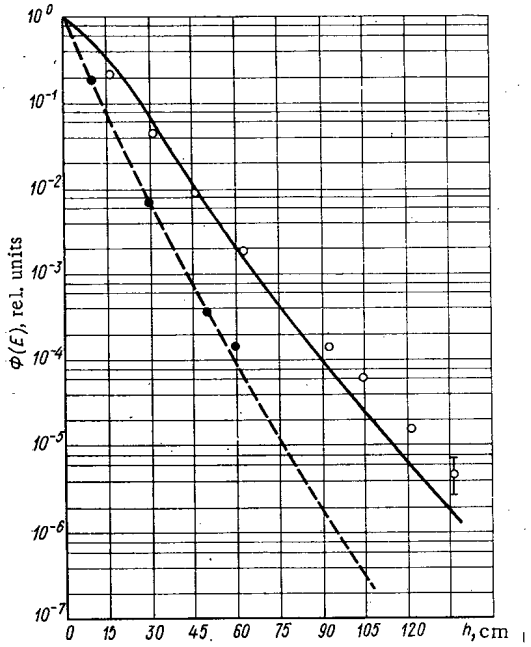

Fig. 1

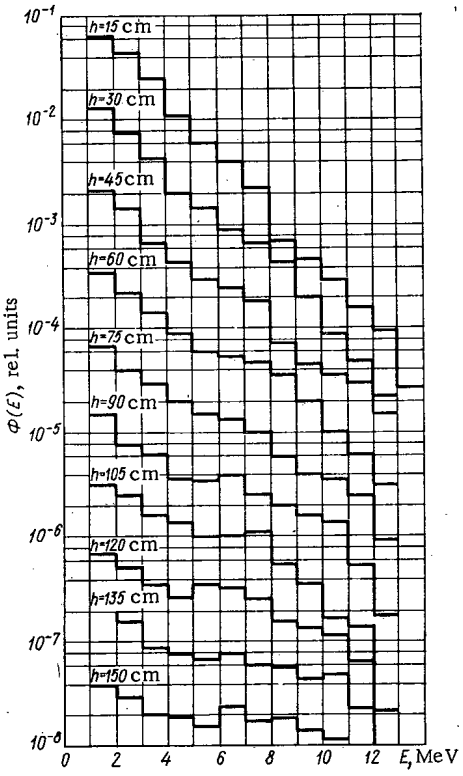

Fig. 2

Fig. 1. Attenuation of neutrons with energies $E \geq 1$ MeV as a function of shield thickness h: ○) experimental data [4] (total flux); ●) experimental data [4] (unscattered flux); ——) Monte Carlo calculation; ---) calculation using total cross section.

Fig. 2. Fast neutron spectra for various shield thicknesses (Monte Carlo calculation).

Translated from Atomnaya Énergiya, Vol. 34, No. 6, pp. 487-490, June, 1973. Original article submitted December 6, 1972.

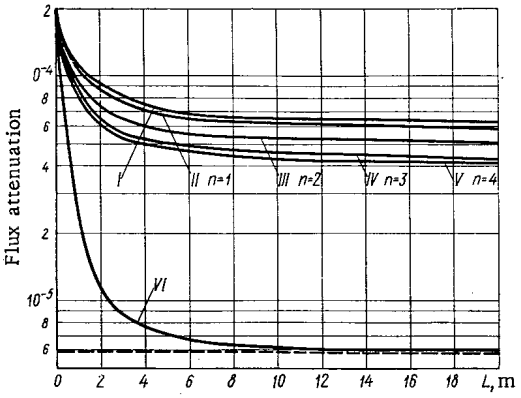

Fig. 3

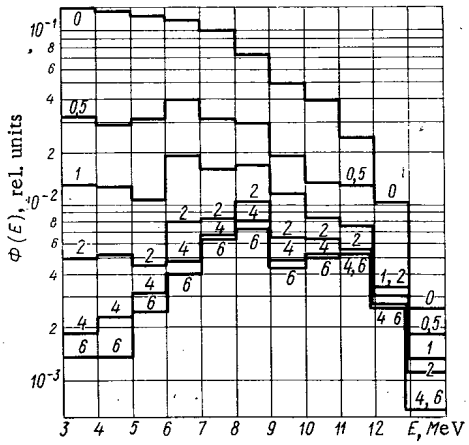

Fig. 4

Fig. 3. Attenuation of neutron flux (E ≥ 3 MeV) as a function of the shield-detector distance for sources with various angular distributions: ——) Monte Carlo calculation; I) isotropic source; II-V) $\cos^n\theta$ sources; VI) monodirectional source; ---) attenuation of unscattered flux.

Fig. 4. Fast neutron spectra behind a block shield for a monodirectional source.

be speeded up appreciably by using splitting and Russian roulette. Optimal splitting factors are obtained in [1] for a given arrangement of splitting surfaces, but so far as we know the general problem of choosing the number and locations of the splitting surfaces which ensure the greatest efficiency remains unsolved. V. A. Khodakov solved this problem exactly for the simplest physical model of the transport of radiation through an infinite slab shield. The optimum parameters of the statistical model (attenuation in the layers, splitting factors) depend on the probability characteristics of the interaction of the radiation with the shield material, but the absolute minimum calculation time for a given statistical error in the cases of practical interest is nearly achieved by dividing the shield into arbitrary layers with repeated attenuation of the particle current and appropriate smoothing in the depth of the shield.

This result is used in the ANKON program written in FORTRAN for a digital computer. The calculation is based on the stochastic simulation of the "wandering" of a particle in phase space with appropriate transition probabilities. Splitting and Russian roulette are accomplished in this program by the lexicographic processing of trees of trajectories [2]. Preliminary calculations show that Russian roulette is ineffective in estimating the current of fast neutrons behind a shield of hydrogenous material, and therefore neutrons backscattered toward the source can be neglected.

The ANKON program permits the calculation of integrated fluxes and spectral-angular distributions of neutrons with energies from 0.1 to 14 MeV both inside and outside finite lithium hydride shields. Plane sources are considered with various angular and spatial distributions.

Simulation of the deep penetration of radiation requires very accurate data on the interaction of radiation with matter. Analysis showed that for neutrons in the 0.1-14 MeV energy range lithium hydride can be regarded as consisting of H^1 and Li^7 atoms in taking account of the following interaction processes: elastic scattering by hydrogen, elastic scattering by lithium, inelastic scattering by lithium, and absorption. In choosing the ranges and scattering processes the program uses data obtained by linear interpolation in the tables in the cross section library [3]. In order to ensure the correctness of the set of interaction constants the calculated results were compared with the corresponding experimental data.

Figure 1 shows the calculated and experimental dependence of the attenuation of the neutron flux (E ≥ 1 MeV) on the thickness of a lithium hydride (ρ = 0.5 g/cm^3) shield for a plane monodirectional source having a fission spectrum [4]. Here the calculations and experiments are for good geometry. A certain divergence at large thicknesses can be explained by the fact that the spectrum of incident neutrons in the experiment was harder than the fission spectrum above 1 MeV. Figure 2 shows histograms of fast neutron spectra for lithium hydride shields of various thicknesses. The figure illustrates the tendency of the spectrum to harden with increasing thickness of a hydrogenous shield.

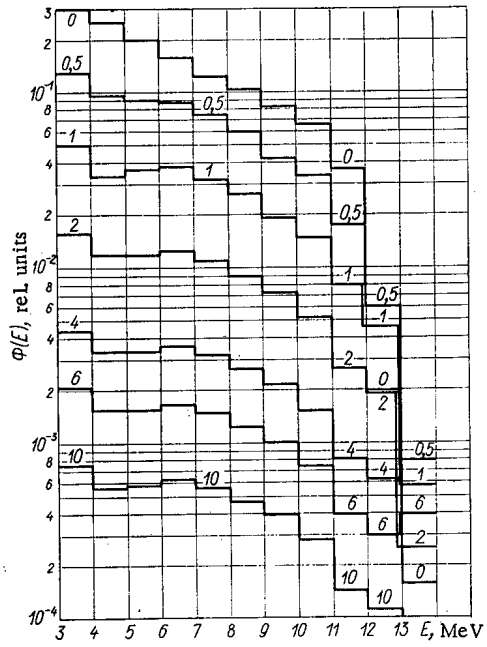

Fig. 5. Fast neutron spectra behind a block shield for a cosine source.

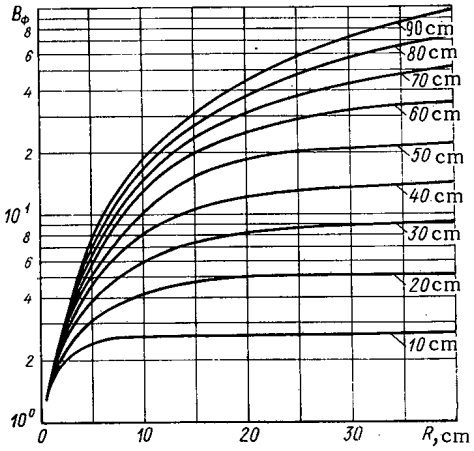

Fig. 6. Buildup factor for fast (E > 3 MeV) neutrons as a function of the thickness (numbers on the curves) and the radius R of a cylindrical shield.

The dependence of the attenuation of the fast neutron flux on the angular distribution of the source is of great interest. Figure 3 shows the dependence of the attenuation function $G = \Phi_{\text{with shield}}/\Phi_{\text{without shield}}$ on the distance between a point detector and the outside surface of the shield and on the angular distribution of fission neutrons from a disc source. The shield is a cylindrical block having a thickness of 45 g/cm^2 and a diameter of 60 cm. The attenuation function is weakly dependent on the form of the angular distribution for isotropic and cosine ($\cos^n\theta$, where n = 1 – 4) sources. The attenuation function for cosine sources converges slowly to the attenuation function for a monodirectional source as n increases. The distance from the shield surface at which the attenuation properties of the shield become constant can be estimated from the curve.

Figures 4 and 5 show fast neutron spectra at various distances from the surface of the same shield for a monodirectional and a cosine (n = 1) source. It is easy to see that the spectrum of transmitted neutrons from a monodirectional source is gradually transformed into the spectrum of the unscattered radiation as the distance from the shield increases. This does not occur for the cosine source; the spectrum at large distances is enriched by low-energy scattered neutrons. The numbers on the histograms are the distances in meters from the outside surface of the shield.

Figure 6 shows the flux buildup factor B_Φ as a function of the thickness and radius of a cylindrical shield. The source is monodirectional and has a fission spectrum; the radii of the source and shield are equal; $\rho_{LiH} = 0.78$ g/cm^3. In all cases the detector is located at the center of the side of the shield. The radius of the shield beyond which it can be considered infinite in the radial direction can be estimated from the curves.

The relative errors of the integrated flux calculations do not exceed 10%. The errors in the spectral distributions are somewhat larger.

LITERATURE CITED

1. V. N. Ogibin, in: The Monte Carlo Method in the Problem of Radiation Transport, G. I. Marchuk (editor) [in Russian], Atomizdat, Moscow (1967), p. 72.
2. N. P. Buslenko et al., The Method of Statistical Trials (The Monte Carlo Method) [in Russian], Fizmatgiz, Moscow (1962).
3. Nuclear Data Library, UKAEA (1968).
4. G. M. Bozin et al., Atomnaya Energiya, 21, 394 (1966).

ENERGY BALANCE OF NUCLEAR-FISSION REACTIONS (dt) IN THE BEAM – TARGET SYSTEM

R. A. Demirkhanov, Yu. V. Kursanov, and L. P. Skripal'

UDC 621.039.61

In connection with the prospects of obtaining beams of high-energy ions and neutrals with currents in the tens of amperes, and plans for using such beams for plasma heating [1, 2], there is practical interest in the question of the energy balance for dt reactions occurring during interactions of accelerated deuterons with a tritium plasma target [3]. Dawson et al. [4] have considered the conditions for a positive energy balance in such reactions in a pure tritium target.

The present paper evaluates the critical parameters of a similar plasma-beam system, taking into account the effect of deuteron accumulation in the target.

We will find the dt reaction intensities IB and the deuteron stopping time τ_1 in a thick, fully ionized tritium target:

$$IB = I\int_0^E \frac{n\,(2E/M)^{1/2}\,\sigma(E)\,dE}{(-dE/dt)}; \tag{1}$$

$$\tau_1 = \int_0^E dE/(-dE/dt). \tag{2}$$

Here, E (eV), M, and I are the energy, mass, and flux of deuterons, respectively; n (cm^{-3}) is the density of the target t; σ (E) and B are the effective cross section and yield of the dt reaction; (–dE/dt) is the stopping loss rate for the deuteron [3]:

$$(-dE/dt) = \frac{1.6\cdot10^{-9}nE\ln\Lambda}{T_e^{3/2}(1+2.7\cdot10^{-4}E/T_e)^{3/2}} + \frac{8.5\cdot10^{-8}n\ln\Lambda}{E^{1/2}}\ \text{eV/sec}), \tag{3}$$

where T_e is the electron temperature of the target (T_e, $T_i \ll E$) in eV; $\ln\Lambda$ is the Coulomb logarithm.

Figure 1 shows the values of B and $n\tau_1$ calculated from Eqs. (1)-(3). The data on the cross section σ (E) are taken from [5]; $\ln\Lambda = 18$; $T_e = 5$-8 keV; $n = 10^{14}$-10^{15} cm^{-3}. Similar results having accuracy of 20% were obtained when finding (–dE/dt) from the solution of the Fokker–Planck equation [6]. The effect of deuteron accumulation in the target can be taken into account with sufficient accuracy by introducing the factor $(1-\alpha)$ into Eq. (1), where α is the relative deuteron density. In this case, n in Eqs. (1)-(3) signifies the overall plasma density.

The condition for positive energy balance in the stationary plasma-beam system has the form

$$[IB(1-\alpha)W_n\eta_n + p\eta_{pl}]\,\eta_i \geqslant p, \tag{4}$$

where $p = 3nT_eV/\tau \geq IE$ is the power input to the target ($T_i \approx T_e$); W_n is the reaction energy; η_{pl} and η_n are the plasma-energy and reaction-product conversion efficiencies, respectively; η_i is the average efficiency of the injector and the additional means for heating the target; V is the target volume; τ is the energy time for plasma confinement.

From Eq. (4) we can obtain estimates of the critical target and beam parameters:

$$n\tau \geqslant \frac{3\,(n\tau_1)\,T_eQ}{\alpha_1(1-\alpha)W_nB}; \tag{5}$$

Translated from Atomnaya Énergiya, Vol. 34, No. 6, pp. 490-491, June, 1973. Original article submitted April 17, 1972; revision submitted October 30, 1972.

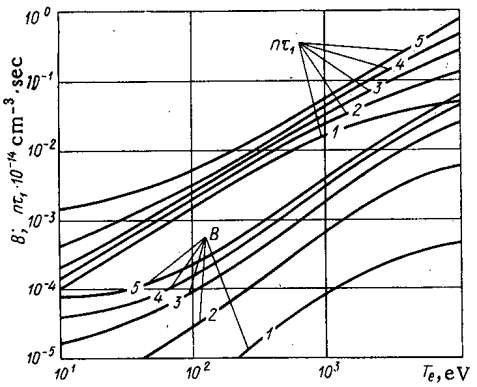

Fig. 1

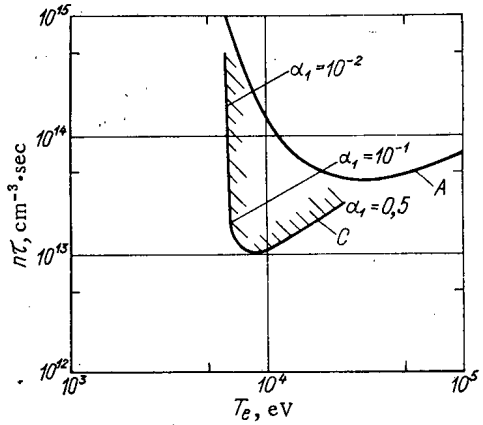

Fig. 2

Fig. 1. Dependence of $n\tau_1$ and B on the deuteron energy E and the target electron temperature T_e. The deuteron energies are: 1) 50; 2) 100; 3) 200; 4) 400; 5) 1000 keV.

Fig. 2. Lawson curves for thermal (Q = 2) and beam (C region filled) reactors: $\alpha = \alpha_1$ when $\tau \leq \tau_1$; $\alpha = \alpha_1(\tau/\tau_1)$ when $\tau > \tau_1$.

$$\frac{B}{E} \geqslant \frac{Q}{(1-\alpha)W_n}; \tag{6}$$

$$\frac{I}{V} = \frac{\alpha_1 n^2}{n\tau_1}, \tag{7}$$

where $Q = (1 - \eta_{pl}\eta_u)/\eta_n\eta_u$; $\alpha_1 = n_1/n$; $n_1 = I\tau_1/V$ is the high-energy deuteron density in the target.

Equation (6) establishes a lower limit for the target temperature, which has a minimum when E ≈ 200 keV, which is in accordance with the results of [4]. It follows from Eqs. (5) and (6) that taking deuteron accumulation into account ($\alpha \neq 0$) leads to increased critical values for T_e and $n\tau$.

The quantity α cannot be as small as we wish. Equations (5) and (6) and the natural requirement $\alpha_1 \leq \alpha$ limit α with a lower bound of $\alpha_{min} = (1/2)(1 - (12T_eQ/W_nB))$ and upper bound $\alpha_{max} = 1/2$, at which the absolute minimum of $n\tau$ is reached.

Figure 2 depicts the region C of $n\tau$ and T_e values which satisfy Eqs. (5) and (6) for E = 200 keV, Q = 2 ($\eta_n = 1/3$, $\eta_{pl} = 2/3$, $\eta_i = 3/4$) and $W_n = 2.4$ MeV. In this case, $T_{e(min)} \approx 6.5$ keV. The minimum for $n\tau$ ($\sim 10^{13}$ $cm^{-3} \cdot sec$) is attained when $T_e \approx 9$ keV and $\alpha = \alpha_1 \approx 1/3$.

For comparison we show the A region for $n\tau$ and T_e ($T_i = T_e$) values of the plasma in a thermal reactor with Q = 2. It is clear from Fig. 2 that the conclusion of [4] concerning easing the Lawson criterion in a beam system holds when the final deuteron density is taken into account, if α_1 is not too small ($\alpha_1 \geqslant 1.5 \cdot 10^{-2}$). The best approximation of the plasma parameters in existing and planned experimental installations to the C region occurs when $\alpha = \alpha_1 \approx 0.1$.

We will estimate the size of the beam current. It follows from Eq. (7) that, when $n \approx 10^{14}$ cm^{-3}, $\alpha_1 = 0.1$, $T_e = T_{e(min)}$, and under the conditions of Fig. 2, the unit current is $I/V \approx 8.3 \cdot 10^{-6}$ A/cm^3. When $V \approx 10^6$ cm^3, a current of I ≈ 8.3 A is required. Obtaining such currents is feasible with modern technology.

In conclusion, we note that the position of the C boundary in Fig. 2 is significantly dependent on several factors. Thus, increasing deuteron stopping due to collective processes (which are especially dangerous when large α_1 are of interest), the presence of heavy impurities, etc., cause decreased output of the B reaction and, yet, push the C boundary closer to the thermal-reactor A region. This effect can be compensated to a certain extent by increasing the energy-conversion efficiency (decreasing Q) and the effective value of W_n (for example, through fission reactions).

LITERATURE CITED

1. C. Barnett et al., Plasma Physics and Controlled Nuclear Fusion Research, Vol. I, IAEA, Vienna (1971), p. 347.

2. K. Berkner et al., ibid, Vol. II, p. 718.
3. L. A. Artsimovich, Controlled Thermonuclear Reactions [in Russian], Fizmatgiz, Moscow (1961).
4. J. Dawson et al., Matt-841 (1971); Phys. Rev. Lett., 26, 1156 (1971).
5. C. Barnett et al., ORNL-3113 (1964).
6. M. J. Caby-Eyrand, Physique, 31, 445 (1970).

AVERAGE YIELD OF PROMPT NEUTRONS $\bar{\nu}$ IN THE FISSION OF U^{233} BY NEUTRONS WITH ENERGIES FROM 0 TO 1.4 MeV

B. Nurpeisov, V. G. Nesterov,
L. I. Prokhorova, and G. N. Smirenkin

UDC 546.799.4

The present work is one stage in the investigation of the dependence of $\bar{\nu}$ on the neutron energy E_n for the basic materials used in reactors.

The method of relative measurements of $\bar{\nu}(E_n)/\nu_0$, used previously in experiments with U^{235} [1] and Pu^{239} [2], is based on the recording of coincidences of pulses from a fragment detector (multiplate ionization chamber) and a neutron detector (24 He^3 counter in a paraffin block). The well known value $\nu_0(Cf^{252}) = 3.756$ [3] for spontaneous fission was taken as a standard. The measurements were performed on a cascade generator using the T(p, n) reaction.

The ratio

$$\rho/\rho_0 = A\bar{\nu}/\bar{\nu}_0,$$

was measured directly in the experiment; ρ and ρ_0 are respectively the number of true coincidences and the number of fissions for the isotope under study and the standard: $A \approx 1$ is a factor taking account of the difference in detector efficiencies in measurements with a layer of Cf^{252} and an arrangement of layers of U^{233}. The only difference from the earlier measurements [1, 2] is that in the present work we used a more compact arrangement of layers in the fission chamber, permitting a decrease in the basic correction for the size fo the fission source from 3.8 ± 0.2% for Pu^{239} [2] and 1.11 ± 0.2% for U^{235} [1] to 0.71 ± 0.2% for U^{233} (Table 2).

TABLE 1. Renormalized Data on $\bar{\nu}$ for U^{233}

E_n, MeV	$\bar{\nu}(E_n)/\bar{\nu}(E_n^0)$	$\bar{\nu}(E_n)$ (renormalized values)
0,08	1,011±0,007	2,511±0,024
0,20±0,05	1,002±0,008	2,489±0,025
0,30±0,05	0,992±0,005	2,464±0,020
0,40±0,05	1,000±0,000	2,484±0,016
0,50±0,05	1,004±0,005	2,494±0,020
0,60±0,05	1,012±0,005	2,514±0,020
0,70±0,05	1,022±0,006	2,539±0,022

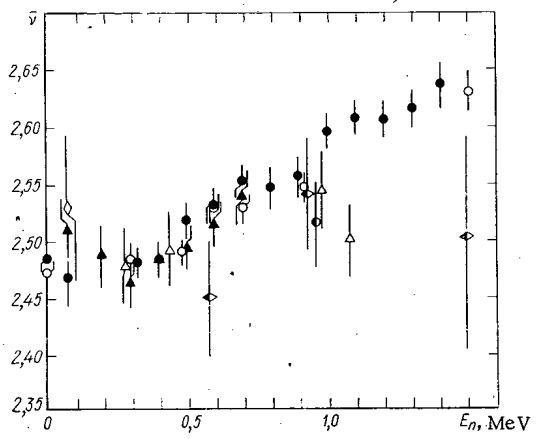

Fig. 1. Data on the average number of prompt fission neutrons $\bar{\nu}$ for U^{233}: ▲) [4]; ○) [5]; ◇) [6]; △) [7]; ◀▷) [8]; ◐) [9]; ●) present work.

Translated from Atomnaya Énergiya, Vol. 34, No. 6, pp. 491-493, June, 1973. Original article submitted December 28, 1972.

TABLE 2. Measured Values of $\bar{\nu}$ for U^{233}

No. of cycles	E_n, MeV	Experimental value of $\rho(E_n)/\rho_0$	$\bar{\nu}(E_n)/\bar{\nu}_0$	$\bar{\nu}(E_n)$
80	0,00 *	0,6708±0,0019	0,6615±0,0027	2,485±0,010
87	0,08 †	0,6663±0,0038	0,6574±0,0043	2,469±0,016
47	0,325±0,048	0,6687±0,0031	0,6607±0,0037	2,482±0,014
63	0,400±0,044	0,6691±0,0038	0,6614±0,0043	2,484±0,016
48	0,500±0,045	0,6776±0,0039	0,6703±0,0043	2,518±0,016
71	0,600±0,043	0,6810±0,0037	0,6738±0,0041	2,531±0,015
64	0,700±0,041	0,6867±0,0032	0,6794±0,0037	2,552±0,014
67	0,800±0,036	0,6852±0,0042	0,6779±0,0046	2,546±0,017
48	0,900±0,042	0,6875±0,0039	0,6805±0,0043	2,556±0,016
66	1,000±0,038	0,6969±0,0039	0,6907±0,0043	2,594±0,016
56	1,100±0,037	0,6992±0,0038	0,6936±0,0042	2,605±0,016
50	1,200±0,030	0,6984±0,0038	0,6932±0,0042	2,604±0,016
42	1,300±0,030	0,6994±0,0040	0,6953±0,0045	2,612±0,017
27	1,400±0,029	0,7040±0,0050	0,7011±0,0054	2,633±0,020

*Data for E_n = 0 obtained for 0.3 MeV neutrons slowed down in a polyethylene block.

†Proton energy was set at 25 keV above the threshold of the T(p, n) reaction.

The error in ρ/ρ_0 was taken as the statistical error or the error calculated from the dispersion of the individual cycles of measurements, whichever was larger. The number of cycles is listed in the first column of Table 2. The error in $\bar{\nu}(E_n)$ was calculated as the mean square of the errors in the ratio ρ/ρ_0 and the factor A. It does not include the error in the absolute value of $\bar{\nu}_0$.

Figure 1 shows a comparison of our measurements with other data [4-9]. The results in [4] in which $\bar{\nu}(E_n)/\bar{\nu}(E_n^0)$ was measured with a threshold detector (reference energy E_n^0 = 0.4 MeV) were normalized to the value $\bar{\nu}(E_n^0)$ = 2.484 ± 0.016 obtained in the present work. In [4] the absolute behavior of $\bar{\nu}(E_n)$ for U^{233} was determined by an indirect and approximate method of analyzing the equation for the fission energy balance. Our present experiment removes this shortcoming and we therefore recommend the renormalized data of [4] listed in Table 1.

The experimental data shown in Fig. 1 are in satisfactory agreement but there are not enough of them to permit a statistical analysis [1, 2].

The authors thank A. P. Klimov, G. I. Abakumov, and the whole staff for keeping the accelerator operating well, Yu. M. Turchin, N. E. Fedorovaya, Yu. I. Baranov, K. E. Volodin, and V. E. Rudnikov for helping with the measurements.

LITERATURE CITED

1. L. I. Prokhorova et al., Atomnaya Energiya, 30, 250 (1971).
2. K. E. Volodin et al., Atomnaya Energiya, 33, 901 (1972).
3. G. Hanna et al., Atomic Energy Rev., 7, No. 3, 4 (1969).
4. V. F. Kuznetsov and G. N. Smirenkin, Yaderno-Fizicheskie Issledovaniya, 4, 19 (1967).
5. R. Walsh and J. Boldeman, J. Nucl. Energy, 25, 321 (1971).
6. B. Diven et al., Phys. Rev., 101, 1012 (1956).
7. J. Hopkins and B. Diven, Nucl. Phys., 48, 433 (1963).
8. D. Colvin and M. Sowerby, for data see J. R. Stehn et al. Neutron Cross Sections, BNL-325, 2nd Ed., Supp. No. 2 (1965).
9. D. Mather et al., Nucl. Phys., 66, 149 (1965).

THE THIRTY-THIRD SESSION OF THE OIYaI ACADEMIC COUNCIL

V. A. Biryukov

The thirty-third session of the Academic Council of the Joint Institute for Nuclear Research (OIYaI) was held at Dubna on January 9-12, 1973. After opening the session, N. N. Bogolyubov, Director of the Institute, reported that the entire international staff of the OIYaI had joined in extensive celebrations of the fiftieth anniversary of the founding of the Union of Soviet Socialist Republics. In their scientific works, the Institute's scientists concern themselves not only with the development of science at the OIYaI but also with the establishment and growth of the physical sciences in each of the participating countries. Scientists from the socialist countries were very helpful to the physicists of the USSR Union Republics and did a great deal to promote the training of personnel and the development of research centers in those Republics. For its important services, the Institute was awarded the Jubilee Badge of Honor commemorating the fiftieth anniversary of the establishment of the USSR. The Institute published a collection, The OIYaI and the Development of Nuclear Physics in the Soviet Republics, describing the scientific cooperation of the OIYaI with the national physics centers and universities of the Soviet Union and the links it maintains with those centers and universities.

N. N. Bogolyubov gave a brief survey of the main lines of activity pursued by the Institute in 1972.

Reports on the results of scientific investigations were delivered by the heads of the Institute's laboratories. D. I. Blokhintsev, Director of the Theoretical Physics Laboratory, reported on the important results achieved in research on the theory of elementary particles and the theory of atomic nucleus. The axioms of quantum field theory had been used as a basis for developing an apparatus that made possible the rigorous justification of methods using the concept of self-similarity of the asymptotic behavior of form-factors in the processes of weak and electromagnetic interaction of hadrons at high energies. The important role of scale transformations and dimensional analysis in high-energy physics was made clear, and new implications of the self-similarity hypothesis in strong, weak, and electromagnetic interactions were found. It was shown that power-series asymptotics for Green's functions and limit expressions of the scale-invariant type for higher Green's functions follow from the assumption that renormalizations of coupling constants are finite.

A new approach was proposed for the study of the structure of highly excited states of atomic nuclei. Analyses were given for those components of the wave functions of neutron resonances which have few quasiparticles and for those which have many quasiparticles. It was shown that the magnetic moments of neutron resonances must be of the same order of magnitude as the single-particle values. Direct reactions with compound nuclei were discussed.

A. M. Baldin reported on the work that the High-Energy Laboratory's scientists had done on the accelerator of the Institute of High-Energy Physics (IFVE) and on the Dubna synchrophasotron. A large number of experiments on elastic interactions of protons at energies of 10-70 GeV are being processed. Researchers have determined the real parts of the amplitude and the cross sections of pp- and pd-scattering, the form factor of the deuteron and the parameters of pn-interaction. Research on the regeneration of K^0-mesons by hydrogen is continuing. It was established that the modulus of the meson regeneration amplitude decreases with increasing energy, while its phase remains constant. Thus, no violations of Pomeranchuk's theory were observed in the 10-50 GeV range. Tests on regeneration by deuterium were conducted with the aid of the 3-meter liquid deuterium target developed at the High-Energy Laboratory; the magnetic tapes of the experimental data were processed not only at Dubna but also in Bulgaria, Hungary, the German Democratic Republic, and Czechoslovakia.

Translated from Atomnaya Énergiya, Vol. 34, No. 6, pp. 495-497, June, 1973.

Work was completed on the irradiation of the 2-meter propane bubble chamber with pions having a momentum of 40 GeV/sec. About 300,000 photographs were obtained, after which the chamber was shipped to Dubna. Scientists of eight countries are studying the multiple formation of particles in π^-p-, π^-n-, and π^-C-interactions and of processes in which γ-quanta participate. About 100,000 frames have been examined. Work is continuing on the irradiation of the "Lyudmila" 2-meter hydrogen chamber in the beams of the Serpukhov accelerator.

The investigation of the interaction of deuterons having momentum values of 2.5 GeV/sec with photoemulsion nuclei, conducted on the OIYaI's synchrophasotron, was completed. For the average emulsion nucleus the total cross section of the interaction is 1.425 ± 110 mb; the cross sections of elastic and inelastic scattering and the cross section of deuteron stripping were measured. Continued work was done with photographs of a 1-meter hydrogen chamber irradiated with deuterons having momentum values of 3.3 GeV/sec was continued. This chamber is also being used for investigating π^-p-interaction with a momentum of 5 GeV/sec. The irradiation of the 1-meter streamer chamber in a beam of synchrophasotron K^0-mesons was completed. Among 150,000 photographs, 20,000 disintegrations of K^0-mesons were found; these included 100 rare disintegrations with a Dalitz pair.

Test-stand trials of 2-meter streamer chamber with a working volume of 200 × 100 × 60 cm were completed. The apparatus is being constructed in collaboration with physicists and engineers of the OIYaI's Laboratory of Computational Techniques and Automation and institutes at Lodz (Poland), Alma-Ata, and Tomsk. Two spark-type filament chambers, a 2-meter chamber, and a 1-meter chamber, have been designed and are being constructed for physics experiments.

An important achievement was the slow extraction of accelerated protons from the synchrophasotron. The efficiency of the extraction is more than 90%.

The work done by the scientists of the Nuclear Problems Laboratory was described in a report by V. P. Dzhelepov. In investigations with a 1-meter propane chamber irradiated on the synchrophasotron with a beam of pions having a momentum of 5 GeV/sec, the researchers observed channels of many rare reactions, with the formation of several strange particles and neutral mesons in a single event the cross sections of these were determined. The existence of a resonance in the Λ^0p-interaction was confirmed. The work is being conducted with the participation of physicists from the Georgian SSR and Czechoslovakia. The interactions of pions with He^3 is being studied with the aid of a high-pressure streamer chamber. The angular distributions of elastically scattered π^+- and π^--mesons with energies of 97 MeV were determined. The total cross sections of elastic scattering of pions at this energy were $\sigma(\pi^-, He^3) = 30.95 \pm 1.32$ mb and $\sigma(\pi^+, He^3) = 43.55 \pm 1.77$ mb. It was found that the phase of the scattering, plotted as a function of energy, has a resonance near 140 MeV. Physicists from Romania and Italy took part in these studies.

The differential cross sections of pp-scattering in the small-angle range was determined with very high accuracy; the experimental values for angles of 2.2-6.5° (laboratory reference system) were found to be much lower than those obtained in earlier measurements by other authors. New results were found in the investigation of short-lived isotopes far from the stability band; the spectra studied included those of γ-radiation, $\gamma-\gamma$ coincidences, and conversion electrons. A new isotope, Rb^{72}, was discovered.

Work was successfully continued in a new direction, that of mesochemical research. In investigations of the mutual influence of atoms and atom groups in complex organic molecules by irradiation of various substances with negative pions, it was found that the replacement of a hydrogen atom in a saturated hydrocarbon by an OH group results in a strong displacement of the density of the valence electrons toward the OH group. Similar results were obtained for a number of benzene derivatives.

In experiments aimed at discovering Dirac monopoles, conducted on the IFVE's 76 GeV accelerator at Serpukhov, a preliminary estimate was found for the upper limit of the cross section of the generation of monopoles by 70 GeV protons on nuclei of an SiO_2 target: $\sigma < 8 \cdot 10^{-40}$ cm^2 for a mass of $M = (4\text{-}5)m_p$, and $\sigma < 1.6 \cdot 10^{-39}$ cm^2 for a mass of $M = 3m_p$. Measurements of polarization in π^-p-scattering at 40 GeV/sec were also begun at Serpukhov. Those participating in the construction of the complex installation, which operates with electronic computers, included physicists of the OIYaI Nuclear Problems Laboratory, the IFVE, the Institute of Theoretical and Experimental Physics (ITEF), and Saclay (France). The measurement results yield a maximum value of 6% for the polarization.

A 5-meter magnetic spark spectrometer was installed on a beam of the IFVE accelerator. A test startup was conducted. The work done at the Nuclear Problems Laboratory included investigations that

made it possible to construct a new charged-particle detector, namely, a filament-type crystal counter in which the recording takes place through avalanche multiplication of primary-ionization electrons in solid frozen argon or xenon.

Research on a collective-accelerator model was continued at the New Acceleration Methods Section. A report on this work was delivered by V. P. Sarantsev. The problem of shaping the transition from the magnetic field of the adherer to the field of the transition segment was solved. Stable operation was achieved on the accelerating section of the model, which consists of four hot resonators. The amplitudes of the accelerating field were about 90 kV/cm for a magnetic field of the order of 10 kG. Special systems were constructed for the diagnosis of the charged ring in the linear induction accelerator, the adherer, and the accelerating section.

Study of all the nodes of a multicharge ion accelerator was completed. Specialists completed the installation and adjustment of systems on the SILUND accelerator, at the outlet of which they obtained an electron beam with a current of about 600 A and a pulse length of the order of 40 nsec. A number of different variants of the adherer were developed: one with a metal chamber, one with a sheathed chamber, and one variant which had a chamber with spherical walls made of a tungsten–titanium alloy or of steel with no plastic sheathing.

For the acceleration of an annular cluster, specialists developed accelerating sections with superconductive resonators and pulse lines. Work was completed on the construction of the equipment of the "kol'tsetron"; this is a superconductive section consisting of four resonators. The system was filled with helium, and physical investigations of the "kol'tsetron" were begun.

A large body of theoretical investigations was related to the study of physical processes in the collective method of acceleration.

M. G. Meshcheryakov reported on the activities of the Computational Techniques and Automation Laboratory. The output of the central computing facility of the OIYaI was doubled by the addition of a new CDC-6200 computer to the system (the CDC-6200 has a memory of 64 K, an access time of 1 μsec, and seven peripheral processors). For efficient utilization of the CDC-6200, the library of standard programs produced on the BESM-6 was transferred to it. In accordance with the plans for a multicomputer facility, work was done with a view to including the BESM-6, the Nuclear Problems Laboratory's Minsk-2, the Neutron Physics Laboratory's BESM-4 and TPA-1001, and the High Energy Laboratory's TPA-1001 in the system. A start was made in processing on the BESM-6 the spectrometric information obtained by means of lines from the Nuclear Problems Laboratory and the Neutron Physics Laboratory.

Further work was done to improve the software of the electronic computers. Twenty-six general-purpose programs for the BESM-6 were replaced with new versions, and 76 more programs were added. A translator for converting machine language to automatic coding was constructed. Work was completed on the construction of a translator from FORTRAN to the language of the BESM-4 computers included in the computing installation. With a view to the operation of the overall system of the measuring and computing installation, algorithms were worked out for checking the functioning of the system and controlling it through the BESM-6 display station.

The optical–mechanical part and the electronic part of the pilot specimen of the "Spiral Meter," an automatic device for processing photographs from bubble chambers, were constructed and assembled. Work is being done on adjusting the apparatus in coordination with the E-100 computer and a control program. The scanning of real photographs was carried out for the first time. Work was continued with a view to improving the HPD automatic scanner, which is now in experimental operation. A scheme was worked out for modernizing its electronic part by including a TPA-1001 control computer. Two BPS-1 monitoring consoles constructed at Dubna and two SAMET monitoring and measuring consoles, of Czechoslovakian manufacture, were placed in operation.

Development of a graphic display system using the TEKTRONIX memory tube was completed: the display system is connected to the "Parameter" electronic computer. The technical documentation for a pointwise display system for small "Parameter" computers was prepared, and a specimen was constructed. A number of studies were concerned with the preparation of software for experiments conducted with filmless spark chambers on the accelerators of the High-Energy Laboratory and the Institute of High-Energy Physics (Serpukhov), the programmed control of a system for the slow extraction of protons from the synchrophasotron, and an apparatus for the investigation of proton–nucleus interaction at energies of 4-10 GeV.

Further work was done to develop methods of applied computation in connection with investigations conducted at the laboratories of the OIYaI.

Among the most important studies conducted at the Neutron Physics Laboratory, described in a report by I. M. Frank, were investigations with polarized nuclear targets and polarized neutrons in the resonance energy range. Work to improve this type of procedure has been done at the Laboratory in recent years. A refrigerator using the dissolution of liquid He^3 in He^4, capable of cooling targets to 0.02°K, was set up on a beam of the IBR-30. This apparatus was used for measuring the magnetic moments of two compound states of erbium at an excitation energy of 6 MeV which were equal (in nuclear magnetons) to 0.9 ± 0.4 and 1.8 ± 0.9 for the Er^{167} resonances at 0.46 and 0.58 eV, respectively. Work was continued on the optimization of channels and the search for promising moderators of ultracold neutrons. A zirconium hydride moderator was tested, and new materials for neutron accumulation vessels were investigated.

In research on the α-decay of resonance states of nuclei, measurements were made for the spectra of α particles from the 55 eV resonance in the two-stage $Nd^{143}(n, \gamma\alpha)Ce^{140}$ reaction. Two other isotopes for which an (n, α) reaction was discovered at a number of resonances were Eu^{151} and Gd^{155}. In connection with the previously discovered anomaly in the carbon distribution in neutron scattering by lanthanum, new measurements were made by the time-of-flight method, with improved resolution: an anomalously large asymmetry was confirmed for La^{139} and was also found in Pr^{141}. The γ-radiation of the radiative capture of neutrons in the resonances of Sm^{147}, Gd^{157}, and Cd^{158} was measured. The spins of the neutron resonances of Gd^{157} were measured by the method of multiplicity of γ-radiation in cascade.

The noncoherent inelastic scattering of thermal neutrons by polycrystalline specimens of $MgZn_2$ was measured. The experimentally determined density of phonon states corroborates the existence of low optical branches of the phonon spectrum which had been predicted on the basis of theory. An inverse-geometry spectrometer was used for investigating the diffusive movement of molecules for two compounds: para-azoxyanisol and butyl chloride. Further investigations were conducted on the inelastic paramagnetic scattering of neutrons in polycrystals.

G. N. Flerov reported on the research carried out by the scientists of the Nuclear Reactions Laboratory. The intensity of a beam of Xe^{136} ions accelerated by means of a system of tandem cyclotrons to a final energy of about 900 MeV has been increased more than a hundredfold and is now $2.5 \cdot 10^{10}$ particles /sec. The high energy makes it possible to bring about nuclear reactions involving nuclei of the heaviest elements. These beams were used for a detailed investigation of the process of fission of the heavy nuclei formed upon the irradiation of Ta^{181}. Experiments with zinc, tantalum, bismuth, and uranium showed that the fission process is a promising method for synthesizing superheavy nuclei. In the U + Xe reaction, an estimate was found for the upper limit of the cross section of formation of superheavy nuclei ($109 \leq Z \leq 115$) with a half-life of 1-100 days: $\sigma_{sf} \leq 10^{-33}$ cm^2.

In investigations of proton-radioactive nuclei, the Laboratory's scientists studied the decay properties of light isotopes of tellurium and measured β^+p-coincidences for Te^{109}. A comparison of proton spectra in coincidence with positrons and without such coincidences indicates that the mass defects of Te^{109} and Sn^{108} differ by 7.14 ± 0.10 MeV. For the spontaneously fissionable isomers of Pu^{236}, Pu^{237}, and Cm^{243} formed in the (α, 2n) and (α, 3n) reactions, the angular distribution of fission fragments was measured. The cross sections of the (n, 2n) and (n, n') reactions at neutron energies of 14.7 MeV resulting in the formation of spontaneously fissionable isomers were determined. Further studies were conducted on the properties of light nuclei with large neutron excesses which were synthesized in transfer reactions with heavy ions. In their experiments the Laboratory's scientists measured the previously unknown masses of the heavy oxygen isotopes O^{21} and O^{22}; the values of M – A for these were found to be $9.3^{+0.3}_{-0.7}$ and $11.5^{+0.2}_{-0.5}$ MeV, respectively. They processed the experimental results by making measurements using the method of observation of the "shadow effect" of the lifetimes of the compound nuclei formed upon the irradiation of single-crystal Ta^{181} and W^{186} targets with various heavy ions. New experimental data on the lifetimes of the four levels of Yb^{162} were obtained by the method of Doppler displacement on recoil nuclei.

A report on international cooperation and the relations maintained by the OIYaI with other institutions was delivered by Deputy Director A. Mikhul. The Institute's laboratories carried out about 270 studies in collaboration with the national organizations of member countries. About 400 specialists have spent time at Dubna in connection with this work; about 300 persons have attended lectures and meetings organized by the OIYaI. Among the meetings held were the Second International Symposium on High-Energy Physics (in Czechoslovakia), the International Symposium on Elementary-Particle Theory (in the German Democratic

Republic), the Seminar on Nuclear Structure (Alushta, USSR), the Symposium on Collective Methods of Acceleration (at Dubna), and working conferences at Dubna, Tbilisi, and Warsaw.

N. N. Bogolyubov delivered a report on the draft proposals for the future plans of development of the OIYaI and the status of the preparatory work already done on this plan.

Diplomas were awarded at the session to the authors of the best studies that had won OIYaI prizes in 1972. First prizes were awarded to two series of studies entitled "Examination on the Interactions of Negatively Charged Mesons in Matter and the Development of Methods of Mesochemical Investigation" and "Investigation of New Conditions of Operation for Streamer Chambers, Development of Helium Target Chambers, and Construction of a High-Pressure Streamer Spectrometer." Second prizes in the field of scientific research were awarded to a series of studies on the real part of the amplitudes of forward pp- and pd-scattering in the 8-70 GeV energy range and to a study entitled "The Nuclear Problem of Three Bodies with Local Potentials." In the field of studies on scientific methodology, second prizes were awarded for the construction of a set of hydrogen targets to be used in physics research on accelerators and for a study entitled "Obtaining Accelerated Xenon Ions on the OIYaI's Tandem Cyclotron."

ANNIVERSARIES

TWENTY-FIFTH ANNIVERSARY OF THE FIRST SOVIET SYNCHROTRON

B. S. Ratner

January 11, 1973 marked the twenty-fifth anniversary of the startup of the first synchrotron in the USSR. A seminar celebrating this anniversary was held at the P. N. Lebedev Physics Institute of the Academy of Sciences of the USSR. After an introduction by P. A. Cherenkov, several reports were delivered: "Construction and Startup of the First Soviet Synchrotron" (B. S. Ratner), "V. I. Veksler and the Beginnings of Accelerator Development at FIAN" (M. S. Rabinovich), and "From the First Synchrotron to the Accelerators of Today" (A. A. Kolomenskii). E. L. Feinberg, A. L. Mints, and others recounted their experiences of earlier years.

Work on the construction of the synchrotron began in 1945, shortly after V. I. Veksler's discovery of the principle of phase stability of particles. Serious difficulties arose at the very outset of the work, principally because the problem was such a new one. During the first postwar years Soviet industry was not yet ready for the manufacture of such extraordinary physics apparatus, and it was only with great difficulty that V. I. Veksler was able to arrange for the manufacture of the synchrotron magnet at the Moscow Transformer Works. In the spring of 1946 the magnet, designed for accelerating electrons to 300 MeV, was installed in one of the rooms of the old Physics Institute building.

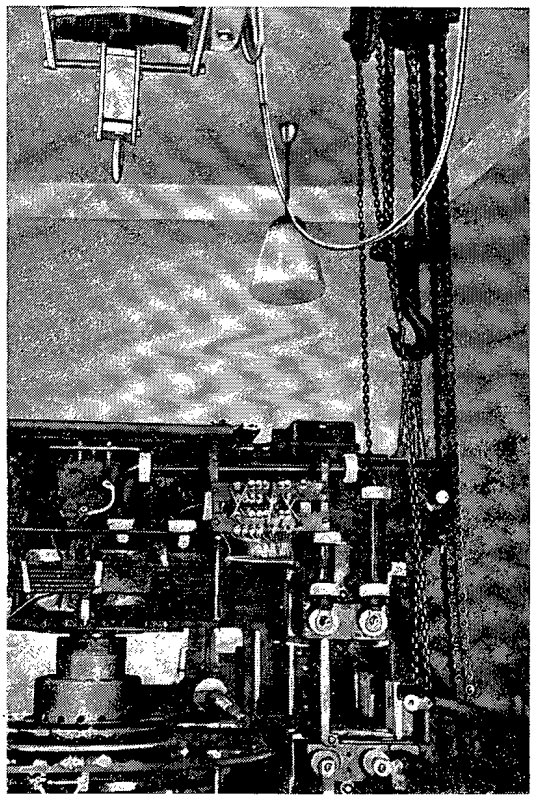

Fig. 1. The synchrotron before startup. The upper yoke of the magnet has been raised.

Initially it was proposed that a radioactive source of electrons should be used at the injector, and therefore the magnet was not equipped with a central core necessary for the preliminary acceleration of electrons in betatron operation. Magnetic measurements were begun in the summer of 1946. At the same time, constant-current magnets were used to investigate the shape to be selected for the pole terminals. The first glass vacuum chamber with circular cross section was also constructed at that time.

It was soon decided to use betatron operations for the preliminary acceleration of electrons to relativistic velocities. A Permalloy wire core was constructed in the laboratory (after annealing, each of the several thousand wires was insulated by hand with Bakelite lacquer). Parallel with this, work was done on the preparation and testing of the injectors, the pulse generator, and the conducting layers mounted on the inner wall of the chamber. Research on the construction of the high-frequency accelerating field was begun some time later. The Institute's scientists designed the superposed wire resonators and the high-frequency generator feeding them, as well as the systems for matching and regulating the high-frequency field. At the

Translated from Atomnaya Énergiya, Vol. 34, No. 6, pp. 498-499, June, 1973.

same time, they worked out methods for finding the position of the equilibrium betatron orbit and the coefficient of decay of the magnetic field.

The first attempts to start up the accelerator were made at the end of 1946. By that time the Institute's scientists had come to understand a very important factor which substantially determined the operation of the accelerator: the existence of a phase displacement in the magnetic field at different azimuths of the electron orbit, as a result of unequal losses in the iron. The phase asymmetry of the magnetic field was substantially reduced by means of loops wound around the pole. The Institute's scientists obtained one revolution of the electrons, but they failed to detect any bremsstrahlung, the sure sign of successful acceleration.

At this point they made a bold decision and adopted the only true solution, namely, to discontinue their startup attempts and to construct a new magnet with a larger working region and better characteristics. A new magnet was ordered from the Moscow Transformer Works. It was designed by the Design Bureau of the Moscow Transformer Works, and it took account of the experience acquired in the investigations on the first magnet. A Moscow glass factory produced half-rings for a new vacuum chamber with an elliptical cross section. Only one glass-blower at that factory was capable of blowing such large components. The chambers were welded together at the Institute's glass-blowing shop. Scientists at the Laboratory proposed a more accurate method for measuring the phase asymmetry (using superposed magnetization of the Permalloy sensors with direct current), so that when the magnet was adjusted it would be possible to minimize the nonuniformity of the magnetic field. A special room in the Institute building being constructed at the time was assigned to the synchrotron. The installing of the accelerator in its new room was begun in the autumn of 1947 (see Fig. 1). When the accelerator was turned on for the first time, on December 28, 1947, success was achieved: the Geiger counters set up at various points in the room indicated the presence of bremsstrahlung. Synchrotron operation was achieved on January 11, 1948, and electrons were accelerated to 30 MeV.

Physics research on the synchrotron was begun immediately after startup, both on a γ-ray beam and on an electron beam extracted shortly after startup. The Institute's scientists conducted one of the first investigations of the shape of the accelerator's bremsstrahlung. Since that time, the 30 MeV synchrotron has been in continuous use as a source of γ quanta for the study of photonuclear reactions. After a number of years of operation a new magnet was constructed, and the first magnet of the synchrotron was placed on exhibition of the Polytechnic Museum.

Other laboratories in the Soviet Union also conducted studies on the construction of electron accelerators during those years, assisted during the first stage by V. I. Veksler and his group. The extensive experience acquired in the construction of the Soviet Union's first synchrotron served as the foundation for the successful development of Soviet accelerator technology.

The moving spirit in the construction of the accelerator was V. I. Veksler. Within a short time he had succeeded in organizing a small but highly capable group, inspired people with his ideas, and successfully solved a highly complex problem requiring the joint efforts of physicists (experimental and theoretical), engineers, workers, and technicians. He encouraged independence and initiative among his co-workers in every possible way. Without giving petty instructions on every trifling detail, he was able to keep the work progressing at a rapid rate by the constant interest he took in the work of each member of the group; they worked from morning until late at night. The atmosphere in the laboratory during this time remained calm, without the nervousness and commotion which so often arise in work that must be done within a short deadline. V. I. Veksler worked with the close assistance of B. L. Belousov, whose group carried out the direct assembly and startup of the synchrotron. Those participating in the work of constructing and starting up the synchrotron included A. Ya. Belyak, K. I. Blinov, L. N. Borodovskaya, S. S. Borodin, E. L. Burshtein, B. B. Gal'perin, V. I. Dragan-Sushchev, F. M. Elizarov, Yu. S. Ivanov, I. D. Kedrov, A. A. Kolomenskii, A. P. Komar, N. G. Kotel'nikov, D. D. Krasil'nikov, V. G. Larionov, A. V. Makarov, E. A. Man'kin, E. M. Moroz, A. A. Nikolaev, V. E. Pisarev, A. V. Porosyatnikov, M. S. Rabinovich, B. S. Ratner, I. O. Stal', G. M. Strakhovskii, P. A. Cherenkov, K. V. Chekhlov, and V. E. Yakushkin, and the workers of the mechanical and glass-blowing shops and the instrument group.

breaking the language barrier

WITH COVER-TO-COVER ENGLISH TRANSLATIONS OF SOVIET JOURNALS

in mathematics and information science

Title	# of Issues	Subscription Price
Algebra and Logic *Algebra i logika*	6	$120.00
Automation and Remote Control *Avtomatika i telemekhanika*	24	$195.00
Cybernetics *Kibernetika*	6	$125.00
Differential Equations *Differentsial'nye uravneniya*	12	$150.00
Functional Analysis and Its Applications *Funktsional'nyi analiz i ego prilozheniya*	4	$110.00
Journal of Soviet Mathematics	6	$135.00
Mathematical Notes *Matematicheskie zametki*	12 (2 vols./yr. 6 issues ea.)	$185.00
Mathematical Transactions of the Academy of Sciences of the Lithuanian SSR *Litovskii Matematicheskii Sbornik*	4	$150.00
Problems of Information Transmission *Problemy peredachi informatsii*	4	$100.00
Siberian Mathematical Journal of the Academy of Sciences of the USSR Novosibirski *Sibirskii matematicheskii zhurnal*	6	$195.00
Theoretical and Mathematical Physics *Teoreticheskaya i matematicheskaya fizika*	12 (4 vols./yr. 3 issues ea.)	$145.00
Ukrainian Mathematical Journal *Ukrainskii matematicheskii zhurnal*	6	$155.00

SEND FOR YOUR
FREE EXAMINATION COPIES

PLENUM PUBLISHING CORPORATION
Plenum Press • Consultants Bureau
• IFI/Plenum Data Corporation
227 WEST 17th STREET
NEW YORK, N. Y. 10011

In United Kingdom
Plenur Publishing Co. Ltd., Davis House (4th Floor)
8 Scrubs Lane, Harlesden, NW10 6SE, England

Back volumes are available.
For further information, please contact the Publishers.

breaking the language barrier

WITH COVER-TO-COVER ENGLISH TRANSLATIONS OF SOVIET JOURNALS

in physics

Title	# of Issues	Subscription Price
Astrophysics *Astrofizika*	4	$100.00
Fluid Dynamics *Izvestiya Akademii Nauk SSSR mekhanika zhidkosti i gaza*	6	$160.00
High-Energy Chemistry *Khimiya vysokikh énergii*	6	$155.00
High Temperature *Teplofizika vysokikh temperatur*	6	$125.00
Journal of Applied Mechanics and Technical Physics *Zhurnal prikladnoi mekhaniki i tekhnicheskoi fiziki*	6	$150.00
Journal of Engineering Physics *Inzhenerno-fizicheskii zhurnal*	12 (2 vols./yr. 6 issues ea.)	$150.00
Magnetohydrodynamics *Magnitnaya gidrodinamika*	4	$100.00
Mathematical Notes *Matematicheskie zametki*	12 (2 vols./yr. 6 issues ea.)	$185.00
Polymer Mechanics *Mekhanika polimerov*	6	$120.00
Radiophysics and Quantum Electronics (Formerly Soviet Radiophysics) *Izvestiya VUZ. radiofizika*	12	$160.00
Solar System Research *Astronomicheskii vestnik*	4	$ 95.00
Soviet Applied Mechanics *Prikladnaya mekhanika*	12	$160.00
Soviet Atomic Energy *Atomnaya énergiya*	12 (2 vols./yr. 6 issues ea.)	$160.00
Soviet Physics Journal *Izvestiya VUZ. fizika*	12	$160.00
Soviet Radiochemistry *Radiokhimiya*	6	$155.00
Theoretical and Mathematical Physics *Teoreticheskaya i matematicheskaya fizika*	12 (4 vols./yr. 3 issues ea.)	$145.00

Back volumes are available. For further information, please contact the Publishers.

SEND FOR YOUR FREE EXAMINATION COPIES

PLENUM PUBLISHING CORPORATION
227 WEST 17th STREET
NEW YORK, N. Y. 10011
Plenum Press • Consultants Bureau
• IFI/Plenum Data Corporation

In United Kingdom
Plenum Publishing Co. Ltd., Davis House (4th Floor)
8 Scrubs Lane, Harlesden, NW10 6SE, England

Declassified and Approved For Release 2013/09/15 : CIA-RDP10-02196R000400010006-4